Slot Suction of the Turbulent Boundary Layer

An Experimental Study

Tim van der Hoeven

March 28, 2013

Faculty of Aerospace Engineering · Delft University of Technology

Challenge the future

Slot Suction of the Turbulent Boundary Layer

An Experimental Study

MASTER OF SCIENCE THESIS

For obtaining the degree of Master of Science in Aerospace
Engineering at Delft University of Technology

Tim van der Hoeven

March 28, 2013

Faculty of Aerospace Engineering · Delft University of Technology

Delft University Of Technology
Department Of
Aerodynamics

The undersigned hereby certify that they have read and recommend to the Faculty of Aerospace Engineering for acceptance a thesis entitled **“Slot Suction of the Turbulent Boundary Layer”** by **Tim van der Hoeven** in partial fulfillment of the requirements for the degree of **Master of Science**.

Dated: March 28, 2013

Head of department: Prof. Dr. Ir. F. Scarano

Supervisor: Dr. Ir. L.L.M. Veldhuis

Reader: Dr. Ir. B.W. van Oudheusden

Reader: Ir. E. Terry

Reader: Dr. Ir. D. Ragni

Abstract

This study examines the effects of slot suction on the mean characteristics of a two-dimensional turbulent boundary layer. Previous studies on this subject have mainly focused on low Reynolds number boundary layers (i.e. $\mathrm{Re}_\theta \leq 2{,}000$). Furthermore, numerical tools are often not able to accurately predict the effects of slot suction. To grasp the effects of slot suction at conditions more relevant to engineering problems, the present research focuses on a turbulent boundary layer with a Reynolds number of $\mathrm{Re}_\theta \approx 10{,}000$.

An experimental investigation has been conducted in the W-tunnel facility at the Delft University of Technology. Two-component planar particle image velocimetry measurements have been performed for boundary layer slot suction at a zero pressure gradient and at an adverse pressure gradient of $\frac{dp}{dx} \approx 200$ [Pa/m]. For these cases, the Reynolds number based on the momentum thickness, for the undisturbed boundary layer was 10,100 and 11,600 respectively. Furthermore, for the adverse pressure gradient case, comparative measurements have been conducted for distributed suction through a porous plastic and a perforated plate.

The results from these measurements are presented in terms of the mean velocity field, the mean pressure distribution and the boundary layer integral parameters. The result of suction on the zero pressure gradient boundary layer show good qualitative correspondence with the low Reynolds number literature. A nearly linear relation is found between the reduction in the Reynolds number based on the momentum thickness and the suction coefficient. For the shape factor this relation is found to be non-linear.

The results for slot suction in the presence of an adverse pressure gradient, generally show strong similarity with the zero pressure gradient case. The change in the pressure distribution and the Reynolds number based on the momentum thickness, relative to the situation without suction is similar as for the zero pressure gradient case. The reduction in shape factor is also found to be non-linear. However, the reduction is higher than for the zero pressure gradient case.

The results for distributed suction through a porous plastic or a perforated plate show similar results. Compared to slot suction, the effects near the region of suction are much more gradual. This is reflected by the local differences between distributed suction and local suction, for the pressure distribution and the integral parameters. However, downstream, where the local influences have vanished, the boundary layer development in terms of the integral parameters is equal for localised and distributed suction.

Concluding, the results in this report form a new source of information, which can be used in the application of boundary layer suction for engineering purposes. The obtained dataset also forms a valuable addition to the scarce data on suction of the turbulent boundary layer and can therefore be used for validation of numerical simulations.

Acknowledgements

This thesis forms the final effort to obtain a master's degree in aerospace engineering at the Delft University of Technology. I would like to thank the people who have supported me during my studies and in particular during this thesis research.

First of all I would like to thank my direct supervisors at the faculty, Dr. Ir. L.L.M. Veldhuis and Dr. Ir. B.W. van Oudheusden, for their feedback and guidance during the thesis research. Furthermore I would like to thank Dr. Ir. D. Ragni, for his support during the experimental campaigns and during the evaluation of the results, without which I would not have been able to accomplish this work.

I would also like to thank my colleages at Actiflow for their support and for giving me the opportunity to perform my thesis research in a fine working environment.

Last, but most certainly not least, I would like to express my gratitude to my parents, friends and especially my girlfriend, Steffie, for their continuous support during my studies.

Tim van der Hoeven

Contents

List of Figures

List of Tables

Nomenclature

Latin Symbols

A	Area	[m^{2}]
B	Turbulent wall-law intercept constant	[-]
C_f	Friction coefficient	[-]
C_p	Pressure coefficient	[-]
c_p	Specific heat at constant pressure	$[\mathrm{J} \cdot \mathrm{Kg}^{-1} \cdot \mathrm{K}^{1}]$
D	Pipe diameter	[m]
d	Depth of slot	[m]
D_h	Hydraulic diameter	[m]
f	Darcy friction factor	[-]
H	Shape factor	[-]
h	Channel height	[m]
k	Thermal conductivity	$[\mathrm{W} \cdot \mathrm{m}^{-1} \cdot \mathrm{K}^{-1}]$
l	Channel length	[m]
L_e	Entrance length	[m]
$\dot{m}$	Mass flow	$[\mathrm{Kg} \cdot \mathrm{s}^{-1}]$
N	Sample size	[-]
p	Pressure	[Pa]
Q	Volume flow	$[\mathrm{m}^{3} \cdot \mathrm{s}^{-1}]$
Re	Reynolds number	[-]
T	Temperature	[K]
t	Time	[s]
u	Velocity in x-direction	$[\mathrm{m} \cdot \mathrm{s}^{-1}]$
u^{+}	Dimensionless velocity in x-direction	[-]
v	Velocity in y-direction	$[\mathrm{m} \cdot \mathrm{s}^{-1}]$

v^*	Friction velocity	$[\mathrm{m \cdot s^{-1}}]$
V_w	Suction velocity	$[\mathrm{m \cdot s^{-1}}]$
W	Width of slot	[m]
w	Velocity in z-direction	$[\mathrm{m \cdot s^{-1}}]$
w'	Channel width	[m]
x	Streamwise position	[m]
y	Wall-normal position	[m]
y^+	Dimensionless wall-normal position	[-]
z	Spanwise position	[m]

Greek Symbols

β	Clauser's equilibrium parameter for pressure	[-]
ξ	Dimensionless pressure gradient	[-]
δ	Boundary layer thickness	[m]
δ^*	Displacement thickness	[m]
ϵ	Surface roughness	[m]
η	Dimensionless wall-normal distance	[-]
κ	Kármán constant	[-]
μ	Dynamic viscosity	$[\mathrm{N \cdot s \cdot m^{-2}}]$
ν	Kinematic viscosity	$[\mathrm{m^2 \cdot s^{-1}}]$
Π	Coles' wake parameter	[-]
ρ	Density	$[\mathrm{Kg \cdot m^{-3}}]$
σ	Suction coefficient	[-]
σ_f	Standard deviation of random variable, f	[-]
τ_w	Wall shear stress	[Pa]]
θ	Momentum thickness	[m]

Subscripts

∞	Freestream value
e	Boundary layer 'edge' value

Chapter 1

Introduction

Within the field of aerodynamics, boundary layer control is one of the most promising strategies for improving the aerodynamic characteristics of aircraft, cars and other objects moving through air. Boundary layer control is considered to be the generic term for all mechanisms or processes that make the boundary layer of a fluid flow deviate from its natural behaviour.[1] Boundary layer suction is one of these types of boundary layer control currently under investigation within the scientific community. Its relative simplicity as compared to other types of control, makes it one of the most viable applications of boundary layer control and thereby a very popular research topic. The possible applications of boundary layer suction range from commercial and military aircraft, to wind tunnels and also to wind turbines as will become clear shortly.

The specific topic of the research project presented in this thesis is the application of boundary layer slot suction to the turbulent boundary layer. This introductory chapter provides more detail on the specific motivation, goals and relevance of this research.

1.1 Background and Motivation

From the introductory statements in this chapter, one might already suspect that the topic of boundary layer suction is interesting from both a scientific and an engineering point of view. To illustrate that this is indeed the case, this section is divided into two subsections.

The first of the two following subsections, gives more background information on the specific application of boundary layer suction on wind turbine blades. Actiflow B.V., the company in collaboration with whom this research project is carried out, have already been studying this application of boundary layer suction. However, there is still quite some knowledge to be gained before this envisioned application can be turned into an actual engineering solution. This specific engineering problem has formed part of the motivation for the research described in this thesis.

A comprehensive literature review in [19] has revealed that the problem of boundary layer slot suction is certainly not yet fully understood within the scientific community. The second subsection, therefore briefly summarises the findings of this literature review. Moreover it mentions specific 'gaps in literature' that have been identified and which have formed the second part of the motivation for the current research.

---

[1] This definition is adapted from [13]

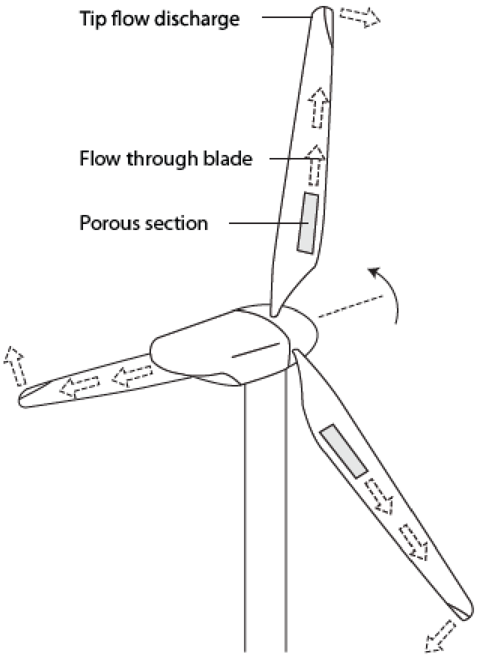

Figure 1.1: Concept of boundary layer suction at the root of the wind turbine blades [3].

1.1.1 Boundary Layer Suction on Wind Turbine Blades

In the current age of continuously increasing tendency towards the production of renewable energy, wind turbine design and optimisation is an important field of research. Considering horizontal axis wind turbines, the airfoil design at the root of the turbine blade is one of the specific challenges in the design and optimisation procedure. In the design of these airfoil sections a trade-off between the structural and aerodynamic properties must be made. In order to carry the loads transferred through the turbine blade, the sections at the root should preferably be as thick as possible. However, as the airfoil sections become increasingly thick, the aerodynamic properties deteriorate. Due to the high local velocities and thus low static pressures caused by the high thickness, the flow experiences very high adverse pressure gradients when the pressure recovery takes place. The (in)capability of the boundary layer to withstand these high pressure gradients before massive separation occurs, places a limit on the maximum lift generated by such a thick section.

Actiflow have been studying the use of boundary layer suction in order to prevent or delay separation and thus increase lift on this airfoil. In this concept, shown in figure 1.1, suction is accomplished passively by using the centrifugal motion of the fluid inside the turbine blade.

To find the optimal application of passive suction, Computational Fluid Dynamics (CFD) simulations and other numerical optimisations have been performed for airfoils with continuous boundary layer suction through a porous surface. The high structural loads at the root of the turbine blade, however, complicate the use of a porous plastic. Furthermore, contamination can cause significant reductions in suction effectiveness of the porous plastic.

An alternative option would be to use discrete suction in the form of suction through a slot in the surface of a non-porous material. This has some clear advantages over the use of a porous medium with respect to production and maintainability. However, localised suction through a slot involves much higher suction velocities, which results in different flow characteristics than for continuous suction. In order to improve the understanding of the effects of slot suction and its optimal use on their airfoils, a further investigation was therefore deemed necessary by Actiflow. In particular, this involves an investigation towards the application of boundary layer suction through a slot in order to prevent separation of the turbulent boundary layer in adverse pressure gradient conditions.

While this motivation from the engineering world has roughly set the scope for the investigation, a literature review has been carried out to find the specific gaps in knowledge on this topic. This is discussed in the following subsection.

1.1.2 Findings from Literature Review

The literature review in [19] has shown that the literature on the topic of boundary layer slot suction is very scarce. It has also shown that the available literature can be divided into two main research areas.

The first area consists of relatively fundamental research towards slot suction on a flat plate, mostly for low Reynolds numbers (i.e. $300 \leq \mathrm{Re}_\theta \leq 2000$). Experimental investigations at low Reynolds numbers have been performed in [1] [28] [10]. These have led to detailed descriptions of the effect of suction on the boundary layer in terms of mean velocity profiles and turbulence characteristics at discrete measurement locations in front of and beyond the location of suction. Furthermore, Direct Numerical Simulations (DNS), have been performed for the problem of slot suction by [29] and [23] giving insight in the streamwise development of the boundary layer with slot suction. However, due to the high computational effort required for DNS, these investigations were also limited to Reynolds numbers of $\mathrm{Re}_\theta \leq 600$. For this low Reynolds number realm, the qualitative and quantitative effects of slot suction are already quite well understood. In section 2.2.2 some of these results are discussed in more detail.

The second area consists mainly of research towards slot suction on a more applied level, on, for example, airfoils. These investigations are for higher Reynolds numbers (i.e. $\mathrm{Re} = \mathcal{O}(10^6)$), which are more representative for actual engineering problems. However, the results of these investigations are mainly given in terms of airfoil characteristics, like lift and drag. The influence of suction on the boundary layer is not specifically investigated.

Another interesting problem investigated in literature, is the application of slot suction on a wall mounted hump. For this problem, slot suction was used to reduce the size of a separation bubble caused by the shape of the hump. An experimental investigation for this problem ($\mathrm{Re} = \mathcal{O}(10^7)$) served as a benchmark during a CFD validation workshop in 2004 [33]. From this validation workshop, it has become clear that, although general correspondence was found, all numerical methods used were unable to reproduce the experimental results correctly, in a quantitative sense. The discrepancy between the numerical and experimental results is probably not only due to the presence of slot suction, but also due to the presence of separation. However, the author feels that this workshop still has clearly demonstrated the limitations of the 'current' numerical methods in predicting the effects of slot suction.

With respect to the influence of slot width, there are some contradictory findings in literature. Pierpont et al. [30] and Fage et al. [12] conclude that for a given suction rate, the width of the slot has no significant influence on effects of suction on the boundary layer. However, Williams et al. [46], who investigated the use of slot suction on a specifically designed airfoil, found that for a given amount of suction, the maximum lift coefficient was increased for a decreasing slot width.

From the literature review it has become clear that there is a need for research towards the effects of slot suction on the turbulent boundary layer at higher Reynolds numbers (i.e. Reynolds numbers more representative for real-world problems). Furthermore, the effects of slot suction on a turbulent boundary layer experiencing a non-zero pressure gradient, have not been quantitatively investigated in terms of boundary layer behaviour. It has also been shown that the numerical methods still need improvement in order to be able to predict the effects of slot suction correctly. To improve these methods, the addition of an experimental dataset to the very scarce collection of available validation data, is extremely valuable. Especially, experimental results which show the effect on the boundary layer upstream and downstream of the slot as well as the flow field near the slot, are deemed a good source for validation of computational methods.

1.2 Research Goals

The previous section has defined the context within which this research is carried out. Furthermore, specific gaps in the current knowledge on the subject of slot suction were pointed out. Based on this, the following general goal for the current research was defined:

To describe the effects of slot suction on a two-dimensional turbulent boundary layer experiencing an adverse pressure gradient, both qualitatively and quantitatively, by performing an experimental investigation at flow conditions relevant to both scientific interest and engineering applications.

This general goal has been divided into a number of more specific sub goals. These sub goals are:

- To determine the relation between the suction quantity and its effects on the boundary layer by performing measurements at different suction rates.
- To relate the effects of slot suction combined with an adverse pressure gradient to results for a zero pressure gradient boundary layer with slot suction, by performing measurements at both a zero and an adverse pressure gradient.
- To determine the effect of the width of the slot by comparing measurements using different slot widths.
- To put the results obtained for slot suction into a broader perspective by performing comparative measurements with distributed suction through a porous plastic and a perforated plate.
- To assess the quality of the dataset as a source for validation of computational methods, by performing an uncertainty analysis of the results.

The next section discusses the relevance of the research presented in this report. It explains how the envisioned outcomes from this report can be seen in a broader context.

1.3 Significance

Numerical tools can be very useful in the design and optimisation of, for example, airfoils with boundary layer suction. However, the tools will, obviously, only be useful if their predictions are accurately enough. In order to validate the accuracy of such tools it is important to have benchmark results. From the literature review it became clear that these benchmark results are very scarce and therefore the dataset created in this report will be an extremely valuable source of validation. To be able to use the dataset as a benchmark, it is very important to estimate the uncertainty within the results.

Next to that, the improved insights on the quantitative effects of slot suction for more application level Reynolds numbers are very important. This knowledge can first of all be used, again, in the design of airfoils with boundary layer slot suction. Especially the direct comparison with distributed suction in this report, gives additional information on the differences and similarities for both types of suction with respect to the external flow. This information possibly helps in deciding whether to use distributed or localised suction. Knowing the influence of slot width, similarly, is valuable with respect to future design considerations.

Finally, the results for suction at a high Reynolds number can be compared with the available literature on low Reynolds numbers. Possibly, a relation between these results can be established. From this, it might then be deduced, to what extent the low Reynolds number results are representative for the high Reynolds number case. The same holds for the combined effects of slot suction and an adverse pressure gradient. If these can be related to the zero pressure gradient case, it can be determined whether the available zero pressure gradient results can actually be extrapolated to 'predict' the effects of slot suction on a more applied level.

1.4 Outline of the Thesis

After this introductory chapter, chapter 2 provides more detailed background on the important concepts used and referred to in the remainder of the thesis. This includes theory related to the turbulent boundary layer and more detailed results from the literature review on boundary layer slot suction. Next to that it gives an explanation of the working principles of Particle Image Velocimetry (PIV), the main measurement method used during the experiments. Finally, the 'relevant flow conditions' for this experiment and the way these have been determined, is discussed.

Chapter 3 gives a detailed description of the experimental setup used during the research project. The post-processing steps applied to the raw results from the experiments are discussed in chapter 4.

In chapter 5 the results of the experimental investigation are presented and discussed. This includes validation by means of a comparison with both theory and literature, a qualitative discussion on the observed flow phenomena and an error analysis of the results. It must be noted that all results presented in this chapter, concern the effect of suction on the mean properties of the turbulent boundary layer. That is, a discussion of the turbulence properties is considered beyond the scope of this work, and is left for further research.

Finally, chapter 6 presents the most important conclusions based upon these results and the recommendations for further research. This chapter reviews the obtained results within the context of the original research goals.

Chapter 2

Theory and Background

This chapter reviews some important topics that are considered to be required knowledge to understand the contents of this report. It mostly discusses established theoretical concepts, but also presents more recent background information from literature.

The first section briefly reviews some theory related to turbulent boundary layers. The second section provides the reader with background information on the topic of boundary layer suction. The general principle of boundary layer suction is discussed and more detailed findings from the literature review on slot suction are highlighted. The third section discusses the main measurement method used during the experiment, Particle Image Velocimetry (PIV). Finally, the last section of this chapter describes the application of boundary suction on a thick airfoil, designed by Actiflow, for the use in wind turbine blades. The flow conditions for this specific engineering application have been taken into account during the design of the experiment.

2.1 Theory of a Turbulent Boundary Layer

A complete description of the theory related to turbulent boundary layers is obviously beyond the scope of this report. This section therefore reviews a selection of theoretical concepts related to the turbulent boundary layer which are used throughout the report. If the reader is already acquainted with boundary layer theory, it is advised to skip this subsection and use it as a reference. Most of the theory presented in this section is based on White [45].

2.1.1 Boundary Layer Characteristics

The boundary layer is the region close to a surface of a solid, past which a fluid with small viscosity flows. It has been demonstrated by Prandtl [31], that the viscous effects are confined to this thin region, while the flow outside this boundary layer behaves in an inviscid sense. The thickness of this layer, δ, is often conveniently expressed as the distance normal to the wall, where the velocity has reached 99 % of the freestream value. Besides the boundary layer thickness, generally, four main parameters are used for the characterisation of a boundary layer: the displacement thickness, the momentum thickness, the shape factor and the friction coefficient. These parameters and their physical meaning are briefly described in the upcoming paragraphs.

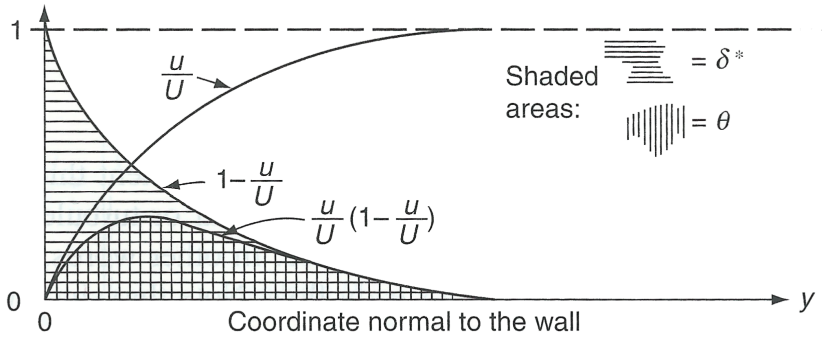

Figure 2.1: Displacement thickness and momentum thickness graphically displayed. Taken from [45].

Displacement thickness The displacement thickness can be described as a measure for the loss of mass as compared to the inviscid case, due to the presence of the boundary layer. Its definition is given in equation 2.1.

$$\delta^* = \int_0^\infty \left(1 - \frac{\overline{u}}{U_e}\right) dy \tag{2.1}$$

Momentum thickness The momentum thickness, similarly as for the displacement thickness, is a measure for the loss of momentum in the boundary layer as compared to the inviscid case. It is defined in equation 2.2.

$$\theta = \int_0^\infty \frac{\overline{u}}{U_e}\left(1 - \frac{\overline{u}}{U_e}\right) dy \tag{2.2}$$

In figure 2.1 the relation to the velocity profile and the value of δ^* and θ is graphically displayed. It can be seen that the displacement thickness is always larger than the momentum thickness.

Shape factor The shape factor, H, is defined as the ratio of the displacement thickness and the momentum thickness (equation 2.3). This parameter is very often used in the description of the state of a boundary layer. It is a measure of the 'fullness' of the boundary layer velocity profile and, from its definition, always has a value larger than 1.0.

$$H = \frac{\delta^*}{\theta} \tag{2.3}$$

For a flat plate turbulent boundary layer the shape factor typically has a value of $H \approx 1.3$. When the boundary layer experiences an adverse pressure gradient, the shape factor increases until separation occurs. The values of the shape factor, reported in literature, for which separation occurs, range between $2.3 \leq H \leq 4.1$, depending on the external flow conditions [36]. Figure 2.2 gives a graphical representation of the shape factor and its relation to the shape of the velocity profile.

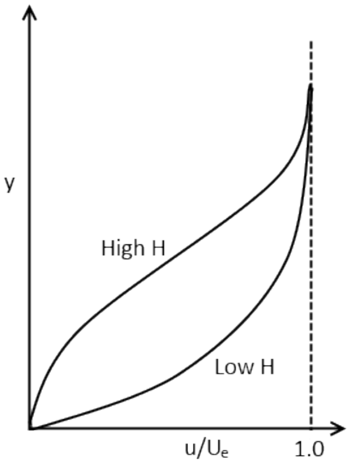

Figure 2.2: Relation between shape factor and the boundary layer velocity profile. Adapted from [42].

Friction coefficient As a result of a fluid having a non-zero viscosity, a shear stress acts on the surface past which the boundary layer flows. The magnitude of this shear stress is related to the viscosity of the fluid and the velocity gradient directly at the wall surface, as can be seen from equation 2.4.

$$\tau_w = \mu \left(\frac{\partial u}{\partial y} \right)_{y=0} \tag{2.4}$$

This stress can be non-dimensionalised by the freestream dynamic pressure, which results in a skin friction coefficient, as is done in equation 2.5.

$$C_f = \sqrt{\frac{\tau_w}{\frac{1}{2}\rho U_\infty^2}} \tag{2.5}$$

Although the above parameters do not give information on the turbulence characteristics explicitly, together, they give a good description of the mean character of the boundary layer. The effect of suction on the integral parameters will be one of the main topics in the discussion of the results in chapter 5.

2.1.2 Turbulent Boundary Layer Equations

Apart from defining the physical phenomenon ‘boundary layer’, Prandtl derived that within this region, a simplification of the general conservation laws can be applied, leading to ‘the boundary layer equations’. For the complete derivation of these equations the reader is referred to [45]. This section shows the results of these simplifications for a two-dimensional, incompressible turbulent boundary layer as well as the assumptions based on which these relations are derived.

The incompressible Reynolds averaged equations for mean continuity, mean momentum and mean thermal energy can be simplified towards the two-dimensional incompressible turbulent boundary layer equations. This simplification is based on the main assumption that the layer of shear is ‘thin’, which is true for $\mathrm{Re}_x \gg 1$. Following from this assumption, a number of inequalities are derived, which result in a drop out of terms in the conservation laws. The inequalities, or boundary layer approximations, are given by:

$$\begin{aligned} \delta(x) &\ll x \\ \bar{v} &\ll \bar{u} \\ \frac{\partial u}{\partial x} &\ll \frac{\partial u}{\partial y} \\ \frac{\partial v}{\partial x} &\ll \frac{\partial v}{\partial y} \end{aligned} \tag{2.6}$$

The assumption of two-dimensionality in the mean flow comes down to: $\bar{w} = 0$ and $\frac{\partial}{\partial z} = 0$. Taking all these assumptions and inequalities into account, this results in the following two-dimensional incompressible boundary layer equations for the mean flow:

$$\frac{\partial \overline{u}}{\partial x} + \frac{\partial \overline{v}}{\partial y} = 0 \tag{2.7a}$$

$$\overline{u}\frac{\partial \overline{u}}{\partial x} + \overline{v}\frac{\partial \overline{u}}{\partial y} \approx U_e\frac{dU_e}{dx} + \frac{1}{\rho}\left(\frac{\partial \tau}{\partial y}\right) \tag{2.7b}$$

$$\rho c_p\left(\overline{u}\frac{\partial \overline{T}}{\partial x} + \overline{v}\frac{\partial \overline{T}}{\partial y}\right) \approx \frac{\partial q}{\partial y} + \tau\frac{\partial \overline{u}}{\partial y} \tag{2.7c}$$

where

$$\begin{aligned} \tau &= \mu\frac{\partial \overline{u}}{\partial y} - \rho\overline{u'v'} \\ q &= k\frac{\partial \overline{T}}{\partial y} - \rho c_p\overline{v'T'} \end{aligned} \tag{2.8}$$

and where $U_e(x)$ is the velocity outside the boundary layer. It should be noted that q and τ contain additional terms as compared to the laminar boundary layer equations. These terms represent additional heat flux and shear stress caused by to turbulent structures in the boundary layer. These additional unknown terms are to be modelled in order to have closure of this mathematical problem. Furthermore the momentum equation in y-direction results in the conclusion that $\frac{\partial p}{\partial y} \approx 0$. This means that the freestream pressure equals the wall pressure and that the pressure only varies in streamwise direction, i.e. $p = p(x)$. This result has been used in equation 2.7b to express the streamwise pressure gradient, $\frac{\partial p}{\partial x}$, in terms of the velocity outside the boundary layer, $U_e(x)$.

Integral momentum equation

The differential boundary layer equations, presented in the previous section, can be combined and subsequently integrated across the boundary layer to arrive at the integral momentum equation. This equation, first derived by von Kármán [21], gives a relation between the boundary layer integral parameters earlier described:

$$\frac{d\theta}{dx} + (2 + H)\frac{\theta}{U_e}\frac{dU_e}{dx} = \frac{\tau_w}{\rho U_e^2} = \frac{C_f}{2} \tag{2.9}$$

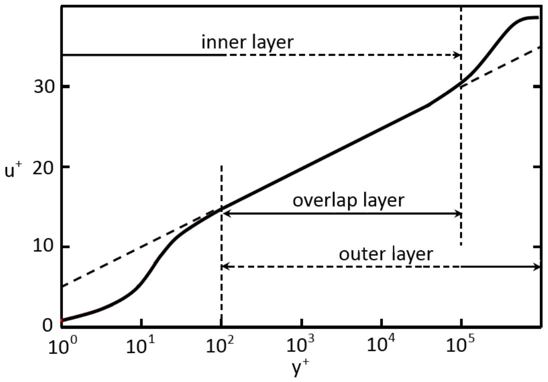

Figure 2.3: Inner, outer and overlap layer for a typical turbulent boundary layer velocity profile.

From equation 2.9 it can be seen that, if the external pressure gradient is zero (i.e. $\frac{dU_e}{dx} = 0$), the rate of change of the momentum thickness is directly related to the friction coefficient in a two-dimensional boundary layer. This fact, and equation 2.9 as a whole, are used during the analysis of the results in this report. Later, in section 2.2.1 this relation is presented in the case of a non-zero wall-normal velocity at the wall.

2.1.3 Mean Velocity Profile

In general, a turbulent boundary layer velocity profile consists of three regions. Close to the wall there is the 'inner' layer, where the shear forces due to viscosity dominate the flow behaviour. On the other hand, the upper part of the boundary layer, the 'outer' layer, is dominated by the turbulent shear. These two layers are connected by an intermediate layer, called the 'overlap' layer [45]. Figure 2.3 shows these regions for typical velocity profile of a turbulent boundary layer.

Dimensional analysis of the governing parameters in these three layers, together with experimental results have led to general laws describing the velocity profile in these three layers. All of these laws are based on non-dimensional velocity profiles. The friction velocity, v^*, is the appropriate scale for non-dimensionalisation of both the streamwise velocity and the wall-normal distance. Its definition is given below, in equation 2.10.

$$v^* = \sqrt{\frac{\tau_w}{\rho}} = U_\infty \sqrt{\frac{C_f}{2}} \tag{2.10}$$

The non-dimensionalised streamwise velocity and wall-normal distance result in the definition of the following 'plus-units':

$$u^+ = \frac{u}{v^*} \tag{2.11a}$$

$$y^+ = \frac{y v^*}{\nu} \tag{2.11b}$$

The upcoming paragraphs present which correlations, based on these plus-units, are used in this report to describe the different parts of the velocity profile. Please note there are alternative correlations available in literature, which are not mentioned in this report.

Inner layer velocity law (Spalding's law of the wall)

Spalding [37] has derived a single equation for the inner layer as well as the overlap layer. This equation has shown to give an excellent fit to experimental data and is defined by:

$$y^+ = u^+ + e^{-\kappa B}\left[e^{-\kappa u^+} - 1 - \kappa u^+ - \frac{(\kappa u^+)^2}{2} - \frac{(\kappa u^+)^3}{6}\right] \tag{2.12}$$

White [45] considers this law 'a complete success for smooth-wall turbulent flow'.

Overlap layer velocity law (logarithmic law)

In the overlap layer, the dimensional analysis has shown that the velocity profile should be described by a logarithmic relation. This logarithmic relation, in terms of the inner layer variables, is given in equation 2.13.

$$\frac{\bar{u}}{v^*} = \frac{1}{k} ln(\frac{yv^*}{\mu}) + B \tag{2.13}$$

Here, κ and B are constants which are determined experimentally. $\kappa = 0.41$ and $B = 5.0$ are the most commonly used constants and are also used in this report. The logarithmic law is considered to be universally applicable to turbulent flow past smooth, impermeable walls. Its universality is also found to be useful in determining the friction coefficient of a boundary layer with a given velocity profile. This will be demonstrated in section 2.1.4.

Outer layer velocity law (Coles' law of the wake)

Coles' law of the wake describes the outer part of the velocity profile very precisely. It combines the logarithmic law with an additional wake function to account for the outer layers' deviation from the log law. The wake function is often described as a sine function or a polynomial. In this report the polynomial function has been used,

$$f(\eta) \approx 3\eta^2 - 2\eta^3 \tag{2.14}$$

where the dimensionless quantity η is described by: $\eta = y/\delta$. This wake function is added to the logarithmic law from equation 2.13 as follows:

$$u^+ \approx \frac{1}{\kappa} ln(y^+) + B + \frac{2\Pi}{\kappa}(3\eta^2 - 2\eta^3) \tag{2.15}$$

Here, Π is called Coles' wake parameter, which is determining for the strength of the wake component. Typically, for zero pressure gradient turbulent boundary layer this parameter is found to be $\Pi \approx 0.5$, while for adverse pressure gradient boundary layers its value can easily rise to 10 or more [45]. This equation is very valuable, as it gives a fair approximation of nearly the entire velocity profile (excluding only the viscous sublayer), with or without the presence of a pressure gradient.

Integrating equation 2.15 across the boundary layer results in the following approximate relations between the integral parameters, the friction coefficient and the wake parameter:

$$\begin{aligned}\frac{\delta^*}{\delta} &\approx \frac{1+\Pi}{\kappa\sqrt{2/C_f}} \\ \frac{\theta}{\delta} &\approx \frac{\delta^*}{\delta} - \frac{2+3.2\Pi+1.5\Pi^2}{\kappa^2(2/C_f)}\end{aligned} \tag{2.16}$$

Again, please note, that the general laws described above, are only correlations resulting from dimensional analysis, while no actual flow equations have been solved. However, due to their good correspondence with experimental data, it is believed that these laws are a good source for validation of two-dimensionally smooth turbulent boundary layers with, or without, a pressure gradient

2.1.4 Estimating the Friction Velocity

Previously it has already been mentioned that the friction coefficient is a physically important characteristic of the boundary layer. Next to that, it is also included in the definition of the friction velocity, which is an important parameter for the non-dimensionalisation of the velocity profile.

It has also been shown that the wall shear force, and thus the friction coefficient, is determined by the velocity gradient at the wall (see equations 2.4 and 2.5). Although it would theoretically be possible to determine this velocity gradient from near-wall measurements, this often is very hard and an alternative way of deducing the friction coefficient is required. One method to do so, relies on the universality of the logarithmic law described in section 2.1.3 and uses a so-called ‘Clauser plot’.

Using the definition of the friction velocity in equation 2.10, one can rewrite the logarithmic law in equation 2.13 as follows:

$$\frac{\bar{u}}{U_\infty} = \frac{C_f}{2}\left[\frac{1}{k} ln\left(\frac{Re_y\sqrt{\frac{C_f}{2}}}{\mu}\right) + B\right] \tag{2.17}$$

Here, Re_y is the Reynolds number based on the wall-normal distance, y. From equation 2.17 one can see that, for a given C_f, there is an explicit relation between the normalised velocity $\frac{u}{U_\infty}$ and the Reynolds number, Re_y. The Clauser technique simply involves plotting this relation for a range of values of C_f and finding the one matching the logarithmic part of the measured velocity profile best. Figure 2.4 schematically shows how this technique works.

Next to the Clauser technique, the friction coefficient can also be approximated using the results from Coles' law of the wake. If we evaluate equation 2.15 at the edge of the boundary layer, a relation between C_f, Π and Re_δ is obtained:

$$\sqrt{\frac{2}{C_f}} = \frac{1}{\kappa} ln\left(\frac{Re_\delta}{\sqrt{2/C_f}}\right) + B + \frac{2\Pi}{\kappa} \tag{2.18}$$

Combining equation 2.18 with 2.16 results in an implicit relation between the friction coefficient, C_f, the shape factor, H, and the Reynolds number, Re_θ. Based on this relation, White presents

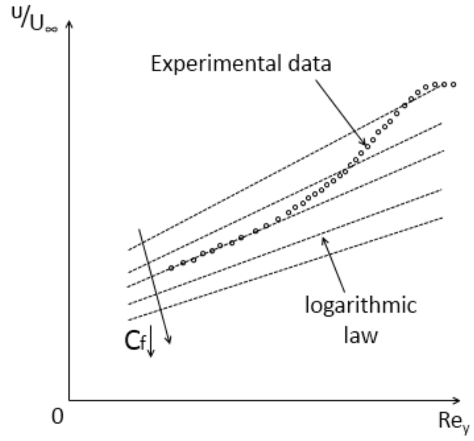

Figure 2.4: Schematic demonstration of Clauser plot. Note that the x-axis has a logarithmic scale.

a correlation for determining the friction coefficient, which is given in equation 2.19.

$$C_f \approx \frac{0.3e^{-1.33H}}{(log_{10}Re_\theta)^{1.74+0.31H}} \tag{2.19}$$

This correlation is found to give a ± 3% accurate fit to the friction coefficient obtained from Coles' law of the wake.

Having covered the theoretical concepts used throughout this report, regarding 'normal' turbulent boundary layers, the effects of suction on a turbulent boundary layer will be elaborated on in the next section.

2.2 Boundary Layer Suction

This section aims to give more background information on the topic of boundary layer suction. The theory related to this is much more scarce as compared to the theory for 'normal' boundary layers. The first subsection discusses the general working principle of boundary layer suction. The second subsection highlights some detailed results found from the literature review on boundary layer slot suction in [19]. These results will be referred to in the discussion of the results.

2.2.1 Principle of Boundary Layer Suction

As already mentioned in the introduction of this thesis, boundary layer suction is one of many types of flow control. Just as for other types of flow control, boundary layer suction can be used for multiple purposes. The interrelation between different flow control goals in general, is well described in [13] and summarised in figure 2.5.

As mentioned earlier, the engineering problem motivating the current research, concerns boundary layer suction to prevent separation of the turbulent boundary layer. It can be observed from figure 2.5 that separation leads to a loss of lift and an increased form drag. By controlling the

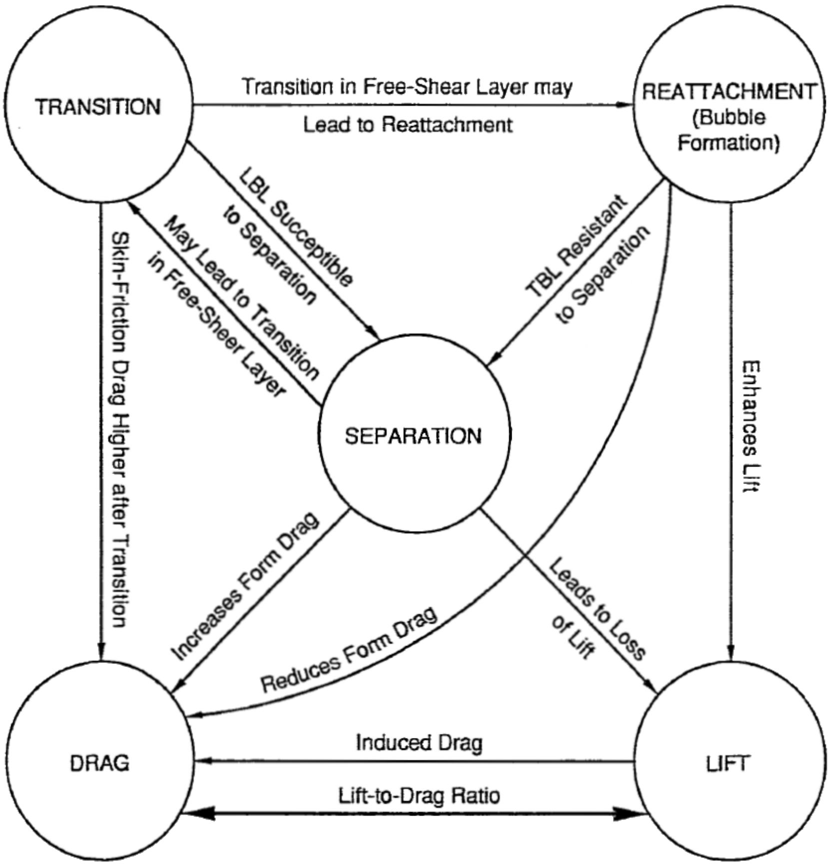

Figure 2.5: The interrelation between different flow control goals. Image taken from [13].

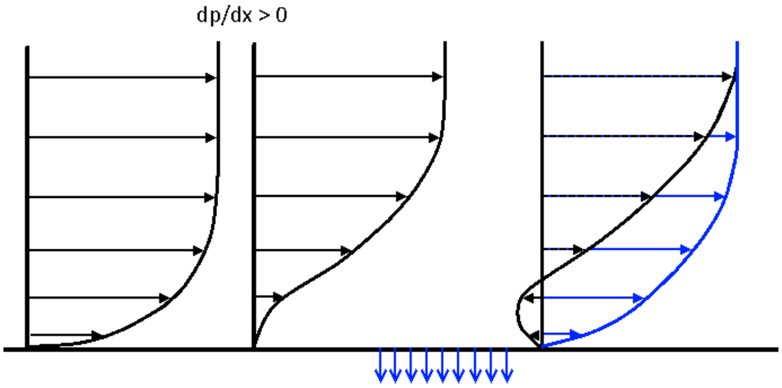

Figure 2.6: Schematic representation of effect of suction on the shape of the boundary layer.

separation behaviour of the boundary layer, one can therefore favourably influence the drag and lift characteristics of, for example, an airfoil.

In order to explain the working principle of boundary layer suction, let us recall what drives a boundary layer to separation: an adverse pressure gradient. In section 2.1.1, it was already stated that a boundary layer will separate if its shape factor rises beyond a certain critical value of H. It was also stated that an adverse pressure gradient causes the shape factor to increase. In order to prevent separation, the effect of an adverse pressure gradient should be opposed. More specifically, the velocity profile should remain such that its shape factor does not increase beyond this critical value.

Boundary layer suction helps modifying this velocity profile by withdrawing the low velocity fluid near the wall. By doing so, the boundary layer becomes ‘fuller’ and thus the shape factor decreases. Figure 2.6 schematically shows the effect of suction on a boundary layer which would normally separate.

Similarly to the von Kármán integral relation in 2.9 the integral momentum equation, including a wall-normal velocity can also be derived [13].

$$\frac{d\theta}{dx} - \frac{V_w}{U_e} + (2+H)\frac{\theta}{U_e}\frac{dU_e}{dx} = \frac{\tau_w}{\rho U_e^2} = \frac{C_f}{2} \tag{2.20}$$

Here, V_w is the-wall normal velocity, being negative in the case of suction. From equation 2.20, it can be observed that wall suction indeed has an opposite effect to the adverse pressure gradient. For an adverse pressure gradient, the term involving $\frac{dU_e}{dx}$ becomes negative, while $-\frac{V_w}{U_e}$ becomes positive, for suction.

While this adapted form of the momentum integral equation shows that suction indeed opposes the negative effects of an adverse pressure gradient, it cannot be applied to the problem of slot suction. In fact, equation 2.20 is a result of a series of mathematical operations to the turbulent boundary layer equations in equation 2.7. The boundary layer approximations on which these are based, become invalid when localised suction, with a high wall normal velocity, is applied. That is, the maximum suction velocity V_w for which the approximations remain valid, is in the order of $U_\infty\ \mathrm{Re}_x^{-1/2}$ [36]. This corresponds to a suction velocity of approximately 0.3 to 1 % of the freestream velocity for $\mathrm{Re}_x = 10^6$ to 10^7. Since for slot suction this velocity can easily be two orders of magnitude higher, we have to rely on data from experiments and simulations, instead of theoretical approximations.

2.2.2 Slot Suction in Literature

An elaborate literature review on the subject of slot suction of the turbulent boundary layer can be found in [19]. This section summarises the most important findings from this literature review, which will be referred to during the analysis of the results.

In this report, the following dimensionless parameter is used to describe the suction rate:

$$\sigma = \frac{V_w W}{U_\infty \theta_0} \tag{2.21}$$

Here, V_w is the suction velocity, W is the slot width, and θ_0 is the momentum thickness at the location of the slot in the absence of suction. Physically, this parameter can be interpreted as the ratio of momentum flux loss due to the suction and the actual momentum flux of the incoming boundary layer at the location of the slot [1].

Antonia et al. [2] experimentally investigated the possible effect of relaminarisation for high suction rates ($2.6 \le \sigma \le 6.5$) through a small porous strip. For this investigation, the Reynolds number, based on the momentum thickness at the location of the slot, was calculated to be $\mathrm{Re}_\theta \approx 580$. At different streamwise positions, velocity profiles were obtained with the use of hotwire measurements. Behind the porous strip, where the local effects were diminished, they found a linear relation between the decrease in Re_θ with σ. The shape factor was found to increase nonlinearly with σ. The fact that an increase of H with σ was observed by Antonia et al, can be explained by the very high suction rates used, causing partial relaminarisation. Typically, the shape factor for a laminar boundary layer is higher than for a turbulent boundary layer.

Park et al. [29] have performed a direct numerical simulation of a spatially developing boundary layer with suction and blowing through a slot. The Reynolds number based on the displacement thickness and freestream velocity at the inlet of the domain was $\mathrm{Re}_{\delta^*} = 500$. For three suction rates within the range $0.09 \le \sigma \le 0.45$, results are presented for both the mean and turbulent characteristics of the boundary layer. The results from Park et al. are a valuable source of validation for the results in the current experiment. They are the only one to present figures with a continuous streamwise development of the integral parameters.

Figure 2.7 shows the effect of slot suction on the streamwise development of the dimensionless wall pressure [29]. In the same fashion, figure 2.8 shows the effect of slot suction on the streamwise development of the momentum thickness. Both quantities show a typical pattern, with a minimum in front of the slot, a rapid increase over the slot and a maximum rearward of the slot.

Kim et al. [22] have, similarly to Park et al., performed a DNS of the turbulent boundary layer with localised suction, for $\mathrm{Re}_\theta = 300$. In this investigation, the emphasis was on the effect of suction on the wall pressure, and the wall pressure fluctuations. The effect on the mean wall pressure found by Kim et al. was similar to the one by Park et al. presented in figure 2.7.

Contrary to the findings of Antonia et al., Park et al. find that there is a weak non-linear decrease of the Reynolds number, Re_θ for an increasing amount of suction, σ. Furthermore, they also find a non-linear decrease in the shape factor, H, instead of an increase found by Antonia et al. The latter can easily be explained by the lower suction rates used by Park et al., for which no relaminarisation effects occurred.

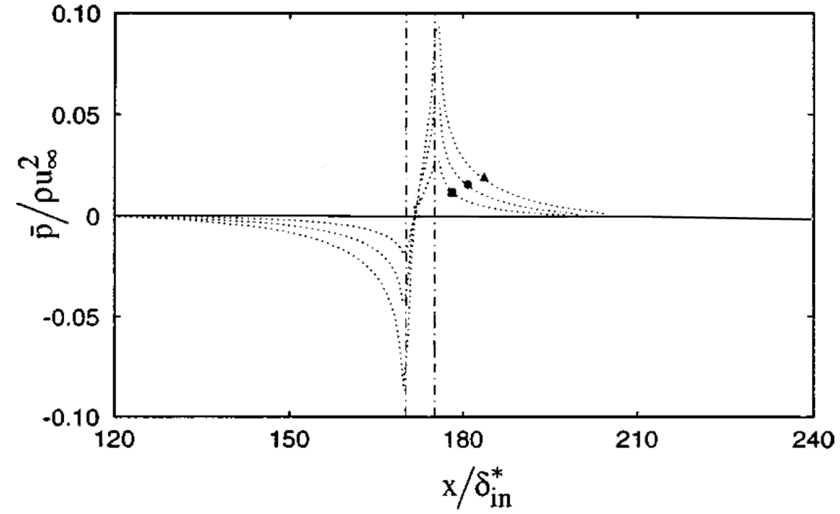

Figure 2.7: Variations of the mean pressure at the wall due to slot suction observed by Park et al. [29]. The figure has been adapted to show the result for suction only. ■: $\sigma = 0.09$, •: $\sigma = 0.225$, ▲: $\sigma = 0.45$. Chain-dotted lines show the location of the slot.

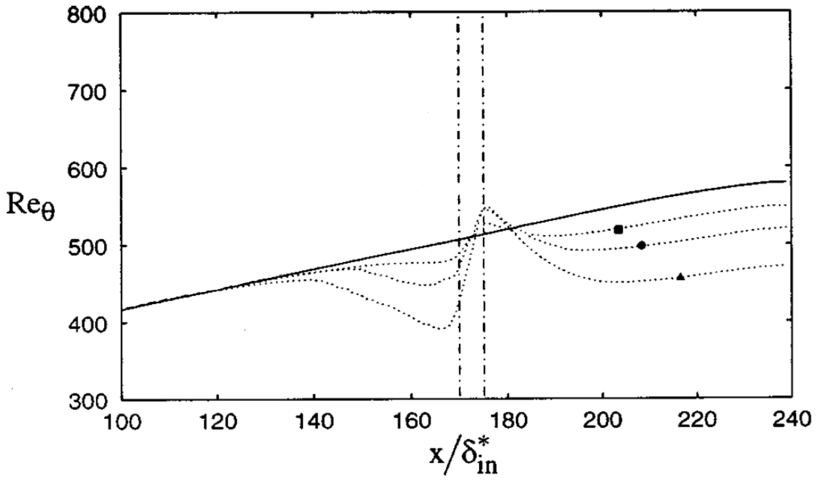

Figure 2.8: Variations of the Reynolds number based on the momentum thickness due to slot suction observed by Park et al. [29]. The figure has been adapted to show the result for suction only. ■: $\sigma = 0.09$, •: $\sigma = 0.225$, ▲: $\sigma = 0.45$. Chain-dotted lines show the location of the slot.

2.3 Particle Image Velocimetry

PIV is currently one of the most popular experimental techniques used for aerodynamic research. The most common PIV technique allows to reproduce a two-dimensional instantaneous vector field, while more advanced techniques are also able to reproduce a three-dimensional vector field. Its ability to reproduce an entire vector field is one of the main advantages over other measurement techniques, which often involve measuring single data points. Next to that, its non-intrusiveness is another important advantage.

This section briefly describes the principles of planar PIV, the technique used for the experiment described in this report. Furthermore, some important requirements for obtaining proper quality results are discussed.

The general principle behind particle image velocimetry will be explained with figure 2.9 taken from [32]. All different elements needed for a PIV experiment are depicted in this figure and will now be discussed briefly.

First of all tracer particles should be added to the flow under investigation. A light sheet is formed by a laser combined with the proper optics (lenses/mirrors) which illuminates all tracer particles within a two-dimensional plane. The light scattered by these particles is captured by a digital camera, equipped with a proper lens. This process of illumination and image capturing is done twice with a time interval Δt. The magnitude of this time interval is selected based on the mean velocity of the flow and the magnification of the image, as will be explained later. The two images obtained by this procedure show a pattern of tracer particles slightly displaced from time t to t'.

The processing consists of performing a cross-correlation between the two successive images. Before doing this correlation, the images are divided into smaller regions called interrogation windows. For each of these windows, the cross-correlation results (if the PIV is carried out correctly) in a correlation peak, corresponding to the average displacement of the particles within that window. Together with the information on the time delay between the two images, Δt, this results in one velocity vector for each of the correlation windows. The final result is a vector field of which the resolution is determined by the size (and possible overlap) of the interrogation windows.

There are numerous important issues to take into account when setting up the PIV experiment and performing the post-processing. The most important and relevant ones, for the investigation described in this report, will be briefly discussed below. For a complete description of the physical and mathematical theory underlying this experimental method, the reader is referred to [32].

2.3.1 Interrogation Window Size

As mentioned above, the cross-correlation procedure results in one velocity vector for each interrogation window. In order to have a high spatial resolution, one would therefore want to use as small interrogation windows as possible. However, when decreasing the size of the interrogation window, there is an important PIV post-processing rule to take into account.

This rule states that for proper accuracy, the interrogation window size should be such that the average particle displacement remains below $1/4^{\text{th}}$ of the window size [35]. Otherwise, a large part of the particles recorded in the first image, are already moved out of the correlation window for the second image. This makes it harder to find the correct correlation between the two. Coming back to the earlier statement, the time interval between the two images can now be chosen such that for a given velocity, magnification and window size, this design rule is obeyed. That is, the smaller the desired interrogation window, the smaller the maximum allowed pixel displacement and thus the smaller the time interval between the images. Unfortunately, decreasing the pixel displacement, also decreases the accuracy with which the correlation peak can be determined (more detail in section 5.6.1). To obtain a result with high accuracy as well as high spatial resolution, the solution is found in a multi-pass correlation procedure.

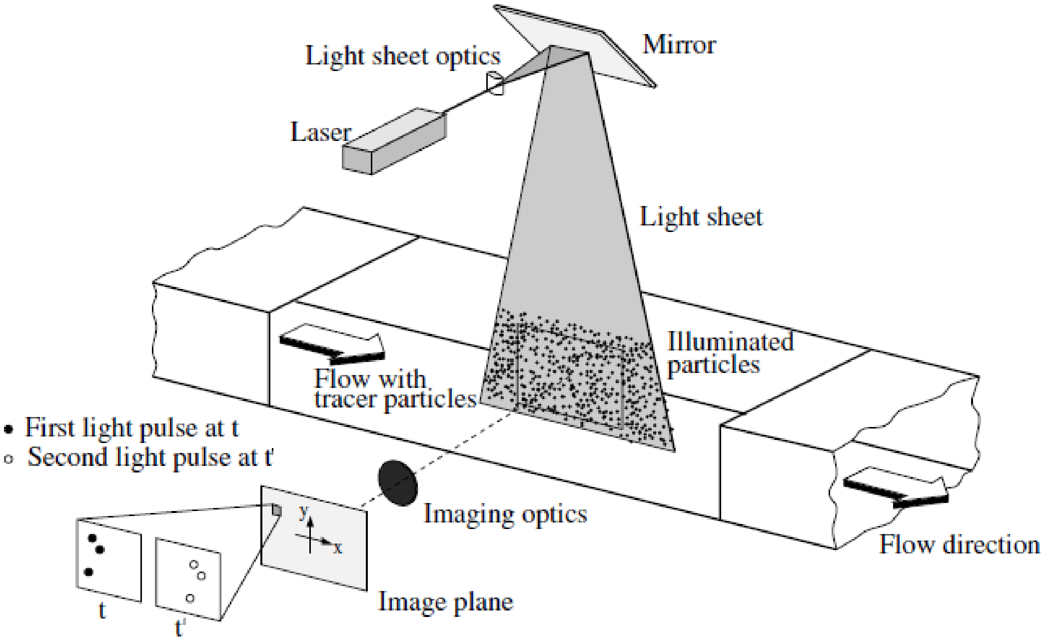

Figure 2.9: General experimental setup for a planar PIV measurement. Taken from [32].

By performing multi-pass correlation, the accuracy of large interrogation window sizes is combined with the high spatial resolution related to small interrogation window sizes. From the first correlation pass, the main motion of the velocity field is determined with high accuracy. Subsequently, this information is used to apply a shift to the smaller interrogation windows, to ensure that the same region of particles is correlated. This process continues until the final window size is reached.

An additional option in the correlation procedure, is to use an overlap of the interrogation windows. By using window overlap, the spatial resolution is increased even further, at the expense of additional computation time. Furthermore it should be taken into account that the additionally obtained vectors are correlated to the neighbouring vectors, as part of the pixels are being 'reused'.

Finally, there is also the option to use non-square interrogation windows. If the velocity gradients in one direction are much smaller as compared to another, the accuracy can be improved by stretching the interrogation window according to these velocity gradients. For example, in the boundary layer, where $\frac{\partial}{\partial x} \ll \frac{\partial}{\partial y}$, the interrogation windows could then be stretched in x-direction. This way, the correlation is based on more particles, which improves accuracy.

2.3.2 Sub-Pixel Precision and Peak Locking

A crucial aspect of PIV is the ability to determine the location of the correlation peak on a subpixel level. This section briefly explains how this is possible and what the consequences are for the accuracy of the results.

In order to find the average particle displacement in one interrogation window, the data from the two subsequent images, in this window, is shifted in two directions. For each of these shifts a cross-correlation is performed. All these correlation values, together form a correlation map with a peak near the shift corresponding to the mean pixel displacement of the particles. Since the optical information obtained from a camera is discretised over the pixels on the camera sensor, the correlation can only be performed for integral shifts [32].

If one would simply select the pixel shift with the highest correlation value to be the actual particle displacement, the accuracy of the results would be limited to 1 pixel. However, instead of picking the highest value in the correlation map, one could also consider the entire peak formed locally, due to the relatively high correlation values on the surrounding pixels. If one fits a Gaussian fit through this peak, the location of the correlation peak can be determined at a sub-pixel level, decreasing the uncertainty to approximately 0.1-0.2 pixels [35].

In order for this Gaussian fit procedure to work well, the correlation peak should be quite narrow, which is ensured by having the individual particles being distributed over 2-3 pixels. If the particles are too much out of focus, covering more than 3 pixels, the correlation values will become increasingly smeared out, making it difficult to find an actual peak. On the other hand, if the particles are only the size of one pixel, the correlation peak will also be concentrated at one pixel, while the correlation value of the surrounding pixels is covered in noise [32]. As the peak now is locked at an integer value, the uncertainty within the result increases by a factor of 10, to approximately 1 pixel again.

In order to get the best accuracy for the PIV results, it is therefore very important to have the individual particles properly distributed over two to three pixels.

2.3.3 Other Sources of Error

This section briefly discusses two additional sources of error in PIV measurement, taken into account during the current experiment. The first one is related to three dimensional effects in the flow field, while the second one is related to high spatial velocity gradients.

When there is a three dimensional component in the velocity field, this might cause an additional error, or reduction of the accuracy, of the PIV measurements. Due to the presence of an out of plane velocity component, particles that are illuminated on the first image, might be moved out of the laser sheet on the second image. Similarly to the case of too high in plane displacement, there are fewer particles that actually contribute to the proper correlation peak. To have good accuracy of the results, the maximum out of plane particle displacement should therefore be less than $1/4^{\text{th}}$ of the laser sheet thickness [35].

Another source of uncertainty is the presence of high velocity gradients within the correlation window. This issue is especially applicable to turbulent boundary layer flows, where, often, a very high velocity gradient is present near the wall. For PIV of a turbulent boundary layer, now consider the interrogation window for the part directly above the wall. Due to the high velocity gradient, there is a large difference between the particle displacement near the top of that interrogation window and near the wall. Since there is a large range of particle displacements, there will not be a clear peak within the correlation map, thereby causing a lower signal to noise ratio.

Furthermore, the obtained near-wall velocity is also possibly biased towards a higher value. This is the result of the multi-pass procedure described above. As explained above, the information on the displacement obtained from the large interrogation windows, is used to give an initial shift to the smaller interrogation windows.

As an example, now assume a 16 x 16 pixels interrogation window, again directly above the wall, which gets an initial shift of 10 pixels. The high velocity near the top of this window causes the particles to have a displacement close to the 10 pixels. However, the near-wall particles, which have very low velocity, might only have a displacement of 1 or 2 pixels. This means that due to the initial shift, the particles with low velocity are not present in the shifted interrogation window, while the high velocity particles are. This causes the correlation peak to be biased to the larger displacement, and thus a higher velocity. Note that this problem is aggravated when a larger particle displacement for the high velocity values is used. A possible solution for this problem is the use of deformed interrogation windows, of which the shape is based on the velocity gradient.

Summarising, this section has described the basic principles of PIV as well as some specific practical guidelines for obtaining proper PIV results. The discussion above is obviously not complete, but it does state the most important concepts, that were taken into account during the PIV measurements and the post-processing of the results.

2.4 Boundary Layer Suction on Wind Turbine Airfoil

This section briefly describes the application of boundary layer suction on wind turbine blades, as already introduced in chapter 1. It was already stated that Actiflow has been using numerical tools as well as experimental investigations in order to investigate the use of suction on thick airfoil sections.

Figure 2.10 shows the shape of the AF-0901 airfoil designed by Actiflow. This airfoil has specifically been designed for the application of distributed boundary layer suction to prevent separation. When increasing the angle of attack, in order to gain lift, this airfoil, finally, suffers from trailing edge stall. This is a typical behaviour for airfoils with a large leading edge radius and a strong upper surface curvature [27] as illustrated in figure 2.10. As the angle of attack is further increased, the separation point moves further upstream causing a reduction in lift. In order to increase the angle of attack at which stall occurs, boundary layer suction can be used to postpone separation.

For this airfoil, Actiflow has built and tested a wind tunnel model, to validate the findings from the optimisation tools. During the design of the current experiment, the typical boundary layer characteristics for the AF-0901 wind tunnel model have been taken into account. In [19], an analysis for the AF-0901 airfoil has been carried out, using Xfoil. From this analysis it was found that, for the wind tunnel airfoil model, the typical Reynolds number at the envisioned location of suction is $Re_\theta \approx 10{,}000$. The pressure coefficient was also calculated in terms of Clauser's equilibrium parameter, given by:

$$\beta = \frac{\delta^*}{\tau_w}\frac{dp_e}{dx} \tag{2.22}$$

Using equation 2.22 it was found that in the pressure recovery zone, the pressure gradient increased from $\beta = 2$ to $\beta = 50$, before it would very rapidly increase to infinity due to the shear stress going to zero at separation. Furthermore, it was also calculated that for the wind tunnel tests already carried out for continuous suction, the maximum suction coefficient used was approximately $\sigma = 0.4$. The upcoming chapter will describe the experimental setup, that has been used to approach the above flow conditions as good as possible.

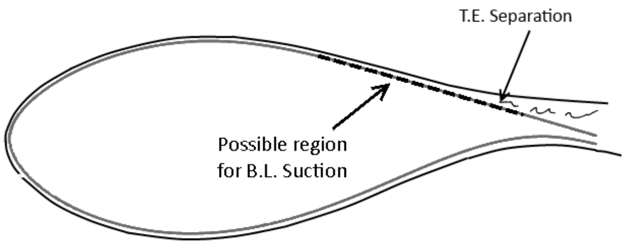

Figure 2.10: Typical application of suction on AF-0901 Airfoil to prevent or postpone separation.

Chapter 3

Experimental Setup

This chapter detailedly describes the experimental setup that has been used to obtain the results presented in this thesis. The experimental setup has been designed to be able to approach the flow conditions described in section 2.4 as good as possible. In the first section of this chapter, the flow facility and the general experimental setup are discussed. The second section discusses the measurement campaigns and the general measurement procedure followed during these campaigns. The third section focusses on the suction system including the slot shape, the suction chamber and the method to determine the suction quantity. The parts of the experimental setup related to the PIV measurements, the pressure measurements and the hotwire measurements are discussed in the fourth, fifth and last section respectively.

3.1 General Setup

As has been stated in the introductory chapter of this report, the goal of this experimental research project is to quantitatively and qualitatively describe the effect of slot suction on the turbulent boundary layer experiencing an adverse pressure gradient. A feasibility study comparing the use of different flow facilities and test setups to reach this goal has been performed in [19]. Based on this study it was decided to perform the experiment at the W-Tunnel facility at the Delft University of Technology (DUT). The W-tunnel is an open circuit low turbulence wind tunnel with a $0.4 \cdot 0.4$ [m^2] nozzle. The feasibility study showed that using the W-tunnel and the boundary layer growing from the wall of this tunnel together with a proper setup is a good manner to achieve the desired research goal. The setup offers flexibility with respect to testing at different pressure gradients and allows a boundary layer investigation at the relevant conditions (i.e. $\mathrm{Re}_\theta \approx 10{,}000$).

A schematic overview of the general setup used during the experiment can be observed in figure 3.1. Basically, the setup behind the tunnel consisted of two main parts. The first part was a straightforward extension of the tunnel nozzle, allowing the boundary layer at the wall of the tunnel to develop to the desired thickness. The second part consisted of the wall including an insert with the suction medium, and an opposing, movable, wall with multiple slots in it. Creating a diverging channel with this movable wall allowed to investigate the slot suction characteristics at different pressure gradients. At the end of the tunnel a fine meshing could be used to create a positive pressure difference between the tunnel and its surroundings. By this overpressure, natural boundary layer suction at the diverging wall could be obtained. This helped reaching higher diffusor angles without having flow separation. At the location of boundary layer suction,

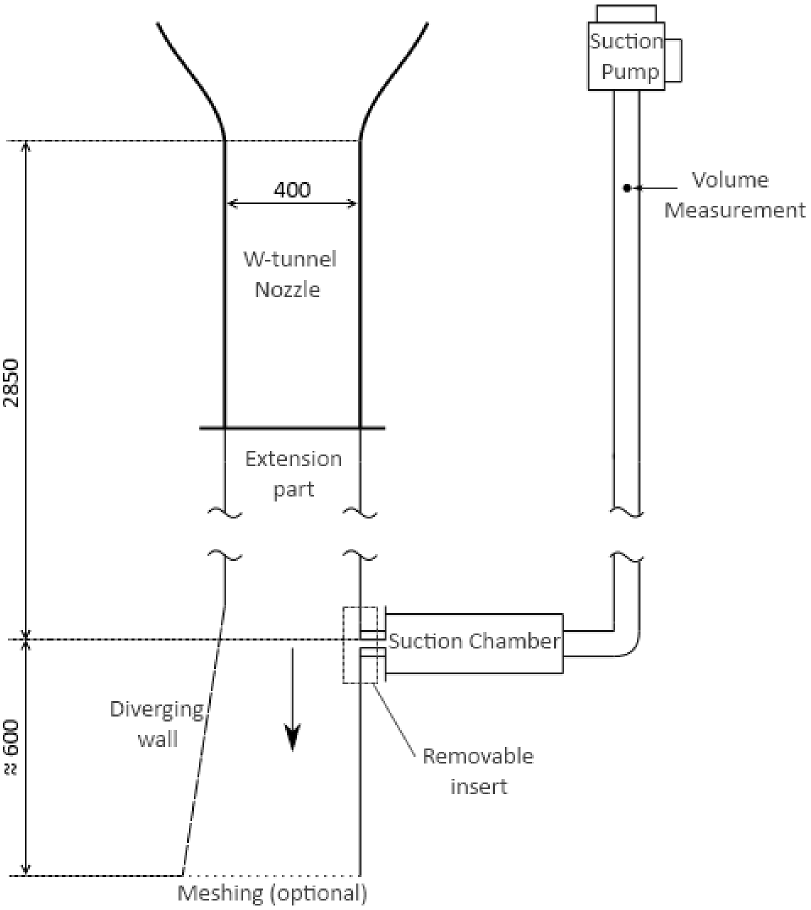

Figure 3.1: Schematic overview of experimental setup (top view). Dimensions in [mm].

the length of the channel was approximately 2.85 [m], which corresponds to a dimensionless development length of, $\frac{l}{D_h} = 7.125$.

The top part of the channel was covered with Plexiglas in order to ensure optical access needed for the use of PIV. Section 3.4 elaborates on the parts of the setup related to the use of this measurement technique. Furthermore twelve wall pressure taps were located near the slot in order to measure the local pressure distribution. Also a pitot tube was positioned in the freestream, well in front of the slot, in order to have direct feedback on the freestream dynamic pressure. Section 3.5 describes the setup related to these pressure measurements in more detail.

During the design of the experimental setup, it was assumed that a turbulent boundary layer would start directly at the end of the wind tunnel contraction. To ensure that this was indeed the case, a trip wire was mounted at the end of the contraction. According to White [45] a flat plate laminar boundary layer can be tripped by using a two-dimensional cylindrical roughness element. Such a trip wire should have a minimum height so that the Reynolds number based on this height and the freestream velocity equals $\mathrm{Re}_{tr} \approx 850$. For a freestream velocity of approximately 30 [m/s], the trip wire should have a minimum thickness of 0.4 [mm] to induce transition. For the current experiment a trip wire with a 1 [mm] diameter was used.

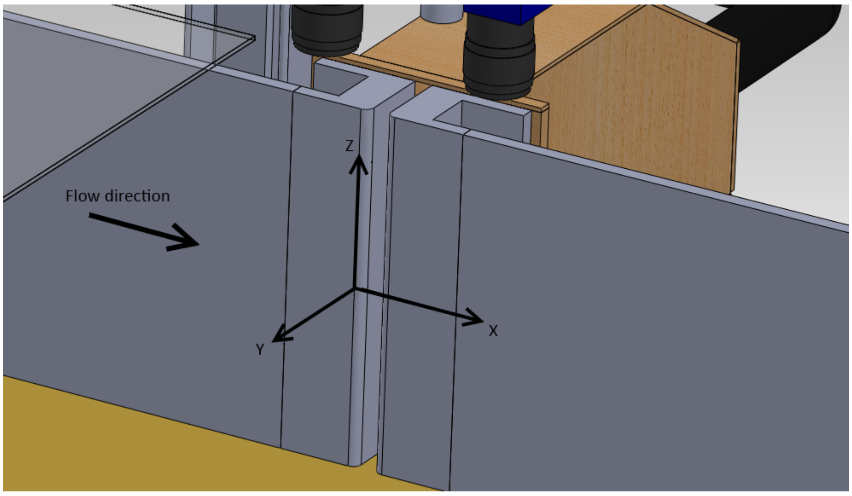

Figure 3.2: Coordinate system used during the description of the experiment and the presentation of the results.

Coordinate system Knowing which general experimental setup was used, it is now important to define a coordinate system. In the remainder of this report, the Cartesian coordinate system depicted in figure 3.2 is used. As can be observed from the figure, the x-axis, y-axis and z-axis correspond to the streamwise, wall-normal and spanwise directions respectively. The origin is positioned at the wall, in the mid-span position of the tunnel. The streamwise location of the origin is at the front edge of the slot, where the suction region starts.

3.2 General Measurement Procedure

During the research project, two measurement campaigns were carried out. Both are briefly described in section 3.2.1. Furthermore the general measurement procedure is explained in section 3.2.2.

3.2.1 Measurement Campaigns

As mentioned earlier in this chapter, both measurement campaigns were carried out in the W-tunnel at the DUT. The first measurement campaign, in the end, has turned out to be a 'learning campaign'. During this measurement campaign a lot of experience was gained on the flow features, the sources of error and the use of PIV.

Before starting with the main PIV measurements, hotwire measurements were performed to assess the two-dimensionality of the flow. The boundary layer velocity profile was measured at different spanwise positions and the spanwise variation was evaluated. Based on these measurements it was also easier to select a proper domain for the PIV measurements as the boundary layer dimensions were already known. Section 3.6 briefly describes the experimental setup related to these measurements.

During the main measurements of this first campaign, the effects of three variables were considered. The dimensionless slot width, $\frac{W}{\delta_0}$, was varied, where δ_0 is the boundary layer thickness at $x = 0$ without the presence of suction. The streamwise pressure gradient and the suction coefficient were also varied.

Quite a 'brute force' strategy was used with respect to the amount of tests for the first campaign. Because the high resolution PIV images did not allow for quick evaluation of the results, a very large test matrix was used, testing combinations of the aforementioned variables. Please refer to appendix A for the entire test matrix of the first campaign. Table 3.1 summarises which variables where considered during the first and second measurement campaign.

Parameter	First campaign	Second campaign
$\frac{W}{\delta_0}$ [-]	0.05, 0.2, 0.5	0.2
$\frac{dp}{dx}$ [Pa/m]	0, 100, 200	0, 200
σ [-]	0.2, 0.4, 0.7, 1.0	0.2, 0.4, 0.7, 1.0

Table 3.1: Different values of the parameters considered during both measurement campaigns.

Unfortunately, during evaluation of the results of the first measurement campaign, it was found that these were relatively inaccurate and, mostly, only suitable for a qualitative evaluation. One of the main problems concerned vignetting of the images. The main cause for this was probably the combined use of a wide-angle lens (35 [mm]) and a Scheimpflug adapter to connect the lens to the camera. However at the particular moment of the first campaign, there was no option to use other lenses.

Based on the experience gained during the first campaign, improvements on the test procedure and the experimental setup were made. These included the use of other lenses, practical improvements with respect to the setup in order to reduce possible vibrations and a smaller test matrix. The latter allowed the author to put more effort into improving the setup and check on the quality of the results during the time frame available in the wind tunnel.

During this second experimental campaign, the main emphasis was on generating high quality data for fewer cases. Despite the flaws and camera issues during the first campaign, its results were considered good enough to assess the influence of slot width. Therefore this parameter was fixed at $\frac{W}{\delta_0} = 0.2$ during the second campaign. Tests were carried out for slot suction at a zero and an adverse pressure gradient (see table 3.1). Furthermore, for this adverse pressure gradient, tests were carried out not only for suction through a slot, but also for suction through a porous plastic and a perforated plate (see 3.3.2). The test matrix for the second measurement campaign can also be found in appendix A.

Note that the descriptions and results in the remainder of this report are all based on the second measurement campaign, unless stated otherwise.

3.2.2 Measurement Procedure

This section briefly describes the general measurement procedure followed during the PIV measurements.

During all tests, the freestream velocity was controlled, based on the dynamic pressure in the freestream, measured using a pitot tube (see section 3.5). In order to account for the varying density, during each measurement, the temperature and atmospheric pressure were measured and the desired dynamic pressure in the freestream was calculated. All these values were written down in a measurement log. It was decided, for each of the PIV measurements, to keep the freestream velocity, in the non-diverged part of the channel, constant at 28 [m/s].

Before starting the measurements with boundary layer suction, for each wind tunnel setting (i.e. type of insert and/or diffuser angle) a reference measurement without suction was performed. From these reference measurements, the value of θ_0 was obtained, which was needed to be able to determine the suction volume for a particular suction coefficient, σ (see equation 2.21). Furthermore the boundary layer thickness δ_0 was also obtained so that the width of the slot could be set to match the desired dimensionless value of $\frac{W}{\delta_0} = 0.2$.

After the reference measurement, the slot was set to the correct width and measurements were performed for the boundary layer with suction. The amount of suction was controlled by regulating the power input of the suction pump. The suction velocity was deduced from the volume measurement as described in section 3.3.4.

For the measurements with an adverse pressure gradient, only one slot on the diffuser wall was opened and a fine meshing was mounted at the end of the tunnel to create the desired positive pressure within the tunnel. Visual inspection by means of tufts was used in order to confirm that the flow remained attached at the diffuser wall.

3.3 Suction System

As mentioned in the introduction of this chapter, the suction system is considered to be the combination of the slot (or porous medium), the suction chamber and everything behind the suction chamber including the pump. This section describes each component of this system in different subsections.

3.3.1 Slot Shape

Contrary to the slot's width, its shape has not been considered as a variable during this experiment. The shape of suction slots has already been investigated quite extensively by Pierpont et al. [30] and Fage et al. [12]. Pierpont et al. found that rounding the edges of a slot results in a reduction of total pressure loss in excess of 30 %. Rounding the edges also slightly improves the external flow. However, given that the slot has rounded edges, the influence of changing the edge radius on the external flow is negligible. Fage et al. present the reader with a set of design curves for an optimal slot shape in terms of slot width, inclination angle and edge radius. These design curves are however dependent on the external flow properties and the suction quantity. Since the experiment described in this report included variations in slot width and suction quantity it is hard to use these design curves for the design of a single slot. Furthermore the use of an inclination angle would complicate the manufacturing of the slot insert beyond feasibility of this experiment.

Based on the findings of Pierpont et al. it was decided to use a single slot shape with rounded edges and no inclination angle. There are two main reasons for using the rounded edges. First of all the large reduction in pressure loss made it possible to achieve higher suction rates with the suction pumps available. Secondly, the improved external flow and reduced pressure loss, give a more representative view on the actual capabilities of slot suction. The latter is especially interesting from an engineering point of view. The actual radius of the edges has been chosen to be 10 [mm]. Using the information from Pierpont et al. this radius is considered to be appropriate for the range of slot widths investigated.

The depth, d, of the slot used is 75 [mm] which results in a depth to width ratio of $2.5 \leq \frac{d}{W} \leq 25$ for the range of slot widths under investigation. According to [20], the pressure loss through an orifice in a wall rapidly increases when the ratio $\frac{d}{W}$ is lower than 2. This is due to the fact that the flow cannot develop properly within the 'channel', causing separation. Increasing the ratio beyond 2 also increases pressure losses due to the increased friction drag. However this increase in pressure loss is much less than the one related to the not fully developed flow. It is assumed that similar effects might occur when using a slot and therefore the slot depth has been chosen such that $\frac{d}{W}$ would not become lower than 2.

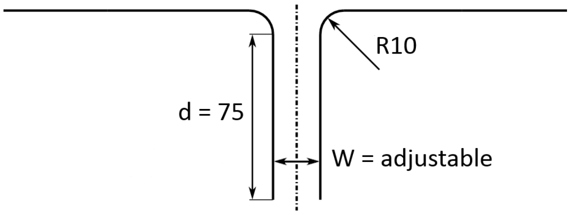

Figure 3.3: Slot geometry used in the experiment. Dimensions in [mm].

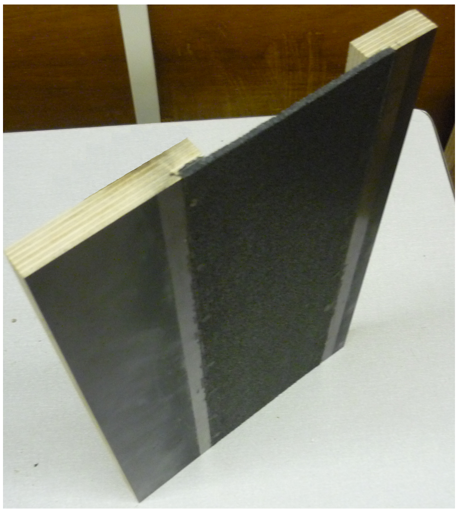

Figure 3.4: Photograph of the used insert, including porous plastic.

Summarising, it was decided to use a single slot geometry, which, for the range of slot widths and suction quantities under investigation, would be as optimal as possible. This resulted in the relatively simple slot geometry as depicted in figure 3.3.

3.3.2 Other Suction Media

In addition to the measurements related to slot suction, similar measurements were performed for boundary layer suction through a porous plastic as well as through a perforated plate. The original insert was adapted in order to fit a 100 [mm] wide region with either the porous plastic or the perforated plate. Figure 3.4 shows the insert used with the porous plastic. The perforated plate was mounted in a similar fashion.

Ideally the suction would be distributed over a large enough width so that the maximum suction velocity remained below ± 1% of the freestream velocity. For such small velocities, the boundary layer approximations in equation 2.6 remain valid [36]. It was calculated that for that purpose, the suction should have been distributed over a range of approximately 300 [mm]. Unfortunately, due to practical limitations, this was not possible.

Figure 3.5 schematically shows how the distributed suction zone (either porous plastic or perforated plate) was positioned related to the original setup including the slot. For convenience, the origin of the coordinate system, as already defined in figure 3.2, is also shown. It can be observed, that for both configurations the suction zone starts at the same location. This is assumed to give the most fair comparison between the two suction mechanisms, as the boundary layer is equally

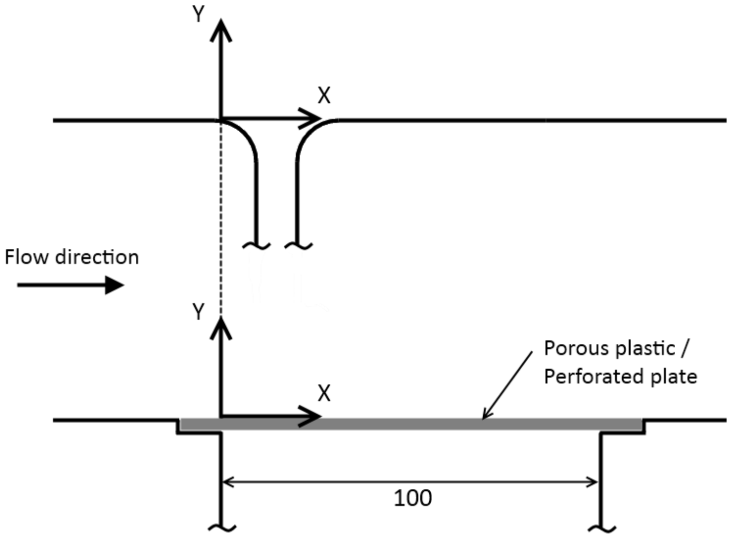

Figure 3.5: Configuration of continuous suction with respect to original configuration with slot. All dimensions in [mm].

developed before the suction is applied. Note that for the porous plastic, part of the suction volume might cross diagonally through the zones where the plastic is mounted to the insert. For the perforated plate, this is not possible. This effect is further considered during the evaluation of the results in section 5.4.

The porous plastic, produced by the company Porex, was 4 [mm] thick and was selected to have a porosity such that the entire range of suction coefficient could be tested with the available suction pump. Furthermore its strength was selected, so that the plastic would not deform due to the pressure differences associated with the higher suction rates. The perforated steel plate had a thickness of 1.5 [mm], and it contained circular perforations with a diameter of 2 [mm]. The perforations were organised in a 60 [deg] staggered pattern with an interspacing of 7.8 [mm] (see figure 3.6). This resulted in an open area ratio of 5.6 %. The porosity characteristics of both materials are demonstrated by the graph in figure 3.7.

3.3.3 Suction Chamber

The suction chamber provides the transition from the slot shape towards the shape of the piping through which the air is guided to the suction pump. While forming this transition, the chamber should have the proper dimension, such that the flow through the slot is two-dimensional. It was assumed that if the suction box would be too small, a peak in suction velocity near the centre of the slot would exist. On the other hand, the suction box could not be too large due to practical limitations. In order to make sure that the flow through the slot was 2-dimensional and to find a suitable geometry for the suction box, some preliminary CFD simulations were performed. These simulations were used to compare different suction chamber geometries and to have an idea of its influence on the 2-dimensionality of the flow through the slot.

From these simulations it was confirmed that if the suction box is too small, the velocity distribution is not completely two dimensional. From a comparison of the different geometries, the one with satisfactory dimensions and velocity distribution was chosen. The geometry that has been

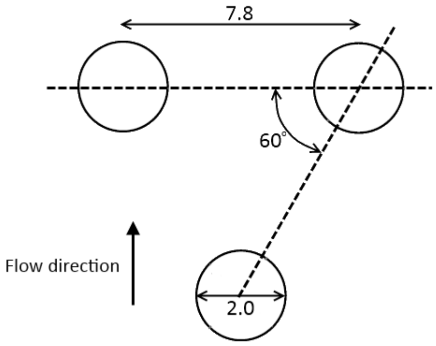

Figure 3.6: Lay-out of hole pattern on the perforated plate. All dimensions in [mm].

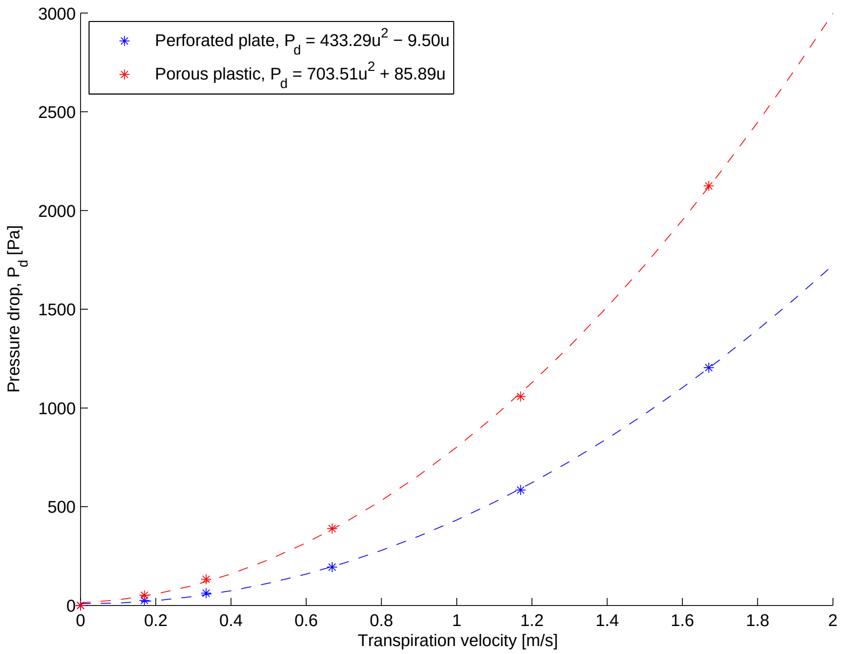

Figure 3.7: Porosity for the porous plastic and the perforated plate.

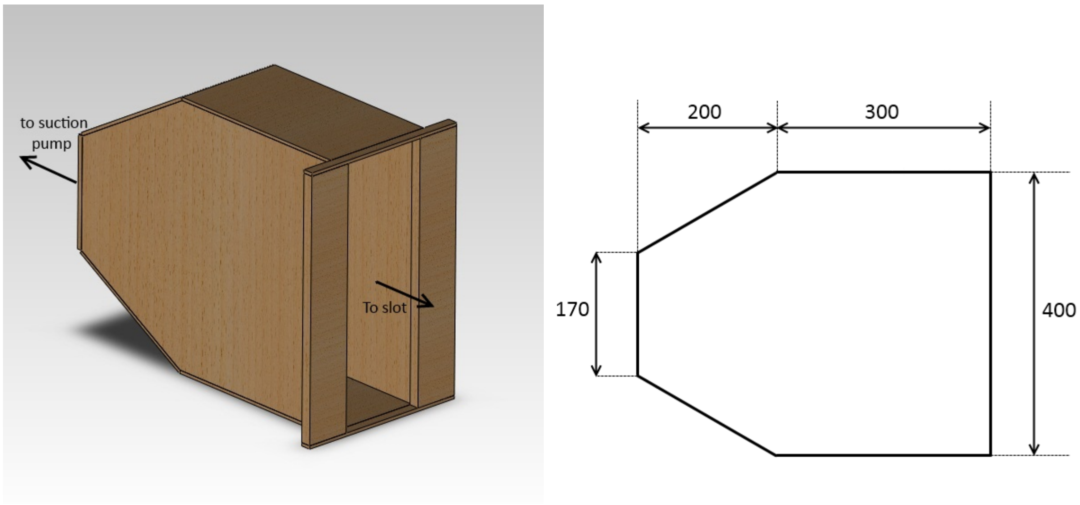

(a) 3D view of the suction box (b) Important dimensions (mm)

Figure 3.8: Suction box geometry used during experiment.

used during the experiment is depicted in figure 3.8. Figure 3.9 shows the velocity distribution along the span of the slot, normalised by the mean velocity. It was found that, apart from very close to the edges where a boundary layer develops, the variation of the velocity in the slot remains below 1 % of its mean value.

The slot width used for this simulation corresponds to the largest slot width used during the experiment. This was considered as a worst case scenario with respect to the two dimensionality of the flow across the slot. The largest slot has the lowest pressure drop and consequently gives the most rise to non-two-dimensionality in the slot flow.

In order to obtain these results, simulations were performed using OpenFOAM. The SimpleFoam solver was used, which solves the incompressible Reynolds Averaged Navier-Stokes (RANS) equations using a finite volume discretisation. The turbulence was modelled using the K-ω SST turbulence model in combination with wall functions for the turbulent quantities. Mostly a second order central difference scheme was used for the discretisation of the differential equations. Only the convection schemes of the turbulent quantities were set to upwind because of stability issues encountered during the simulations.

The computational domain as used for these simulations can be observed in figure 3.10. This domain has been drawn and discretised using a commercial software package, ANSA. The mesh consisted of a combination of prism layers growing from the walls and tetrahedral elements which covered the rest of the domain. On the inlet plane a uniform velocity was imposed such that the resulting volume flow corresponded to approximately 1.5 times the maximum volume flow encountered during the actual experiment. The outlet and wall boundary conditions were set such that the no-slip condition was satisfied at the walls and that the pressure was fixed at the outlet. Table 3.2 summarises the boundary conditions used during the simulation.

Patch	Velocity $\bar{U}$ [m/s]	Pressure p [Pa]	Turbulent quantities
Inlet	fixedValue (-0.4783 0 0)	zeroGradient	outletInlet
Outlet	zeroGradient	fixedValue, 0	zeroGradient
Wall	fixedValue (0 0 0)	zeroGradient	Wall function

Table 3.2: Boundary conditions used for each patch during CFD simulation.

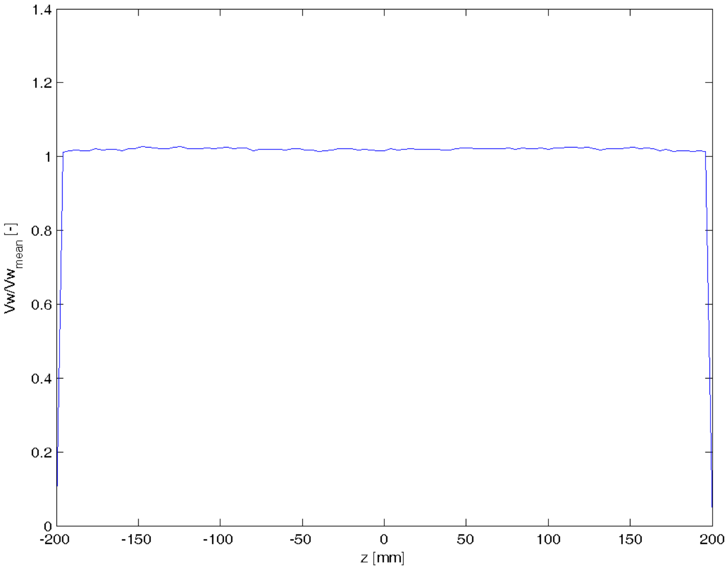

Figure 3.9: Velocity distribution along the span of the slot, obtained from CFD simulations.

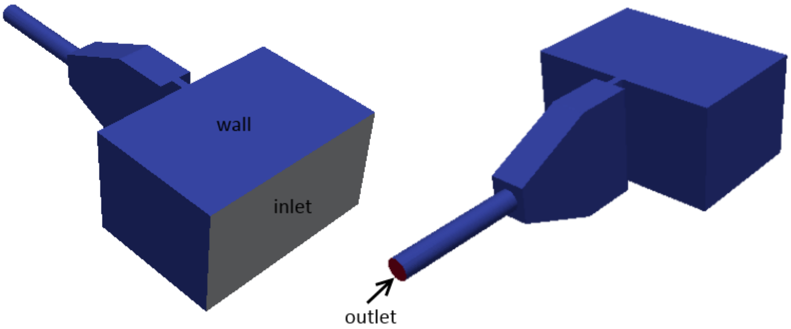

Figure 3.10: Computational domain used for simulation of suction box.

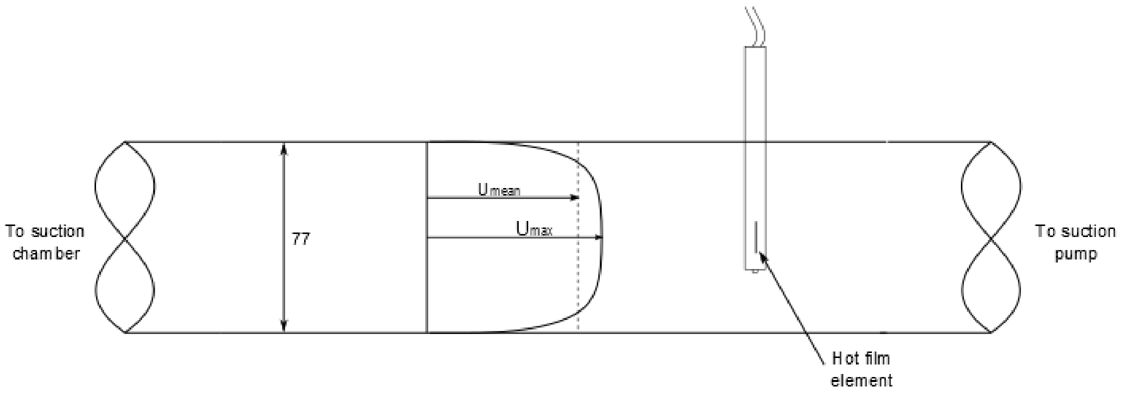

Figure 3.11: Measurement of the maximum velocity within a pipe, by using hot film element. Dimensions in [mm].

3.3.4 Volume Measurement

In order to determine the suction coefficient, σ, one needs to know the suction velocity within the slot (see equation 2.21). During the current experiment this suction velocity is not measured directly but deduced from a volume measurement of the flow through the slot. This is mainly because there is no feasible way to determine the slot velocity with direct feedback. Note that an important assumption on which this deduction is based is that the suction velocity is uniformly distributed over the span of the slot.

For the experiment, different volume measurement techniques were considered. Ideally the volume rate is measured with a high level of accuracy without introducing significant pressure losses. These pressure losses are to be avoided as this might compromise the suction rate achievable by the pumps available. However this is not easy to achieve, especially at the high volume rates considered during the current experiment (up to 4000 [litres/min]). High accuracy flow meters available at the experimental facility could not be used due to their limited range of flow rates (up to 300 [litres/min]). These are based on the positive displacement principle in which the volume is measured in discrete amounts of air. Also ‘pressure based’ methods were considered, including the venturi tube and the orifice plate. However, the manufacturing and calibration of a venturi tube requires quite some expertise. Furthermore an orifice plate induces undesirably high pressure losses. Therefore both of these methods were considered to be inappropriate for the current experiment.

In the end, a method has been used in which the maximum velocity is measured within the pipe connecting the suction chamber to the pump. The relation between this maximum velocity and the velocity profile could be used to determine the average velocity through the pipe and thus the volume flow as described in appendix B. This method is easy to implement, introduces reasonably low pressure losses and has an acceptable accuracy.

For the volume measurement a PVC pipe with a length of 3.5 [m] and a diameter of 77 [mm] has been used. The position at which the measurements were performed was located approximately 3.3 [m] away from the entrance of the pipe. This was done in order to make sure that the velocity profile within the pipe was fully developed and that the entrance effects were negligible [44]. For the current measurement position and pipe diameter, it was confirmed, using equation B.1, that the velocity profile indeed was fully developed for the entire range of suction velocities used. The relations in Appendix B were used together with the roughness height for common PIV pipe, $\epsilon = 0.0015$ [mm], to find the relation between the maximum velocity inside the pipe and the mass flow.

Laser	Power [Mj]	Wavelength [nm]	Repetition rate [Hz]
Quantel Evergreen	200	532	15
Quantel Twins BSL	200	532	15

Table 3.3: Lasers used during experiments.

In order to measure the maximum velocity, a hotfilm element embedded within a cylindrical sensor (EE75 Velocity/Temperature Transmitter) was used. Although this element induces some errors due to its intrusiveness and the limited spatial resolution, it is preferred over the use of a pitot tube. The hotfilm element is very easy to operate and is capable of measuring the velocity accurately at both low and high velocities. Figure 3.11 schematically shows the measurement principle.

In order to assess the validity of this measurement method a series of tests has been performed prior to the actual wind tunnel experiment. These tests included the comparison of the maximum measured velocity by both a pitot tube and the hotfilm element. Furthermore it was confirmed that the velocity profile was fully developed at the measurement position. The test procedure and the corresponding results can also be found in appendix B.

3.4 Particle Image Velocimetry Measurements

This section describes the part of the experimental setup related to the PIV measurements.

During both measurement campaigns two different types of lasers were used. Apart from availability there was no specific reason for using two different lasers during the experiment. Both Nd:YAG lasers are comparable as can be seen from table 3.3.

The light sheet for the experiment was formed by a combination of one spherical(-150) and two cylindrical(200/90) lenses and a mirror. In order for the laser not to cause any blockage effects it was positioned outside the flow and a mirror was used to bend the light sheet towards the right direction. The height of the laser sheet, and thus the measurement plane, was set at $z = 0.9$ [cm]. The position of the laser and the resulting laser sheet are schematically depicted in figure 3.12.

To obtain the images, two 16 megapixel cameras were used (see table 3.4) and positioned next to each other to obtain an extra wide field of view. The cameras were positioned above the tunnel which was covered with Plexiglas plates in order to ensure optical access. Figure 3.13 shows the positioning of the cameras. The cameras were positioned such that an overlap region existed between the two obtained images. This was needed to be able to stitch the obtained images/vector fields nicely. The total field of view obtained after cropping the images in the wall-normal direction and including the overlap region was 590 x 150 [mm^2].

Two AF Micro-Nikkor 50mm f/2.8D lenses were mounted on the cameras which were set to an f-stop of 4 in order to have proper brightness in the images. Due to the relatively large field of view, the intensity of the resulting laser sheet was somewhat low, for which was compensated by the larger aperture. The f-stop, therefore, was below the calculated optimal, causing the imaged particle diameter to be below the size of one pixel. To prevent the peak-locking effect

Lavision Imager Pro LX16	
Resolution [pix.]	4870 x 3246
Frame Rate [Hz]	5
Pixel Size [μm]	7.4 x 7.4
Min. Time Interval [ns]	600

Table 3.4: Specifications of the cameras used during the experiment.

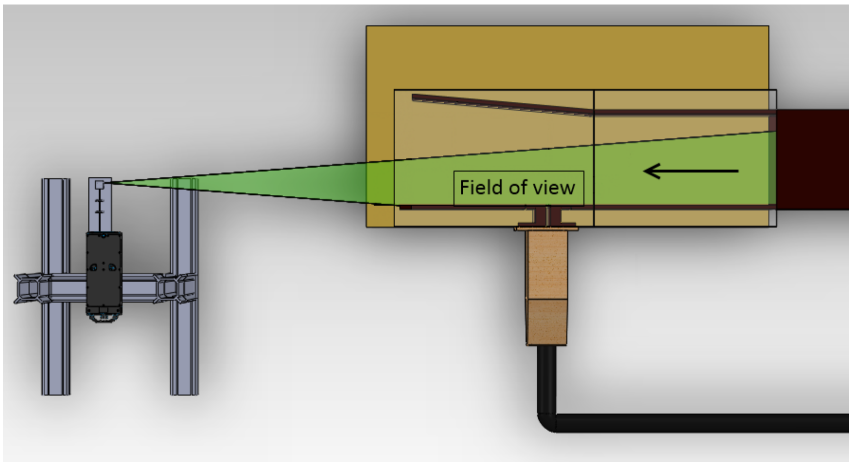

Figure 3.12: Schematic overview of the laser setup during the experiment (top view).

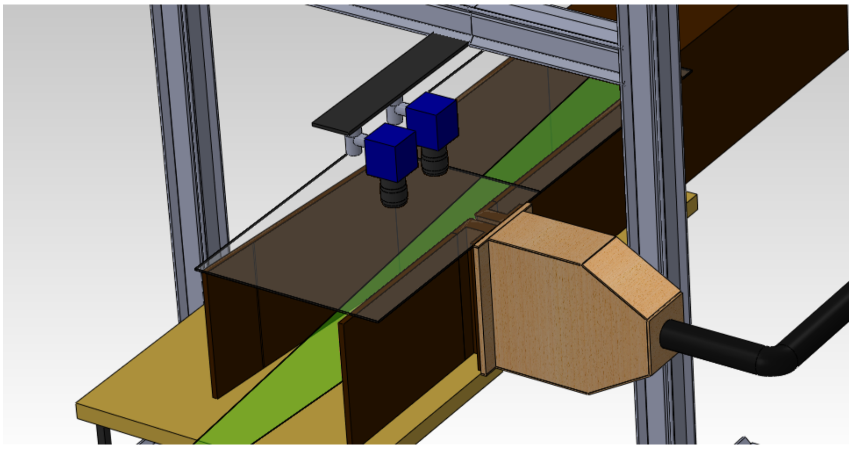

Figure 3.13: Positioning of cameras relative to the experimental setup.

PIV Setting	Value
Combined Field of View [mm^2]	590 x 150
Magnification [-]	0.111
Focal length [mm]	50
F-stop [-]	4
Pulse separation [μs]	35
Sample size [-]	500

Table 3.5: PIV settings used during the experiment.

from occurring (see section 2.3) the lenses were slightly defocussed. This caused the particles to cover approximately two to three pixels again. Table 3.5 summarises the PIV settings used for the experiment. In section 4.1 further settings regarding the PIV post-processing are discussed.

3.5 Pressure Measurements

In addition to the PIV measurements, pressure measurements have been performed. In order to see the influence of suction on the pressure distribution, pressure taps, with a 0.4 [mm] diameter, have been positioned symmetrically in front of and behind the slot. These were displaced in the spanwise direction, at z = 50 [mm], in order to make sure that they were non-intrusive to the PIV measurements. The pressure taps were connected to a Scanivalve DSA3217 pressure scanner of which the data was digitally recorded. Figure 3.14 schematically shows the position of the pressure taps relative to the slot.

To measure the freestream velocity, a pitot tube was positioned in the freestream at approximately x = -300 [mm], y = 250 [mm] and z = 0 [mm]. This tube was also connected to the Scanivalve scanner, and its direct feedback allowed to regulate the freestream velocity.

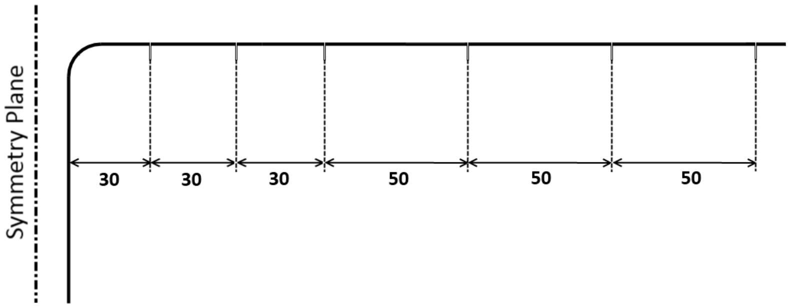

Figure 3.14: Location of the pressure taps with respect to the slot. Cross-section at z = 50 [mm], pressure taps symmetrically distributed around slot.

3.6 Hotwire Measurements

Earlier it was already described that hotwire measurements were performed to assess the two-dimensionality of the flow, prior to the main experiment. In order to do so, boundary layer traverses were made, at different spanwise positions, using a hotwire probe. The hotwire probe was mounted on a traversing system which was positioned at the exit of the tunnel. The hotwire element was inserted into the flow through the nozzle exit as can be observed from figure 3.15. The measurements were obtained at $x = 400$ [mm].

The hotwire probe was connected to an IFA-300, Constant Temperature Anemometer (CTA) from TSI. This anemometer was, in turn, connected to a computer with the ThermalPro and LabVIEW software packages installed. Using these software packages, the hotwire was calibrated based on the velocity measured from a pitot tube.

(a) General setup

(b) Traversing system

Figure 3.15: Photograph of experimental setup for hotwire measurements.

Chapter 4

Data Processing

This chapter discusses the data processing procedures performed to convert the raw PIV images to the results presented in chapter 5. Firstly the PIV post-processing, to obtain the velocity data, is discussed. Secondly the calculation of the integral parameters θ and δ^* is explained. Thirdly the Savitzky-Golay smoothing filter used during the presentation of the results is briefly discussed. Finally, the procedure to obtain the pressure field from the velocity data, obtained through PIV, is discussed.

4.1 PIV Post-processing

To obtain the instantaneous and mean velocity vector fields from the raw image pairs, the software package DaVis from Lavision was used. This program offers the user a great variety of post-processing tools and settings. While the selection of some of these settings is quite straightforward, others need to be varied, depending on the experimental setup and the flow problem in order to have the best quality of results. Therefore, before processing the datasets of all test cases, different PIV post-processing procedures were compared.

The final post-processing procedure used, is described by the following steps:

1. Calculate and subtract the ‘minimum’ of the data set from each of the raw images.

The software package forms an image of which each pixel represents the minimum value found for that particular pixel in all the raw images contained by the dataset. By subtracting this image from each of the raw images, steady reflections are removed. This is especially useful for the reflection of the laser light on the wall. Figure 4.1 shows the effect of subtracting the minimum for reducing this reflection on the wall.

2. Define and mask out the irrelevant part of the image

As can be observed from the raw images, a part of the wall, which should not be included for the cross-correlation procedure, is still visible. Therefore a mask is applied in order to ensure that this part is not used for the cross-correlation. Figure 4.2 shows the masked out part of the image.

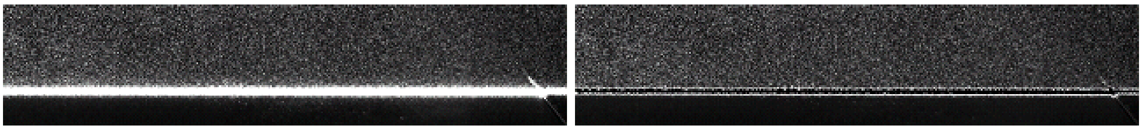

(a) Raw image (b) Minimum subtracted

Figure 4.1: Effect of subtracting the minimum from the raw image for the near-wall region.

Figure 4.2: Application of mask to the near-wall part.

3. Perform the cross-correlation of image pairs to obtain a set of instantaneous vector fields.

The settings eventually used to obtain the instantaneous vector fields are summarised in table 4.1.

Most of these settings were chosen after consulting more experienced users of the DaVis software package. However, the effect of interrogation window size was investigated by performing multiple different processing sequences for the same image. Based on this comparison the final settings related to the window size as presented in table 4.1 has been used.

In order to save computational resources the comparison has been performed for a small part of the image. This was considered to be enough to see the influence of the change in interrogation window size. The window size, overlap and aspect ratio were varied which resulted in a number of different velocity profiles. In general the differences between the obtained velocity profiles were very small. As expected, decreasing the window size and increasing the overlap both results in a higher vector density.

In the end it was found that using 75 % overlap with a window size of 16x16 pixels resulted in a profile for which the lowest measured velocity approximately equals $\frac{u}{U_e} \approx 0.3$. Using either smaller overlap ratios or larger window sizes increased this value towards $\frac{u}{Ue} \approx 0.5$. Figure 4.3 also shows that for the 16x16 75 % overlap windows, the shape of the profile remains smooth near the wall. Similarly, it was found that stretching the interrogation windows to have a 1:4 overlap gave slightly better results. Therefore it has been decided to use these specific settings in order to post-process all other datasets. The resulting spatial resolution in terms of vector pitch was 0.267

Option	Setting used
Type of Correlation	Standard (using FFT)
Single vs Multi Pass	Multi Pass
Interrogation Window Size (Aspect Ratio)	
First Pass:	32x32 (2:1)
Second and Third Pass:	16x16 (4:1)
Median Filter	Strongly Remove and Iteratively Replace
Remove if diff. to avg >	2 · RMS of neighbours
(Re)insert if diff. to avg <	3 · RMS of neighbours
Vector Postprocessing	Remove groups with fewer than 10 vectors

Table 4.1: Post-processing settings to obtain instantaneous vector fields.

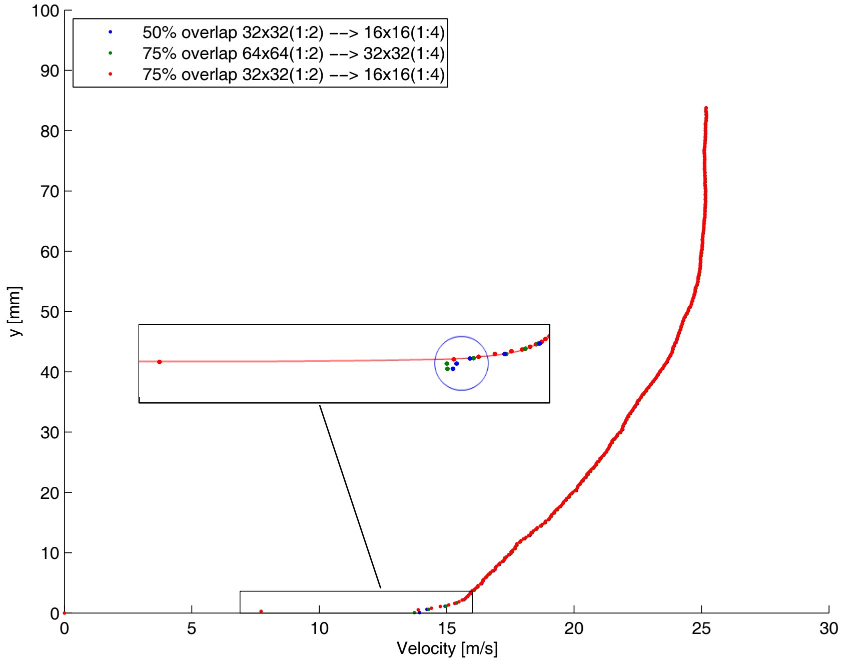

Figure 4.3: Effect of different interrogation windows for the near-wall points in the velocity profile.

[mm] in both x- and y-direction.

For further explanation on, for example, the correlation procedure, using the Fast Fourier Transform or the median filter, the reader is referred to [32].

4: Obtain the mean vector field and Root Mean Square (RMS) fluctuations with respect to this mean.

To improve accuracy, the instantaneous velocity fields were processed iteratively to obtain the final mean and RMS velocity fields. By doing so, it was ensured that all source vectors for a mean vector, were inside the range of $\pm\, 2 \cdot$ RMS.

4.2 Determination of Integral Parameters

This section describes the procedure used to determine the integral parameters, θ and δ^*. During this procedure some assumptions are made of which the validity will be shown.

In order to calculate θ and δ^*, a numerical integration has to be performed for the discrete data points obtained from the PIV measurements. In this report a trapezoidal rule has been used for this purpose [38]. This rule estimates the integral by assuming the function to be linear between each of the data points. Since, for the upper part of the velocity profile, the density of data points is very high, the integration error is assumed to be negligibly small. The part near the wall, where the velocity gradient increases, will be discussed later on.

4.2.1 Determination of Freestream Velocity

The first step in the determination of the integral parameters is the determination of the boundary layer edge velocity, U_e. After all, the velocity profile needs to be non-dimensionalised by this freestream velocity in order to calculate θ and δ^* (see equations 2.1 and 2.2).

Theoretically, when the velocity profile has reached its maximum (i.e. $u = U_e$), the velocity remains constant when moving further away from the wall. During evaluation of the results it was found that this was not always the case. Minor variations or a slight drift in freestream velocity were found to be present sometimes, thereby causing a discrepancy between the measured velocity at the edge of the boundary layer and at the top of the measurement domain (see section 5.2.1). In order to avoid this discrepancy to cause an additional error within the results, an algorithm was used to determine the approximate 'edge' of the boundary layer.

This algorithm calculated the velocity gradient, $\frac{\partial u}{\partial y}$, for each position normal to the wall, y. To do so, an average was taken over the range of twenty points above the particular wall-normal coordinate. When the calculated gradient reached a value below a given threshold, the 'edge' of the boundary layer was set to that coordinate, y_e. The freestream velocity was determined by averaging the value of thirty data points above this edge coordinate. Figure 4.4 illustrates the determination of the edge velocity. The threshold value, $\left(\frac{\partial u}{\partial y}\right)_t$ was determined from the condition:

$$\left|\frac{y_e}{U_e}\frac{\partial u}{\partial y}\right| \lesssim 0.025 \tag{4.1}$$

As y_e and U_e were not known a priori, these were respectively estimated by the freestream velocity at the top of the domain and the boundary layer thickness corresponding to that position, where the velocity profile reached 99 % of the estimated freestream velocity. It was found that iteration did not significantly change the result for the edge coordinate. That is, the maximum shift in edge coordinate due to iteration was found to be 1 to 2 data points.

From figure 4.4, one can also observe that indeed an error would be made when, for example, a slight drift in velocity is present and the edge velocity was determined at the top of the domain. More disturbingly, this error would also be dependent on the size of the boundary layer, since a drift can possibly cause a larger error in measured freestream velocity for smaller boundary layers. As this type of error is prevented due to the used algorithm, the author believes that this method is a fair way of determining the freestream velocity. Finally it should be noted that the edge coordinate, y_e is also used as the upper boundary of the integrals to determine θ and δ^*.

4.2.2 Near-Wall Data Points

Before being able to apply the trapezoidal integration rule, the raw velocity profile had to be adjusted for the near-wall region. The points with a velocity lower than $u \leq 0.2 \cdot U_e$ were set to zero. This was done since for some velocity profiles, a few points with a very low velocity (i.e. $\frac{u}{U_e} \leq 0.05$) occurred which were observed to be erroneous. That is, visual inspection showed that these points could not represent physical data.

For each velocity profile the first data point for which the velocity was above $\frac{u}{U_e} = 0.2$ was found and set to be at a height of $1.5 \cdot \Delta y$. Here, Δy is the uniform spacing between the data points in wall-normal direction. It was found that this gave acceptable results when compared with theoretical data from Spalding's law of the wall [45]. To illustrate this, figure 4.5 shows an example of the lower part of a measured velocity profile for the case without suction, together with Spalding's law of the wall.

From figure 4.5 it can be observed that as the wall is approached, the measured data points tend to deviate more from Spalding's law of the wall. This could be observed for both the

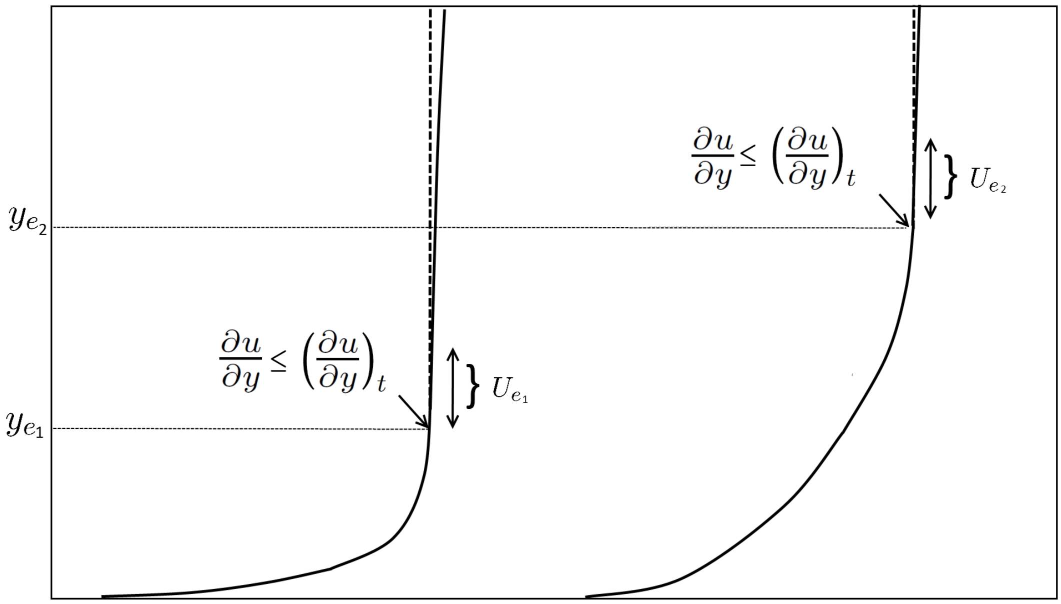

Figure 4.4: Illustration of procedure to determine the freestream velocity at the edge of the boundary layer, U_e

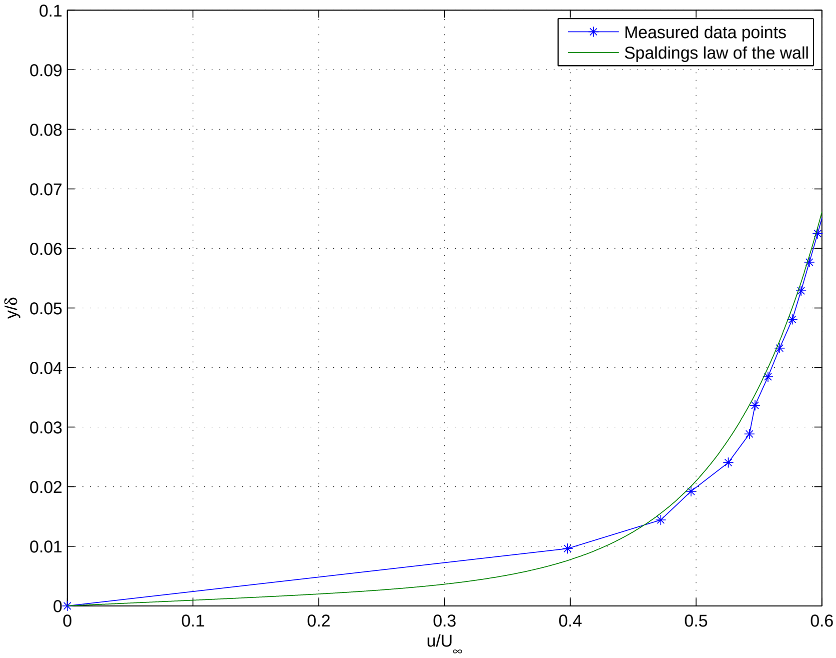

Figure 4.5: Example of measured velocity profile data vs. Spalding's law of the wall for near-wall region. Data from adverse pressure gradient case without suction.

zero pressure gradient case and the adverse pressure gradient case without suction at different streamwise positions. This can be explained by the fact that the accuracy of the PIV measurements decreases when approaching the wall [18]. The reflections from the laser at the wall play an important role in this. Furthermore, the velocity gradient is very high near the wall which is also a source of error for the PIV results (as explained in section 2.3.3).

Apart from the deviation of the data points, one can also observe that, when approaching the wall, the linear assumption made in the trapezoidal rule becomes less valid. It can be seen that due to the linear approximation, in this case, the apparent velocity profile based on the discrete data points in figure 4.5 is 'less full' than the one described by Spalding's law of the wall. Inspection of multiple profiles showed that both over- and under prediction of the integral values occurred due to the above combination of errors.

For both the zero pressure gradient and the adverse pressure gradient, the lower part of the velocity profile has been compared with Spalding's law of the wall for 100 spanwise positions. Based on this comparison for, in total, 200 velocity profiles, an RMS error was found of approximately 0.04 [mm] and 0.01 [mm] for δ^* and θ respectively. For the lowest values of δ^* and θ, this corresponds to a percentual error of 0.5 % and 0.2 % respectively.

Note that to be able to use Spalding's law of the wall, the shear velocity and thus the friction coefficient need to be known. To find the friction coefficient, the Clauser technique has been used as described in section 2.1.4.

4.3 Smoothing of the Results

During the presentation of the results, smoothing is frequently applied in order to improve the readability of the graphs. Specifically for the presentation of the streamwise development of the boundary layer parameters this was needed to filter out the high spatial frequency fluctuations (measurement noise). This section will describe the smoothing methods used and their effect on the presented results.

To filter out the high frequency variations in the raw results, two smoothing procedures were considered. The first procedure relied on averaging the velocity data over a particular amount of points in spanwise direction. The averaged velocity profile was then used to calculate the boundary layer parameters, thereby giving a smoother result with a decreased resolution in spanwise direction. The second way of smoothing considered was applying the Savitzky-Golay (Sgolay) smoothing filter to the 'noisy' data [34]. This method relies on the local application of a polynomial regression to determine the smoothened result of each point. The degree, k and the span (minimum of k+1) can be selected by the user to give the desired results. As compared to a conventional moving average filter, this filter has the advantage of being able to preserve local minima and maxima instead of flattening them.

Figure 4.6 shows an example of the effect of both filters on the momentum thickness for the adverse pressure gradient case with suction. Both filters use a span of 100 data points and the Savitzky-Golay filter uses a second degree polynomial regression.

It can clearly be seen that for these settings the data points of both filters nicely coincide with the original data. However, the peak value near the location of suction ($x = 0$ [mm]) could be missed when using the velocity smoothing method. This could be avoided by using a lower span for averaging, near the slot. Instead, during the remainder of the report mostly the Sgolay filter has been used for smoothing, due to its ease of use. If smoothing is applied, it is stated in the caption of the figure. For example, a first order Sgolay filter with a span of 200 points is denoted as Sgolay(1,200).

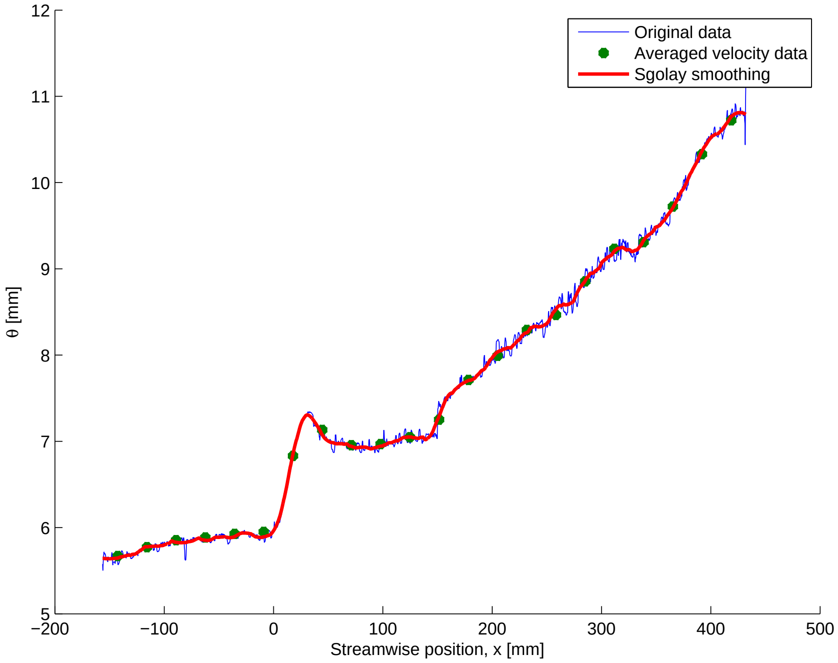

Figure 4.6: Effect of smoothing filters on the APG result with suction for the momentum thickness. Span = 100 and degree = 2 (Sgolay).

4.4 Image Stitching

As reported in section 3.4, two cameras have been used in order to obtain an extra wide field of view. The two image sets were post processed separately using DaVis and the resulting vector fields were stitched afterwards using Matlab. During the setup and calibration of the cameras it was ensured that an overlap region was present. Within this overlap region the vector fields of both images were averaged to create one large vector field. This averaging was done according to the linear function schematically depicted in figure 4.7.

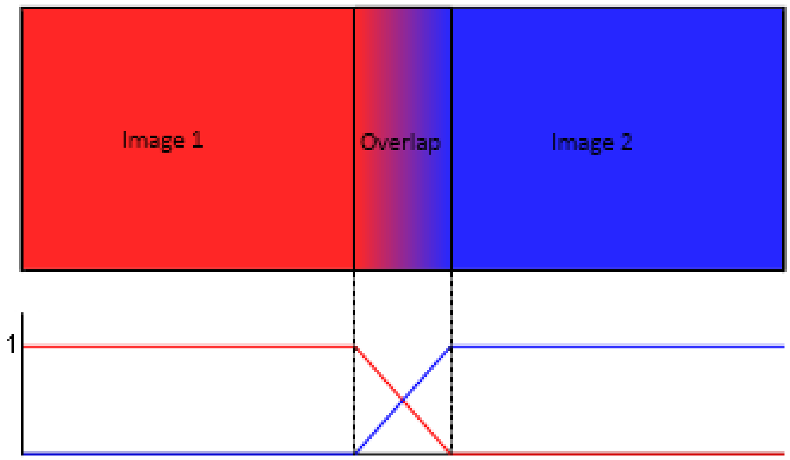

Figure 4.7: Schematic representation of stitching of the two separate vector fields.

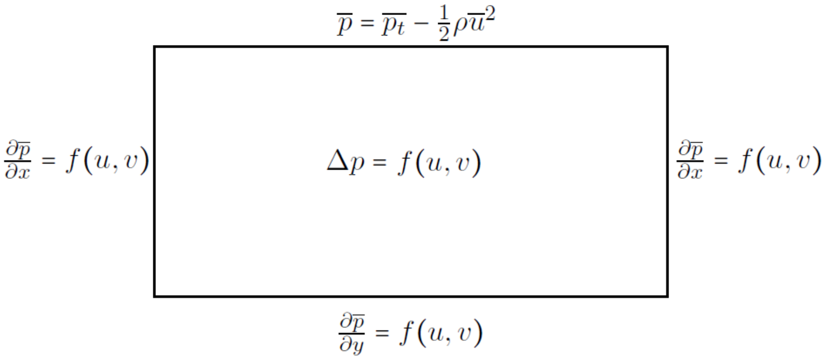

Figure 4.8: Boundary conditions used for solving the Poisson equation for the pressure.

4.5 Obtaining Pressure from PIV

In order to obtain the pressure field from the PIV velocity data, the Poisson equation for the mean pressure was solved numerically [16]. For a two-dimensional turbulent flow, the mean pressure is given by equation 4.2. For the derivation of this equation, please refer to appendix C.

$$\Delta\overline{p} = 2\rho\left(\frac{\partial\overline{u}}{\partial x}\frac{\partial\overline{v}}{\partial y} - \frac{\partial\overline{v}}{\partial x}\frac{\partial\overline{u}}{\partial y}\right) - \rho\left(\frac{\partial^2\overline{u'^2}}{\partial x^2} + 2\left(\frac{\partial^2\overline{u'v'}}{\partial x\partial y}\right) + \frac{\partial^2\overline{v'^2}}{\partial y^2}\right) \tag{4.2}$$

This equation was solved, using a Matlab code[1], in which a finite difference method was applied. In order to be able to solve the equation, the correct boundary conditions were implemented, consisting of three Neumann boundary conditions and one Dirichlet boundary condition to make the 'connection to the real world'.

The Neumann boundary conditions, prescribing the values of $\frac{\partial\overline{p}}{\partial x}$ and $\frac{\partial\overline{p}}{\partial y}$, were simply obtained by rearranging the two dimensional Reynolds averaged momentum equation, resulting in:

$$\frac{\partial\overline{p}}{\partial x} = -\rho\left(u\frac{\partial u}{\partial x} + v\frac{\partial u}{\partial y}\right) + \mu\Delta u - \rho\left(\frac{\partial u'^2}{\partial x} + \frac{\partial u'v'}{\partial y}\right) \tag{4.3a}$$

$$\frac{\partial\overline{p}}{\partial y} = -\rho\left(u\frac{\partial v}{\partial x} + v\frac{\partial v}{\partial y}\right) + \mu\Delta v - \rho\left(\frac{\partial u'v'}{\partial x} + \frac{\partial v'^2}{\partial y}\right) \tag{4.3b}$$

The derivatives on the right hand side of equations 4.2 and 4.3 were obtained by using the 'gradient' function in Matlab. This function computes the gradients in x- and y-direction for a given matrix, using a central differencing scheme.

The Dirichlet boundary condition, prescribing the value of p, was determined using Bernoulli's principle. At the top of the measurement domain, in the freestream, the velocity data from the PIV results was used, together with the calculated value of the density, ρ, to calculate the dynamic pressure. The total pressure in the freestream was obtained from the pitot tube measurements (section 3.5). Figure 4.8 schematically illustrates the implementation of the boundary conditions.

---

[1] Code adapted from D. Ragni

Chapter 5

Results

This chapter presents the reader with the results obtained from the experimental investigation. The results in this report only consider the effects of suction on the mean properties of the turbulent boundary layer. As mentioned in the introductory chapter, the investigation of the turbulence properties is left for further research. The results are discussed and compared with both theory and other references from literature. This chapter is organised as follows:

The first section shows the results from preparatory measurements, while the second section discusses the results for suction of the turbulent boundary layer at a zero pressure gradient. The third section presents the results for slot suction of the boundary layer experiencing an adverse pressure gradient which are compared with the zero pressure gradient case.

For the adverse pressure gradient case, distributed suction was also applied through a porous plastic and a perforated plate. The results of these tests are presented in section four, together with a comparison between distributed suction and localised (slot) suction. Turning back to the problem of slot suction, section five briefly discusses the effect of the width of the slot for a given suction rate. Finally, section six ends this chapter with a discussion on the uncertainty of the presented results.

5.1 Results from Preparatory Experiments

Before diving into the results of the main experiment, this section presents results from preparative measurements, carried out before the main PIV measurements. It discusses the two-dimensionality of the main flow field without suction and the two-dimensionality of the suction velocity. Furthermore it shows how the sample size for the PIV measurements was determined.

5.1.1 Two-Dimensionality of the Main Flow

It is important to confirm the two-dimensionality of the flow field, as this is one of the main assumptions on which the interpretation of the results is based on. Furthermore, it is important to avoid three-dimensional effects, like separation, because these influence the quality of the measurements in a negative sense. Finally, the method to determine the suction quantity, as described in section 3.3.4, also relies on the assumption of two-dimensional flow.

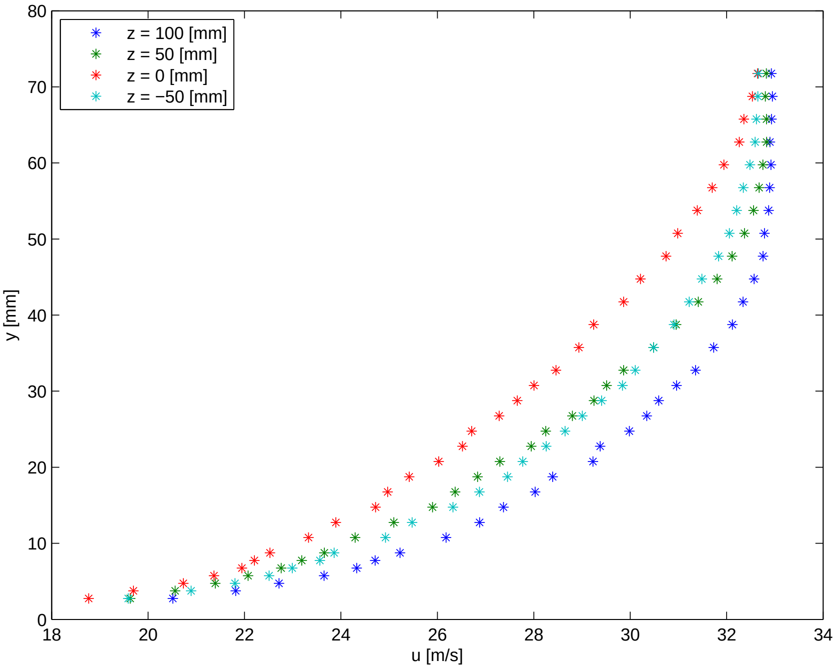

Figure 5.1: Velocity profiles at different spanwise positions, for the zero pressure gradient case without suction (obtained at $x = 400$ [mm]).

In order to assess the two-dimensionality of the flow along the measurement wall, hotwire measurements were performed, prior to the main PIV measurements. At different spanwise locations, boundary layer profiles were measured. These measurements were performed at $x \approx 400$ [mm].

Figure 5.1 shows the different velocity profiles obtained at this streamwise location. One can immediately observe that the velocity profiles vary, depending on the spanwise location. It can be seen that there is a slight variation in freestream velocity along the span. This variation is considered to be a wind tunnel characteristic. However, the normalised velocity profiles in figure 5.2, still show a clear discrepancy between each other.

It can be noted that the boundary layer thickness varies with spanwise position. At the centre of the tunnel (i.e. $z = 0$ [mm]), the boundary layer has the greatest thickness while it decreases when moving away from this centre. This behaviour might seem opposite to what one would expect. After all, near the centre of the tunnel only one boundary layer is present, while at the corner region, two boundary layers merge. However, the observed behaviour can be explained by the presence of ‘corner vortices’.

These vortices are typical for flow along a corner and flow in non-circular ducts. In literature this phenomenon is described as Prandtl’s secondary flow of the second kind, which is driven by turbulence [5]. Figure 5.3 schematically shows this vortex pattern for one quadrant in a fully developed channel flow. It can be seen that in each corner of the square duct, a pair of counter rotating vortices exists. Demuren et al. [9] present an extensive review of the literature on this topic. Basically, they conclude that the analysis of the streamwise vorticity equations, by Einstein and Li [11], together with experimental studies have shown that the gradients of Reynolds stresses give rise to this secondary motion. For further details on the origin of this secondary motion the reader is referred to [9].

Generally, the magnitude of this secondary motion is found to be in the order of 1 % of the mean axial velocity [4][25]. This directly explains why this secondary current was not observed

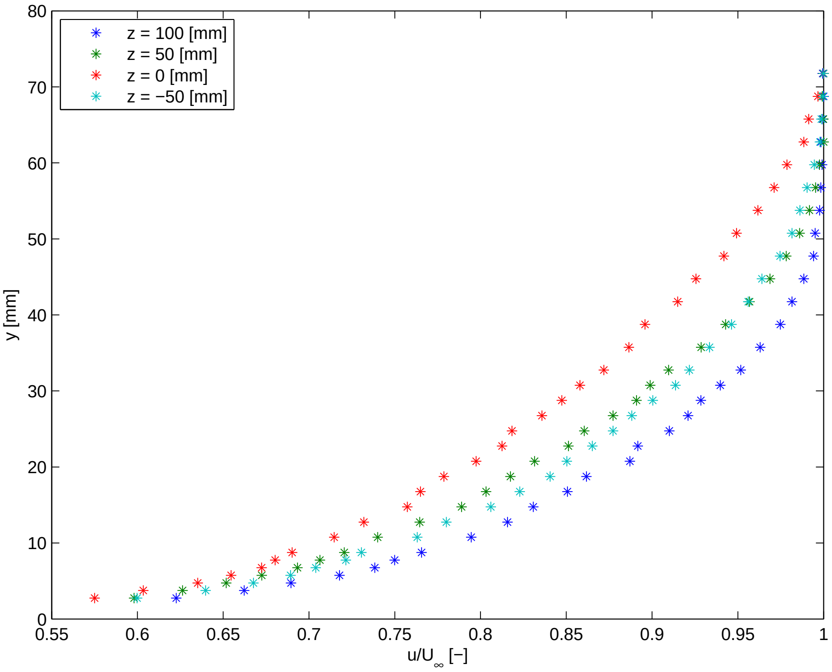

Figure 5.2: Normalised velocity profiles at different spanwise positions, for the zero pressure gradient case without suction (obtained at $x = 400$ [mm]).

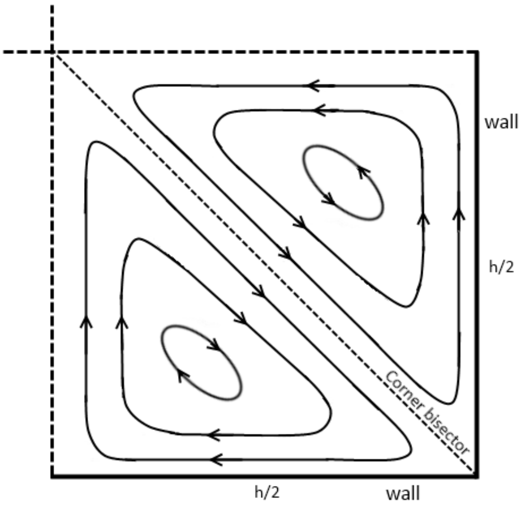

Figure 5.3: Schematical representation of vortex streamline pattern in one quadrant of a channel with height, h.

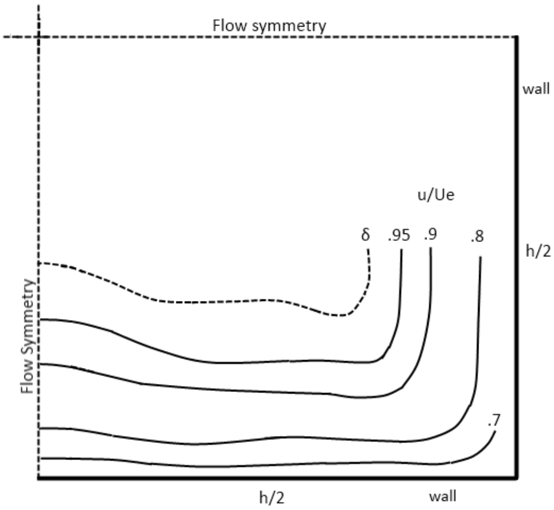

Figure 5.4: Isovelocity pattern near the corner of a channel due to secondary flow. Image adapted from [41]. Note that the image has been adapted to have the flow symmetry plane match with the actual symmetry plane.

z [mm]	H [-]	δ_{99} [mm]
-50	1.384	55.8
0	1.391	64.8
50	1.397	52.8
100	1.394	46.8

Table 5.1: Boundary layer shape and thickness at different spanwise positions.

with the use of tufts during the experiment. Despite the low secondary velocities, the influence of this motion is found to be significant. Veenhuizen et al. [41] investigated the effect of these secondary effects for a developing duct flow within a wind tunnel with a 2.0 x 2.0 [m] cross-section. Figure 5.4 schematically shows the effect of the secondary flow on the axial isovelocity contours in one quadrant of the wind tunnel cross-section. This pattern, found by Veenhuizen et al., is approximately at the same development length as for the current experiment. Therefore is assumed to be representative for the qualitative behaviour in the current channel.

One can observe from figure 5.4 that the boundary layer thickness varies across the tunnel, with its maximum in the middle of the tunnel. In table 5.1 the calculated boundary layer thickness for each spanwise position can be found, for the velocity profiles in figure 5.2. It can indeed be observed that at the mid-span position, the thickness is highest, while it decreases for the positions away from the middle of the tunnel. This observation agrees with the trends presented in figure 5.4.

Despite the presence of this axial isovelocity pattern and thus the spanwise varying boundary layer thickness, it was found that for the current measurements, the variation in shape factor across the span is negligible. That is, the shape factors of the boundary layer profiles in figure 5.2 were found to be within 1 % of each other. This can also be observed from the values presented in table 5.1.

Since the magnitude of the secondary motion was very small and the shape of the boundary layer did not noticeably vary along the span, the flow was still considered to be of a two-dimensional nature. That is, it was assumed that the setup remained valid for the use of two-dimensional boundary layer measurements.

z [mm]	RMS deviation from mean slot velocity [%]
-150	1.7
-100	2.6
-50	1.1
0	1.3
50	5.5
100	1.7
150	2.2

Table 5.2: Spanwise variation in slot velocity, averaged over three measurements.

5.1.2 Two-Dimensionality of the Suction Velocity

Apart from measuring the two-dimensionality of the flow field without suction, it was also attempted to determine the two-dimensionality of the suction velocity through the slot. To do so, a pitot tube was traversed by hand, in spanwise direction through the slot. Despite its intrusiveness and the rather crude way of traversing, the pitot measurements did give some insight in the variation of suction velocity. Table 5.2 shows the deviation from the mean spanwise slot velocity, averaged over three measurements. In order to obtain these values, a 'worst' case scenario has been assumed. That is, the slot width was chosen to be 30 [mm], and the suction rate was approximately 1.5 times the maximum suction rate, eventually used during the PIV measurements. Furthermore, the wind tunnel was turned on with a freestream velocity of 28 [m/s].

From table 5.2 it can be observed that the maximum deviation from the mean spanwise velocity is approximately 5 %. Taking into account the inaccuracy of the measurement method, as well as the fact that these tests were for a 'worst case scenario', the results are deemed acceptable. At least, the result is assumed to validate that the suction was two-dimensional enough to use the volume measurement method described in section 3.3.4.

5.1.3 Determination of the Sample Size

In order to determine the sample size (i.e. number of PIV image pairs), the convergence of the mean velocity and the velocity fluctuations was considered prior to the main experiment.

The convergence of the flow was checked by again considering the 'worst case' encountered during the experiment. Using the maximum suction coefficient, the region around the slot was checked for convergence. For this region, 750 image pairs were captured and processed using DaVis. For each of the resulting vector fields, the sum of all vectors was taken and the mean of this value, as a function of the sample size, was computed. The results for both the mean, and the fluctuating component of the velocity can be found in figures 5.5 and 5.6 respectively.

From these figures, it was determined that a sample size of $N = 500$, would be sufficient to ensure a converged mean velocity field. In order to determine if this sample size gives acceptable results from a statistical point of view, the resulting measurement uncertainty for the mean freestream velocity was determined. It was found that, for a freestream velocity of 28 [m/s], the theoretical uncertainty in the measured mean freestream velocity was below 0.05 % for a sample size of $N = 500$. Further details on this calculation can be found in section 5.6, where the measurement uncertainty of the experiment is discussed in general. Based on the above, the sample size for the PIV results was indeed chosen to be $N = 500$.

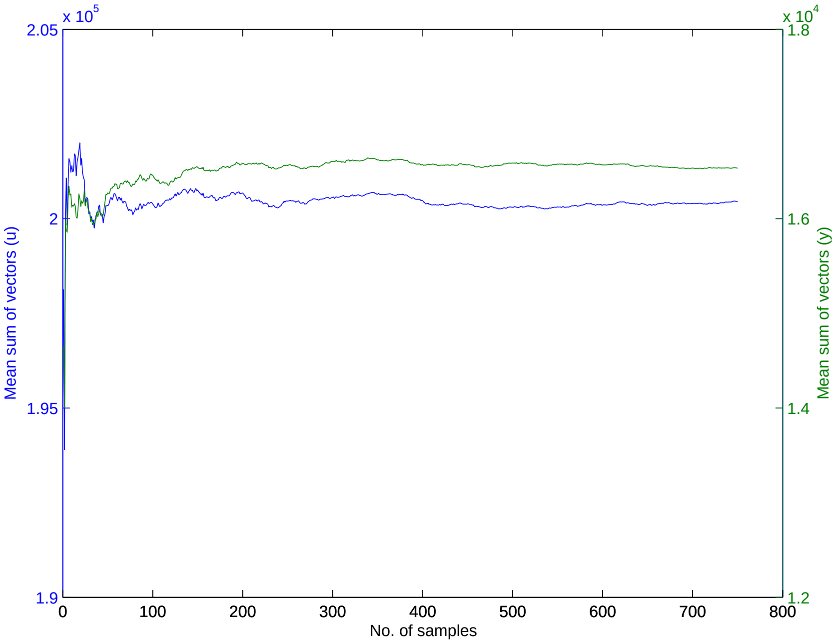

Figure 5.5: Convergence plot for the mean velocity in x- and y-direction.

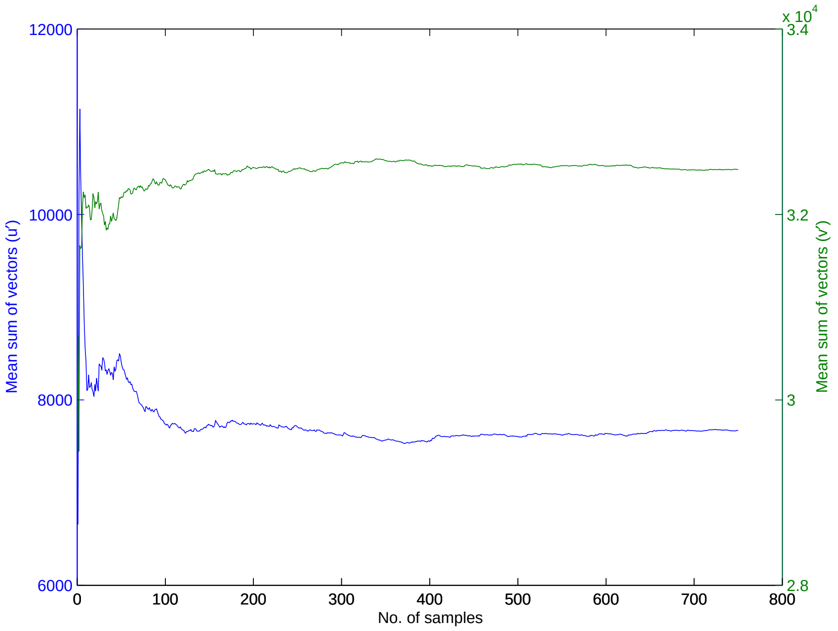

Figure 5.6: Convergence plot for the velocity fluctuations in x- and y-direction.

5.2 Slot Suction with Zero Pressure Gradient

Similarly to the investigations of Antonia et al. [2] and Park et al. [29], this section presents the results for slot suction of a zero pressure gradient turbulent boundary layer. However, the Reynolds number based on the momentum thickness, Re_θ, for the current results is an order of magnitude higher. Whereas the investigations in literature use Reynolds numbers of $\mathrm{Re}_\theta \approx 500$, the current Reynolds number in the undisturbed flow is found to be $\mathrm{Re}_\theta \approx 10{,}100$. This section will show to what extent the present results are comparable with the results from literature, which were summarised in section 2.2.2.

5.2.1 Measurement without Suction

Before presenting the results related to boundary layer suction, this section discusses the reference measurement for the zero pressure gradient turbulent boundary layer. Firstly, the general boundary layer development and the observed errors are discussed. The reference values, θ_0 and δ_0 are also indicated. Secondly, the measured boundary layer is compared with a theoretical zero pressure gradient turbulent boundary layer. The observed similarities and differences with respect to theory are discussed and explained.

General boundary layer development

This paragraph describes the measured boundary layer development in a qualitative sense. In order to do so, let us consider figure 5.7. This figure shows the streamwise development of the momentum thickness, θ, without the application of suction.

Due to the physical nature of the problem, one would expect this parameter, θ, to be monotonically increasing in x-direction. However it can be seen that near x = -120 [mm] and, more pronounced, near x = 320 [mm], a hump is present. Closer inspection shows that the deviation from the trend at these locations is in the order of magnitude of 3 %. Although this deviation is relatively small, it is important to identify its cause. If, for example, these humps are caused by a physical phenomenon not included in the analysis of the results, erroneous conclusions might be drawn.

Obviously, the humps cannot be explained from the physics of a zero pressure gradient boundary layer. Therefore, two possible causes for the presence of these humps can be proposed. They can either be caused by an unexpected physical phenomenon due to, for example, a flaw in the experimental setup, or they can be caused by some sort of measurement error.

Let us now focus on the most pronounced hump in the results, near x = 320 [mm]. It has been found that this hump is visible in nearly all results for the momentum thickness. That is, not only for the zero pressure gradient case, but also for the adverse pressure gradient case. The same result is also found for the displacement thickness, δ^*. It turns out that for some cases with suction, the humps decrease in amplitude though. In view of this effect, one might suspect the cause for the humps to be physical. However, the opposite is true, as will be shown below.

To explain the cause for this hump, let us consider the velocity profiles at $x \approx 320$ [mm] and at $x \approx 390$ [mm]. In figure 5.8, it can be seen that the velocity profiles are very close to each other, until y reaches a value of $y \geq 30$ [mm]. At the edge of the boundary layer, the freestream velocity for $x \approx 320$ [mm] is approximately 0.3 [m/s] higher than for the position further downstream. Since the velocity profile is normalised by this freestream velocity for the calculation of θ, the apparent momentum loss will indeed be higher for the velocity profile at $x \approx 320$ [mm].

Figure 5.9 now shows the freestream velocity, determined using the procedure described in section 4.2.1, versus the streamwise location, x. It can be seen that there is a variation within this velocity, also in the form of humps. The locations of these humps correspond to the location of the humps

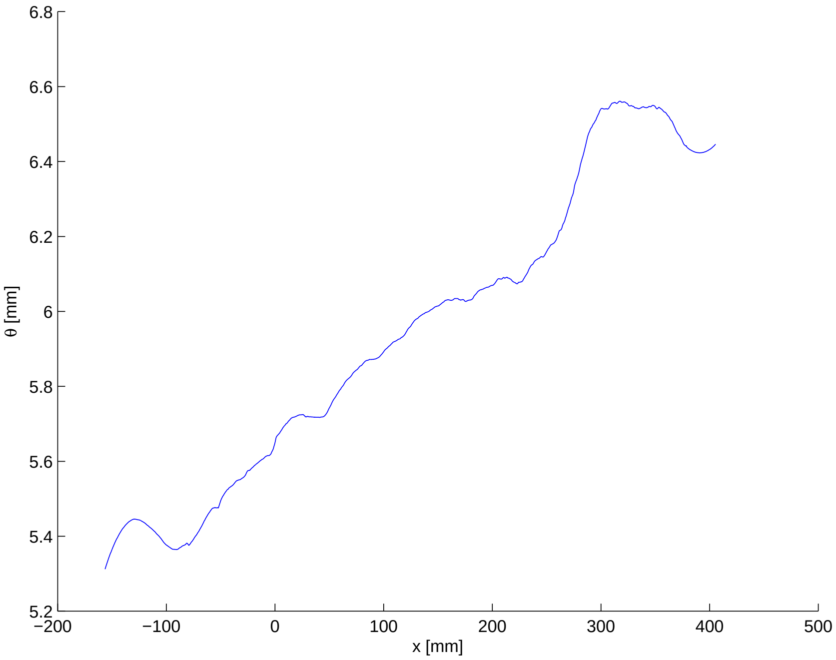

Figure 5.7: Streamwise development of the momentum thickness for flat plate boundary layer. Smoothing: Sgolay(2,200).

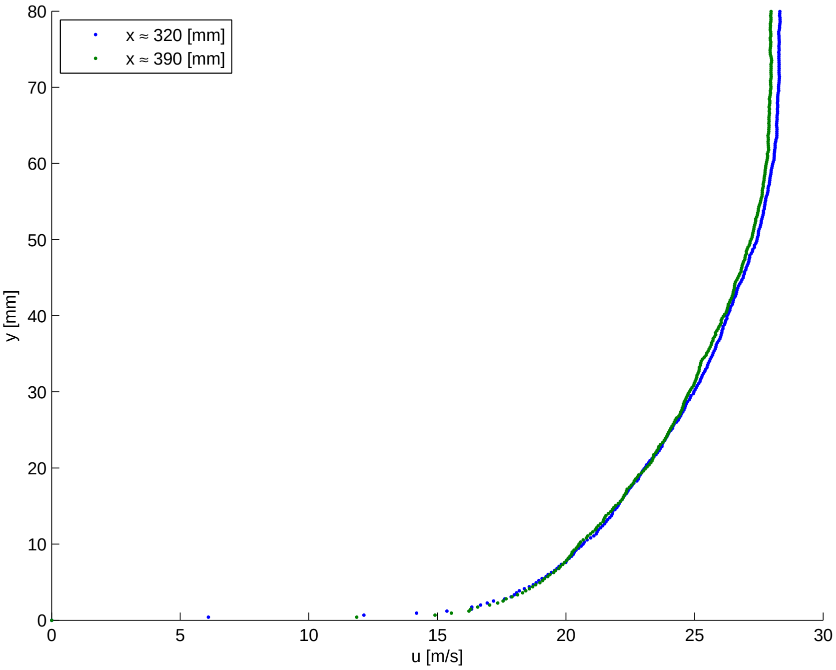

Figure 5.8: Velocity profiles for streamwise positions at and beyond the hump in the results.

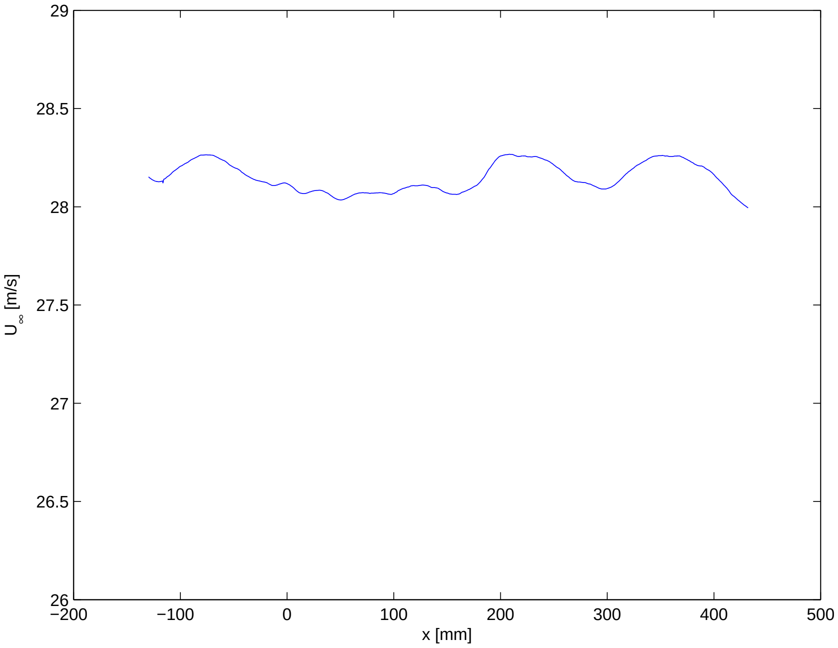

Figure 5.9: Streamwise development of the freestream velocity. Smoothing: Sgolay(2,100).

in the result for θ. However, since there is no pressure gradient, this velocity should be constant throughout the domain. The freestream velocity was controlled to be 28 [m/s], using a pitot tube. Again, no physical cause for a sudden increase in freestream velocity could be identified.

Additionally, it has been found that the measured RMS fluctuations are also higher in the regions where these humps are present. This can be seen in figure 5.10. Obviously, if a higher velocity is measured, the measured RMS fluctuations should also be higher. However, the increase in RMS fluctuations near the humps is close to 100 %, while the freestream velocity only shows an increase in the order of 1 %. Therefore, there must be another cause for the RMS fluctuations to increase so heavily in these regions.

Inspection of the data within DaVis has shown that the correlation peak ratio (i.e. the ratio between the highest and the second highest peak in the correlation map) is lower in those regions of increased RMS. Going back one step further, it was observed in the raw images that the particles in those regions with increased RMS were out of focus, to an undesirable extent (see figure 5.11). The fact that particles are out of focus, causes a decreased accuracy of the results due to a lower signal to noise ratio, as explained in section 2.3.

The author feels that the combination of the above observations can only lead to one conclusion regarding the source of the humps in the results. It is believed that the humps originate from lens distortions, which are of a too high order to correct for, using the calibration procedure in DaVis (third order polynomial correction). A relatively low f-stop has been used for the images to be bright enough (see section 3.4). However, due to lower f-stop, a larger part of the lens is used, increasing the possibility of having lens distortions. These lens distortions cause an error in the magnification, which results in local bias errors in the measured velocity. The other consequence of using a low f-stop, is that the field of focus is slightly 'curved'. This causes the outer parts of the images to be slightly out of focus, resulting in the higher RMS fluctuations.

Unfortunately, the distortion is of such a nature that no additional general correction can be applied to the velocity field. Especially for the results of the zero pressure gradient case, the erroneous humps are disturbing for interpreting the results. While the variation from the trend

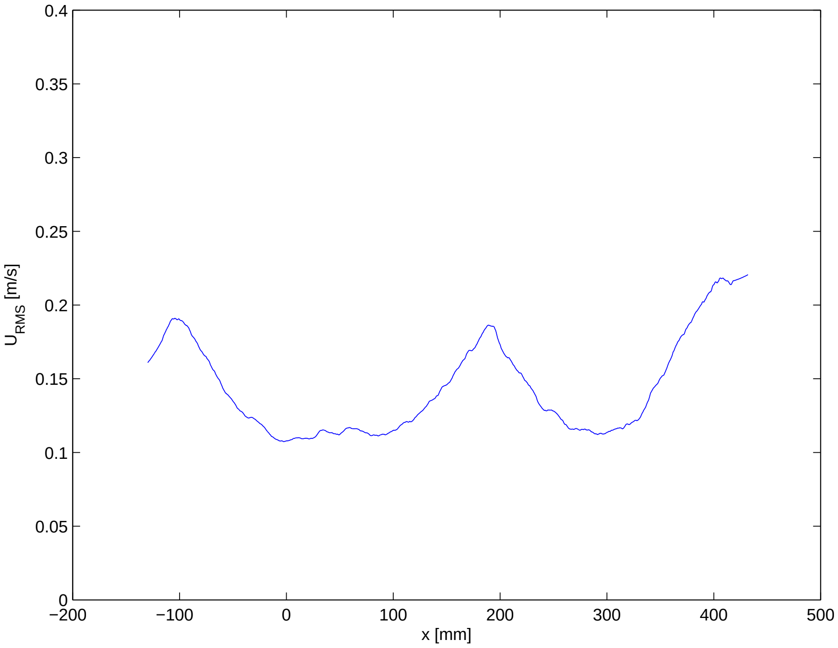

Figure 5.10: Streamwise development of RMS fluctuations in the freestream velocity. Smoothing: Sgolay(2,100).

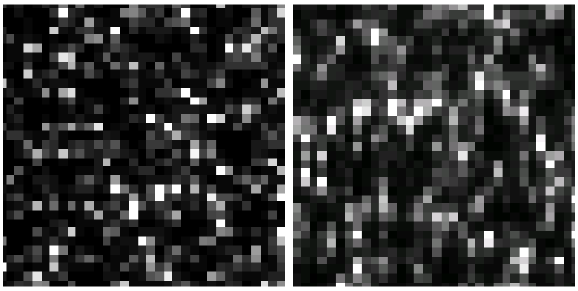

(a) Low RMS (b) High RMS

Figure 5.11: Imaged particles in and out of focus in the low and higher RMS zones respectively.

near the hump is only 2 to 3 % from the measured local value of θ, it is approximately 20 % of the variaton of θ over the measurement domain. In order to improve the readability of the results in this section, mostly trendlines will be used. For all figures, the original data is also included in appendix D.

Finally, let us come back to the observation of the amplitude of the hump being dependent on the suction rate. This can simply be explained by the fact that the boundary layer is thinner after the application of suction. From figure 5.8 it could be observed that the error was present in the upper part of the velocity profile. Having a thinner boundary layer rearward of the slot, due to suction, the error in magnification now occurs mostly outside the boundary layer region.

Fortunately, the data at $x = 0$ [mm] is not biased by these humps. The reference momentum thickness is found to be $\theta_0 = 5.6$ [mm]. With a freestream velocity of 28 [m/s], the resulting Reynolds number was found to be $\mathrm{Re}_\theta \approx 10{,}100$. Furthermore the boundary layer thickness at this position was found to be $\delta_0 \approx 50$ [mm]. These reference values have been used to calculate the right suction coefficient, σ and slot width, W.

For this zero pressure gradient case, using the ratio $\frac{W}{\delta_0} = 0.2$ resulted in a fixed slot width of: $W = 10$ [mm]. Furthermore, the suction coefficient, σ, was determined by controlling the suction volume, and thus suction velocity (see equation 2.21). All other parameters in equation 2.21 were fixed.

Validation of flat plate boundary layer growth

The behaviour of a flat plate turbulent boundary layer without suction is quite well understood and described in literature. To validate the results obtained from the current experiment, the flat plate measurements will be compared to theoretical behaviour in this section.

A very convenient estimation for a zero pressure gradient turbulent boundary layer is the relation between its growth and the freestream Reynolds number, Re_x. An often used approach for this purpose is to assume a simple one-seventh power-law profile which results in direct approximate relations between Re_x and the integral parameters [45]. However, in section 5.1.1 it was shown that the boundary layer development differs across the span due to the presence of corner vortices. So, while the local Re_x is the same for each of these spanwise positions, the boundary layer is not. Furthermore, due to the developing boundary layer in the channel before the region under investigation, there is a slight positive pressure gradient within the channel. Therefore these relations cannot be applied to the current boundary layer measurements. Instead the theory discussed in chapter 2 is used.

Figure 5.12 shows the trend for the development of the shape factor in streamwise direction. To obtain this trendline, a linear regression is performed, ignoring the data outside the range $-100 \leq x \leq 300$ [mm]. One can observe that the shape factor seems to remain nearly constant at a value $H \approx 1.34$. As already mentioned in section 2.1.1, this is an approximate value for a turbulent boundary layer at a zero pressure gradient. More specific, by using the results for a theoretical velocity profile described by Coles' law of the wake (equations 2.16 and 2.18) it is possible to calculate the shape factor, based on the local value of Re_θ and Π. For a zero pressure gradient turbulent boundary layer the wake parameter typically has a value of $\Pi \approx 0.5$ [45]. Using this value for Π and the value of Re_θ from the current experiment, a theoretical decrease of H from 1.31 to 1.30 over the domain is calculated. Although there is a deviation between the two, it is not larger than 3 %. Therefore, the author feels that the result in figure 5.12 indicates an approximate zero pressure gradient behaviour for the measured boundary layer.

As already described in chapter 2, most theoretical descriptions of turbulent boundary layers involve a generalised velocity profile. This velocity profiles relies on non-dimensionalisation by the friction velocity (see section 2.1.3). To be able to compare the current results with theory, it is therefore needed to non-dimensionalise the data, using the friction velocity. From equation 2.10 it

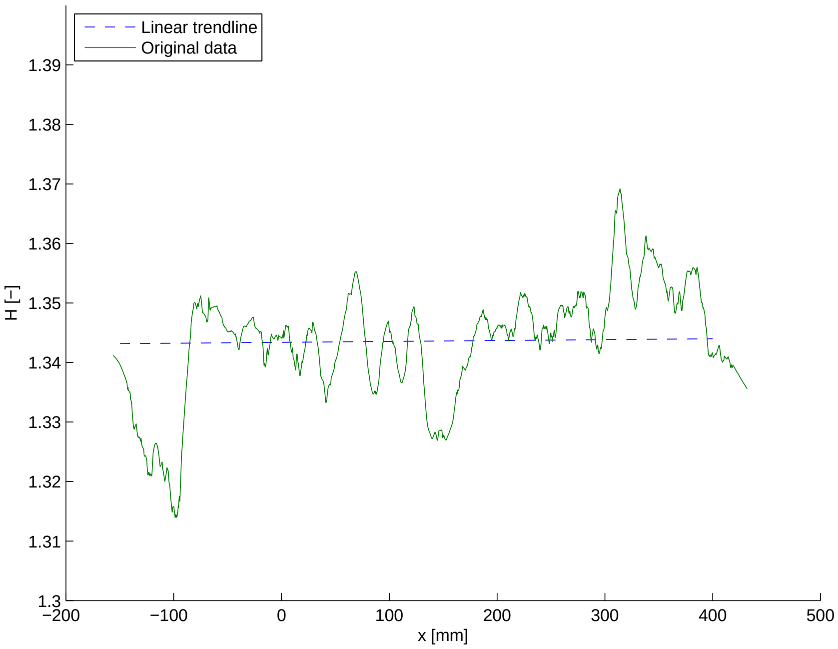

Figure 5.12: Streamwise development of the shape factor for the zero pressure gradient boundary layer. Linear trendline, based on data for -100 $\leq x \leq$ 300, vs. original smoothed data (Sgolay(1,20)).

can be observed that the friction coefficient, C_f, is needed to determine this friction velocity. Then from its definition in equation 2.5, it can be seen that C_f is a function of the velocity gradient at the wall. Since no direct measurement of the velocity gradient at the wall has been performed (the first data points are not close enough to the wall), the friction coefficient has been determined otherwise.

The Clauser technique, which relies on the validity of the universal log-law (see section 2.1.3), has been applied to obtain the friction coefficient. Although this technique has its limitations, especially at low Reynolds numbers, it is believed to give a good estimate of the local skin friction coefficient [14]. Figure 5.13 shows the fitted log law together with the measured velocity profile for two positions within the measurement domain. These positions, x = -50 and x = 250 [mm] have deliberately been chosen to avoid the regions where the humps in the integral parameters where found (see figure 5.7). For these positions, it can be seen that the log law nicely collapses with the velocity profile data. This is reflected by the low RMS error presented in table 5.3. Note that the logarithmic law is only applicable to boundary layers without suction. Therefore the Clauser technique cannot be applied for the cases with suction, as the velocity profile does not match the logarithmic law.

Figure 5.14 shows the same profiles with a fit of the complete overlap and outer layer according to Coles' law of the wake. To optimise this fit, the value of C_f is set to the one obtained through the log law fit, while the value of Π is allowed to vary. The value of Π is found to vary from $\Pi \approx 0.45$ to 0.55 over the domain, which approximately corresponds to a zero pressure gradient boundary layer [45]. Table 5.3 summarises the characteristic values found for both fits for the velocity profiles in figures 5.13 and 5.14.

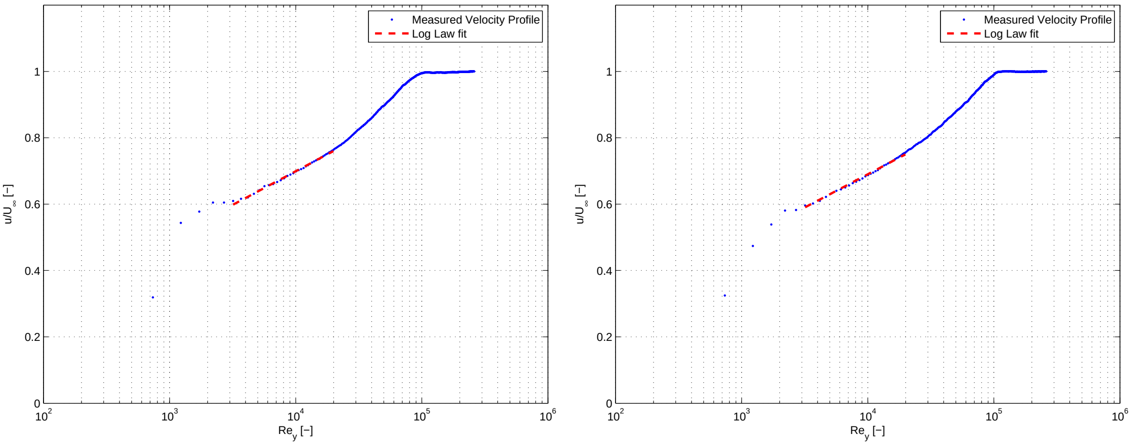

(a) x = -50 mm (b) x = 250 mm

Figure 5.13: Fit of the logarithmic law for two velocity profiles at different streamwise locations for the zero pressure gradient case without suction.

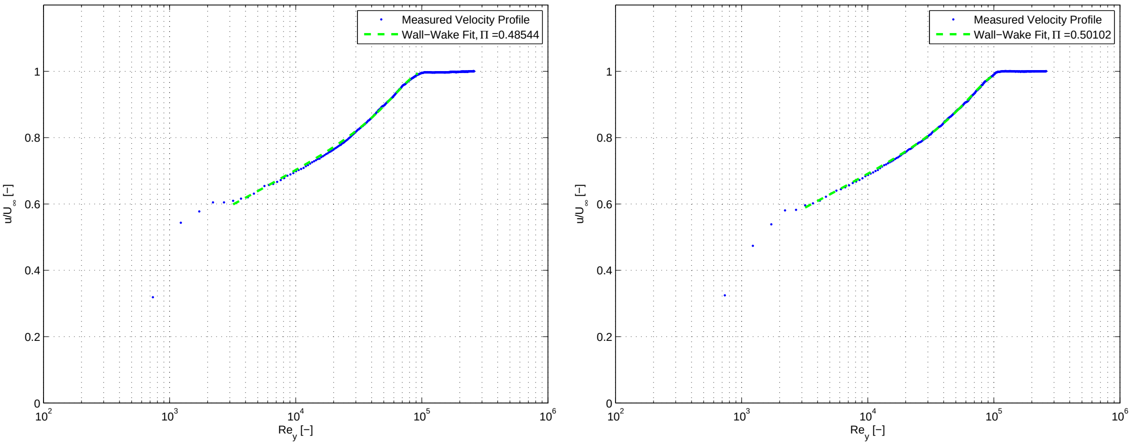

(a) x = -50 mm (b) x = 250 mm

Figure 5.14: Fit for Coles' law of the wake for two velocity profiles at different streamwise locations for the zero pressure gradient case without suction.

	x = -50 [mm]	x = 250 [mm]
C_f (Clauser) [-]	0.00261	0.00255
RMS error log law fit [-]	0.0030	0.0033
Π (Coles) [-]	0.485	0.501
RMS error Coles fit [-]	0.0037	0.0027

Table 5.3: Results for the log law fit and Coles' wall of the wake fit at x = -50 [mm] and x = 250 [mm] for zero pressure gradient case without suction.

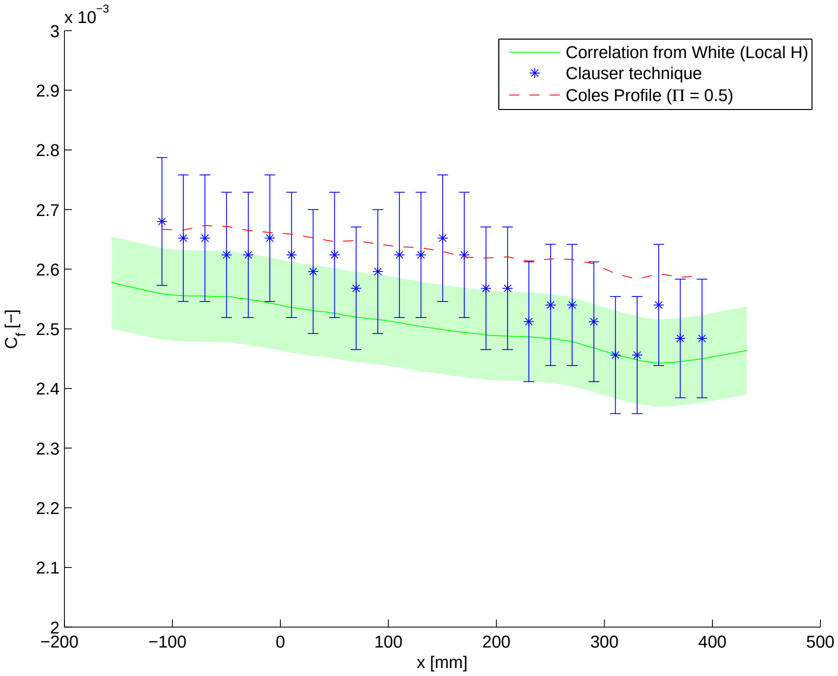

Figure 5.15: Friction coefficient obtained through Clauser technique compared with theoretical friction coefficient from White for the zero pressure gradient case.

Figure 5.15 shows the friction coefficient obtained by the Clauser technique, together with the theoretical approximation from White in equation 2.19, which uses the measured values of H ($\approx$ 1.34) and Re_θ. This latter is based on Coles' law of the wake and has an approximate accuracy of 3 % [45]. Typical values for the accuracy of the Clauser plot technique to determine the friction coefficient are in the range of 3 to 5 % [43][8][39]. The uncertainties for both approximations are also depicted in figure 5.15. The third, red dashed, line in figure 5.15 represents the friction coefficient for a theoretical Coles' velocity profile, based on the local value of Re_θ and $\Pi = 0.5$. This has again been obtained by using the combination of equations 2.16 and 2.18.

Comparing the results for the correlation from White and the Clauser technique it can be observed that they show fair correspondance when taking into account the uncertainties of both methods. There does seem to be an offset in the order of 0.1 ($\approx$ 3.5 %) between the results. It should be noted that the outcomes of this correlation are very sensitive to the value of H. Above it was seen that the value of H was somewhat above the theoretical value from Coles', which can explain the offset between the two results. To check for this, the direct results from a theoretical Coles' profile, which does not use the local measured value of H, were added. Indeed this result gives a better match, especially at the beginning of the domain. Here the deviations are in the order of 1.5 %. The trend from the theoretical Coles' profile appears to be somewhat less steep than the one for the Clauser technique. This is indicative for a slight adverse pressure gradient, which matches the earlier finding that Π increases from 0.45 to 0.55 over the domain. However, the maximum offset between a linear trend through the Clauser technique and the result from the theoretical Coles profile is not larger than 5 %. Therefore it is assumed that the results are approximately corresponding to the theoretical behaviour of a zero pressure gradient boundary layer.

Now, let us consider the streamwise development of the momentum thickness, already shown in figure 5.7, at the beginning of this section. According to the von Kármán integral relation in equation 2.9, for a zero pressure gradient boundary layer, the streamwise rate of change of the momentum thickness can be directly related to the local skin friction coefficient. Using the skin

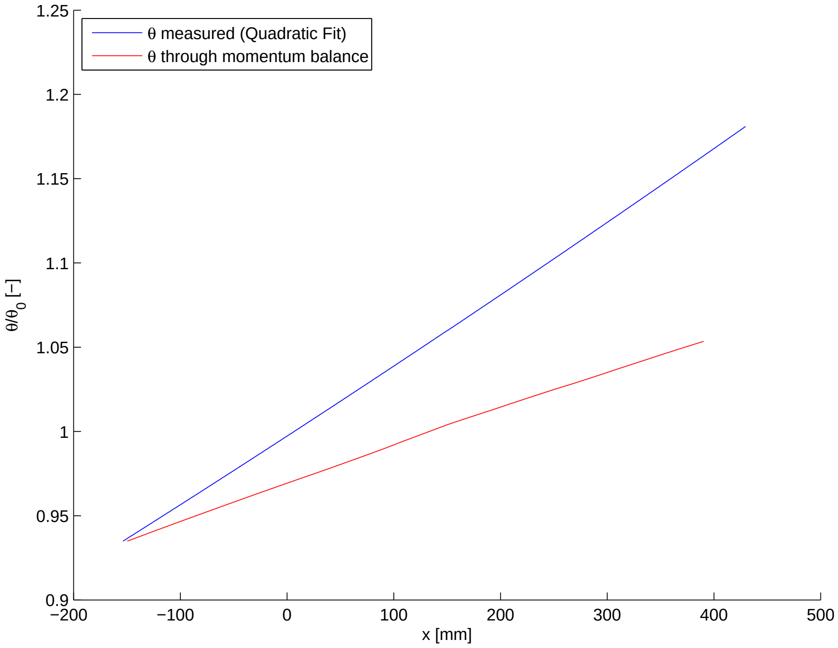

Figure 5.16: Streamwise development of the measured momentum thickness compared with the value obtained from integrating the momentum integral relation.

friction coefficient obtained from the Clauser plot technique, this relation is numerically integrated to predict the streamwise development of a two-dimensional zero pressure gradient boundary layer. Figure 5.16 shows the measured and theoretically predicted growth for θ. Note that this time, a trendline is used for the presentation of the measured value of θ.

It can be observed that there is a clear discrepancy between the theoretical and the measured growth of the momentum thickness. The increase in momentum loss in the measured boundary layer is nearly twice the theoretical value. When considering the two-dimensional integral momentum equation in its complete form, three possible causes can be identified for this discrepancy. Either the value of C_f obtained from the Clauser technique is too low, or the pressure gradient is incorrectly assumed to be zero, or the momentum integral relation cannot be applied to this boundary layer. From wall pressure measurements however, it was seen that the pressure gradient is negligibly small (see figure 5.22). Furthermore, the value of C_f obtained from the Clauser technique, although being slightly lower, approximately corresponds to the one obtained from theory for a zero pressure gradient boundary layer.

As an additional check it was calculated, from the integral momentum equation, which pressure difference, Δp, should have been present to cause the observed development of θ. Based on a linear approximation of all variables, it is found that this Δp should have been approximately 20 [Pa] over the measurement domain. A variation of this order of magnitude would most certainly have been measured through the pressure taps. In the same way it was also estimated which value of C_f should have been present to explain the measured growth for a zero pressure gradient boundary layer. This is found to be approximately $3.8 \cdot 10^{-3}$, which is nearly 1.5 times higher than the results for C_f in figure 5.15. Therefore, it is clear that such something else must have caused the increased rate of growth for the momentum loss.

Summarising the findings until now, the boundary layer seems to have all the characteristics of a two-dimensional zero pressure gradient boundary layer, but its streamwise development does not obey the two-dimensional integral momentum equation. The latter can therefore not be used to

Boundary [mm]	2-D ‘volume flow’ [m^2/s]
x = -50	-3.3316
x = 250	3.3049
y = 120	0.0633

Table 5.4: Calculated two-dimensional ‘volume flows’ to check for continuity for -50 ≤ x ≤ 250 [mm] for the zero pressure gradient case.

Boundary [mm]	2-D ‘volume flow’ [m^2/s]
x = -50	-3.3188
x = 250	3.2896
y = 120	0.0327

Table 5.5: Calculated two-dimensional ‘volume flows’ to check for continuity for 0 ≤ x ≤ 150 [mm] for the zero pressure gradient case.

estimate the friction coefficient for the current experiment. The author believes that the most likely explanation for the faster growth of the momentum thickness is the presence of ‘corner vortices’, earlier described in section 5.1.1.

Although the secondary flow has a low velocity, it moves high momentum fluid from outside the boundary layer, along the corner bisector towards the corner [9]. Low momentum fluid then moves along the wall, away from the corner towards the symmetry plane. There it is transported through the boundary layer upwards into the freestream [9]. This typical ‘redistribution’ of low momentum fluid offers a possible explanation for the increased momentum thickness found in the current measurements. Since the measurement plane is very close to the symmetry plane, low momentum fluid is moved towards the measurement plane from the corners likely causing an increase in the measured streamwise momentum loss in the boundary layer.

Unfortunately, the author has not been able to assess whether this phenomenon also quantitatively matches with the measurements. In order to do so, more information is needed on the axial velocity pattern. Possibly, the difference in the theoretically predicted momentum thickness and the measured momentum thickness is due to a combination of the corner vortices, a slight adverse pressure gradient and a small error in the measured value of C_f.

To assess the influence of the secondary flow on the two-dimensionality on the flow field, the volume continuity equation (see equation 2.7a) was considered over a domain described by: -50 ≤ x ≤ 250 [mm] and 0 ≤ y ≤ 120 [mm]. For each of the boundaries of the domain, table 5.4 shows the result of the integrated velocity, according to the divergence theorem. Here a positive value corresponds to a flow out of the domain. Note that the velocity at y = 0 [mm] was assumed zero, as no suction was present.

The result of the integration is found to be 0.037 [m^2/s] corresponding to approximately -1 % of the inflow at x = -50 [mm]. However, it should be noted that the result is easily influenced due to the magnification errors, causing an error in the measured velocity (see figure 5.8). Performing the same integration for a domain with the same height but with an x-range of 0 ≤ x ≤ 150 [mm], results in an error of only -0.1 % (see table 5.5). Taking this into account, it appears that the effect of the vortices on the level of two-dimensionality of the flow field is relatively small.

5.2.2 Flow Pattern due to Suction

This section discusses the qualitative flow pattern observed due to the application of slot suction. Before presenting results in terms of boundary layer characteristics, it is important to understand and also validate the observed flow pattern.

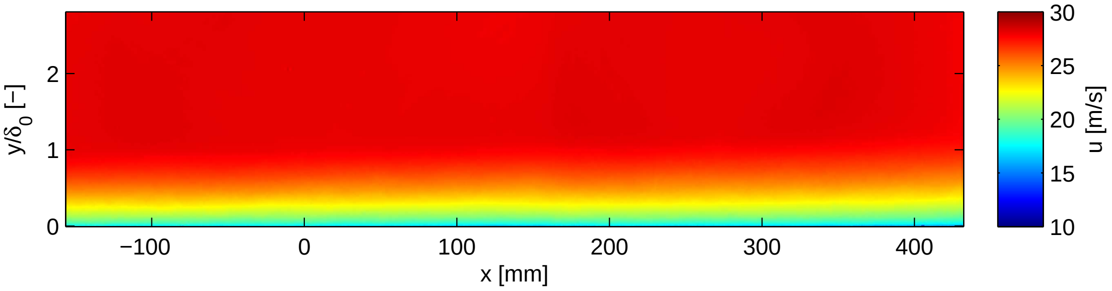

Figure 5.17: Streamwise velocity for zero pressure gradient without suction.

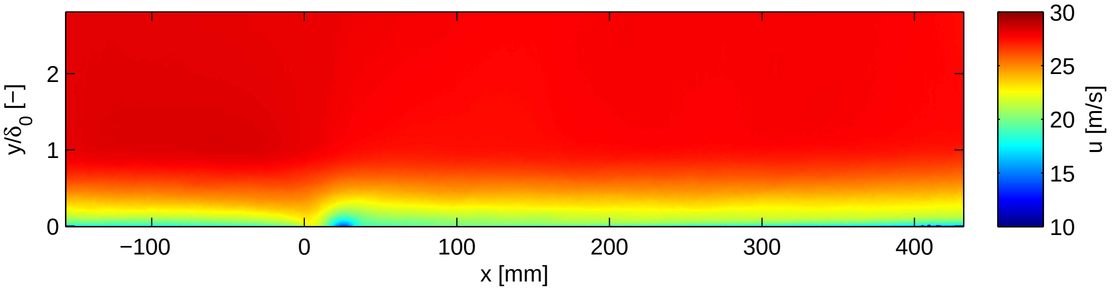

Figure 5.18: Streamwise velocity for zero pressure gradient with suction, $\sigma = 0.7$.

Figure 5.17 shows the mean velocity component in streamwise direction in the absence of suction, while figure 5.18 shows this result for the case with suction, for $\sigma = 0.7$. It can be observed that near the slot, the flow pattern is significantly affected due to the suction. Most distinctive, is the region of relatively low streamwise velocity directly behind the slot, near $x = 30$ [mm]. However, due to the relatively large velocity scale (10-30 [m/s]) it is hard to exactly see the influence of the slot on the flow pattern.

In order to illustrate the effect of slot suction on the mean flow field more clearly, figure 5.19 shows the difference between the streamwise velocity fields for the flat plate case and the case with suction, for $\sigma = 0.7$. Now, it can cleary be observed that in front of the slot the flow is accelerated due to suction, while behind the slot it is decelerated. Furthermore, it can be observed that after the slot, an increase in velocity is present in the region close to the wall. The withdrawal of the fluid has thus caused an increased near-wall velocity downstream of the slot, indicating a reduction in θ and δ^*.

In order to understand the observed behaviour close to the slot, let us draw the analogy between the current viscous flow and a similar problem for potential flow. Although the boundary layer flow does not obey the condition of irrotationality, it is still assumed to be possible to use the potential flow superposition argument in order to explain the qualitative behaviour of the flow. This assumption is based on the fact that the qualitative nature of the local flow disturbance due to the presence of a slot is dominated by convective effects.

Figure 5.20 shows how the addition of a uniform flow and the flow through the slot, without presence of a cross-flow, give the combined streamline pattern including a stagnation point. From this analogy, it can now easily be seen, that in front of the slot, the streamwise velocity is increased due to the addition of the slot flow to the uniform flow, while behind the slot the opposite is true. Furthermore, the resulting streamline pattern shows that near the rear edge, a stagnation point occurs. Depending on the strength of suction, this point will move up or down. The streamline

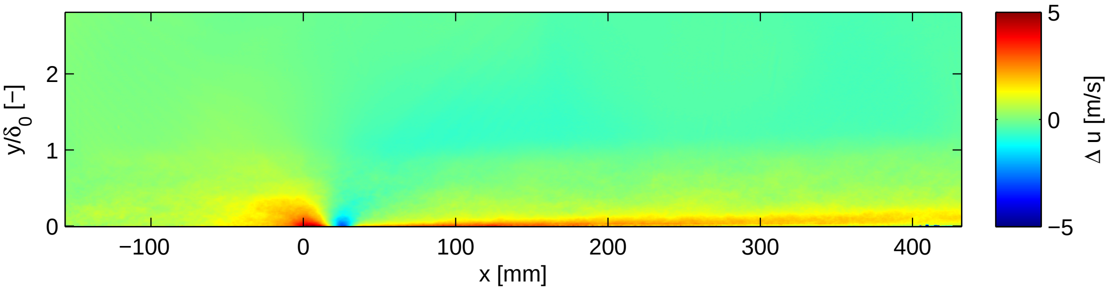

Figure 5.19: Difference in streamwise velocity for zero pressure gradient case without suction and with suction, $\sigma = 0.7$.

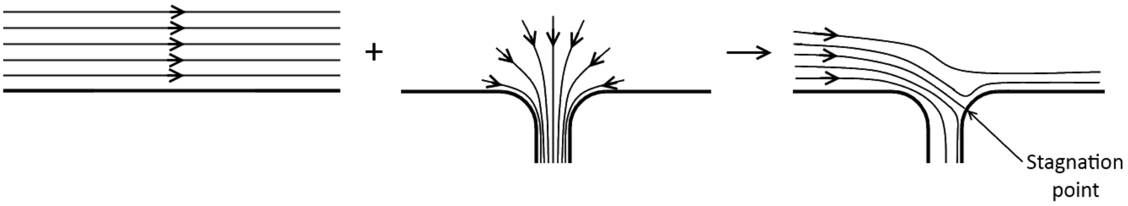

Figure 5.20: Qualitative representation of the streamline pattern around slot, due to superposition of two potential flows.

pattern also shows an additional upward velocity near the rear edge.

Figure 5.21 shows both velocity components for the region close to the slot. It can indeed be observed that there is an upward velocity component for the region near $x = 30$ [mm]. Furthermore, the calculated streamline pattern matches the one explained in figure 5.20.

The reduction in near-wall velocity as compared to the reference measurement, rearward of the slot, has an important implication with respect to the use of slot suction. If the undisturbed boundary layer would be close to separation, the application of slot suction might actually give rise to separation. For airfoil design this might pose an extra criterion on the positioning of the slot.

As a final observation, turning back to figure 5.19, it can also be noted that the freestream velocity behind the slot is reduced. This can be explained by considering conservation of volume of the air flowing through the tunnel. First of all, the volume removed through the slot causes a reduced volume flow through the tunnel. Since the tunnel cross-section does not change, the mean velocity through the tunnel should then also reduce. Furthermore, the increase in near-wall velocity as described earlier, causes a reduction in displacement thickness. This causes the effective area, for the air to flow through, to increase, which again results in a reduction of free stream velocity.

In conclusion, this section has shown the general flow pattern caused due to the application of slot suction. All phenomena that were observed could be explained and therefore the obtained mean velocity fields appear to be valid, at least qualitatively.

5.2.3 Effect of Suction on the Pressure Distribution

This section presents the results for the effect of slot suction on the pressure distribution. To do so, the data obtained from the wall pressure taps is evaluated and compared with the results

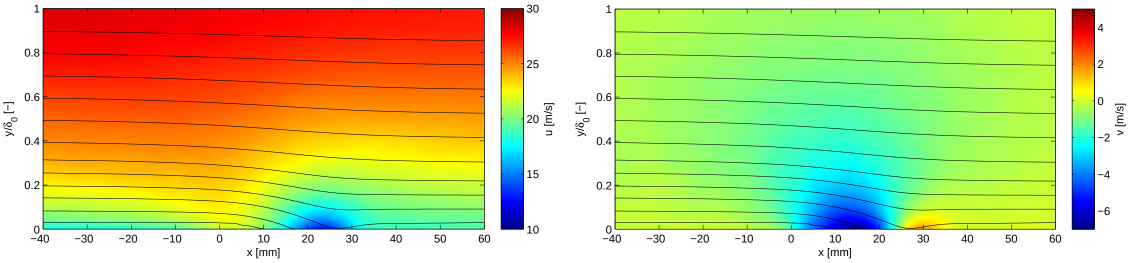

(a) Streamwise velocity

(b) Wall-normal velocity

Figure 5.21: Streamwise, wall-normal velocity and measured streamline pattern for the region close to the slot with suction, $\sigma = 0.7$.

from Park et al. [29] and Kim et al. [22] already described in section 2.2.2. Furthermore, the pressure obtained from the PIV velocity field is validated by comparing it to the data from the wall pressure taps. Finally this entire pressure field is used for further evaluation and validation of the effects of slot suction.

Figure 5.22 shows the effect of suction on static pressure at the wall, in front of and behind the slot. This mean pressure, measured through the wall taps, is the result of averaging 200 samples which were obtained with a frequency of 10 [Hz]. From the flat plate measurement it can be seen that the pressure gradient is negligibly small and therefore validly assumed to be zero. Furthermore, it can be seen that due to the application of suction, the flow experiences a favourable pressure gradient in front of and behind the slot. Although no data is available above the slot, it can be observed that an adverse pressure gradient must be present there to have a continuous pressure distribution. This is shown by the dotted lines in figure 5.22. The current observations correspond to the ones in [22] and [29]. If one compares the current data with figure 2.7 in section 2.2.2, the same trends can indeed be observed.

From figure 5.22 it also can be seen that behind the slot, at $x \approx 250$ [mm], a difference in pressure remains to exist for the cases with different σ. It is found that the pressure increases for increasing suction. It has already been mentioned above, that suction causes a decrease in freestream velocity due to conservation of mass. Now, assume that at this position, relatively far away from the slot, $\frac{\partial p}{\partial y}$ is approximately zero. This means, that the wall pressure is equal to the freestream pressure. Now, assuming that the Bernoulli equation is valid in the freestream, the reduction in freestream velocity is directly related to an increase in freestream static pressure, and thus wall pressure.

As a means of validation, in appendix E, the reduction in mass flow has been calculated from this reduction in static pressure. The resulting reduction in mass flow was then compared with the measured mass flow through the slot. It has been concluded that these two mass flows can indeed be linked to each other.

Using the method described in section 4.5, the measured velocity field has also been used to determine the pressure field and from this the wall pressure distribution. Figure 5.23 shows a comparison between the pressure obtained at the lower boundary of the domain and the one obtained through the wall taps for the case without suction. Note that the lower boundary of the pressure domain corresponds to a position of approximately 2-3 [mm] above the wall. From figure 5.23 it can be observed that there is a very good agreement between the two results, which already (partly) validates the results obtained by this method.

In the same way, the pressure distribution at the lower boundary of the domain, for the case where σ equals 0.7, is plotted in figure 5.24. Again a very good correspondence between the data obtained from the pressure taps and the data obtained from PIV can be found. Now it can

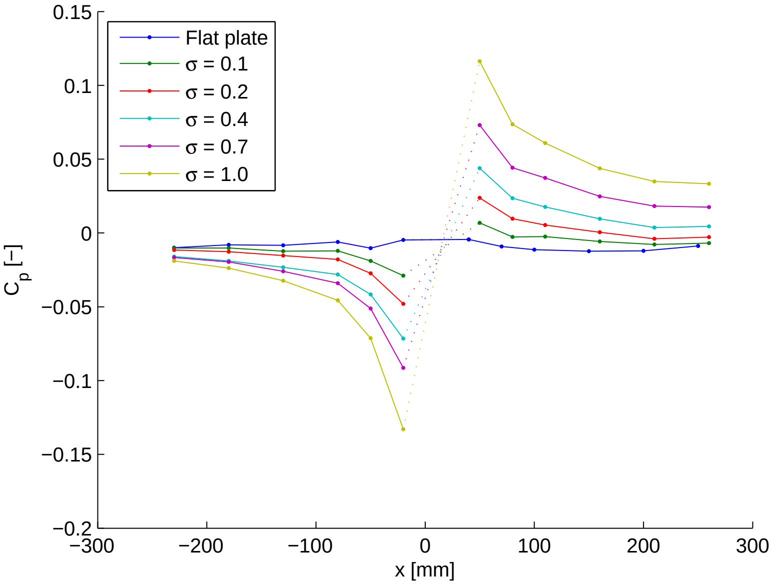

Figure 5.22: Streamwise development of the wall pressure coefficient due to the application of suction. Pressure obtained from wall pressure taps.

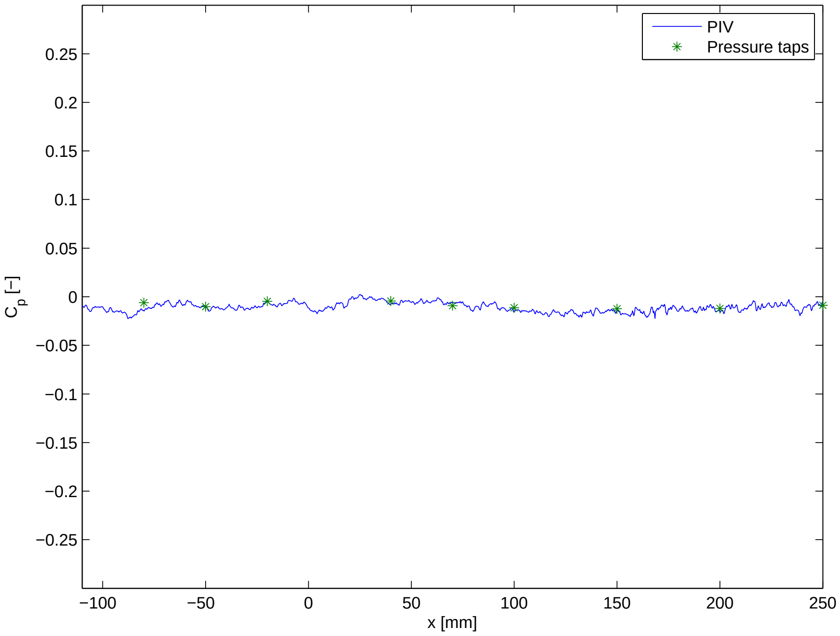

Figure 5.23: Comparison between the pressure from wall taps and from PIV, for the zero pressure gradient case without suction.

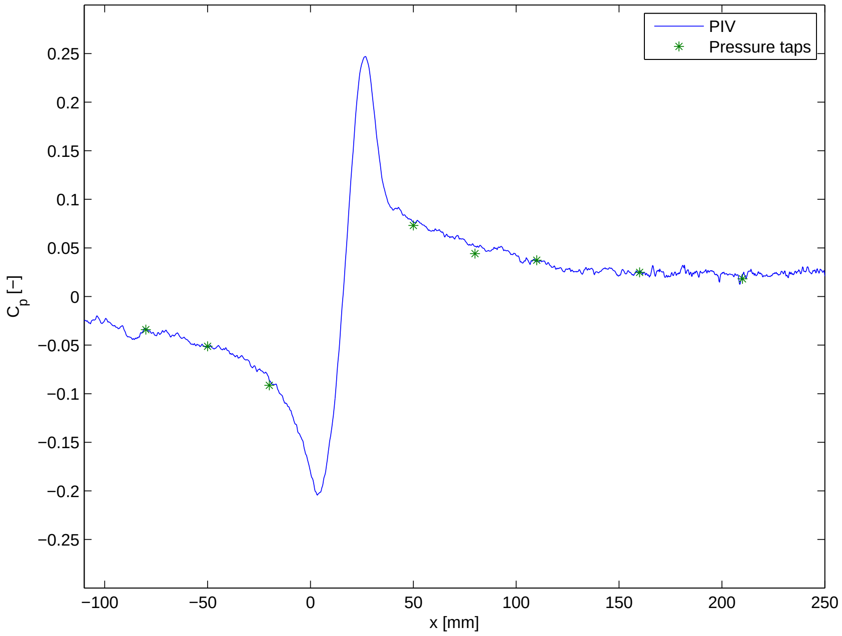

Figure 5.24: Comparison between the pressure from wall taps and from PIV, for the zero pressure gradient case with suction, $\sigma = 0.7$.

indeed be seen that in the region above the slot, an adverse pressure gradient is present. If one compares this with figure 2.7, it can be observed that for this region there is also good qualitative correspondence with the data from Park et al.

Note that the pressure above the slot for both the current results and the results from Park et al., is not actually the wall pressure. It is the pressure over the straight line where the wall would have been if there were no slot.

To further investigate the effect of suction on the pressure distribution, figure 5.25 shows the entire pressure field obtained from PIV for the case with suction at $\sigma = 0.7$. From this, one can observe a region of low pressure when approaching the slot, followed by a region of high pressure near the rear edge of the slot. The high pressure zone is formed around the stagnation point (see figure 5.20), where the pressure reaches its maximum. The low pressure region is formed around the minimum pressure point near the leading edge of the slot, due to the acceleration of the flow.

As already stated in section 2.2.1, due to the high wall-normal velocities, the boundary layer approximations in equation 2.6 are not valid for the case of slot suction. From the pressure pattern in figure 5.25 it can indeed be observed, that one of the results of these boundary layer approximations, $\frac{\partial p}{\partial y} \approx 0$, is not valid in the region near the slot. This, once again, points out that common design tools, which solve the boundary layer equations, cannot be used for predicting the effects of slot suction.

From the results in this section, it can be concluded that the measured influence on the pressure distribution matches the findings from literature. Furthermore it has been shown that the pressure obtained from PIV shows very good correspondence with the pressure, measured from the wall taps. In section 5.2.1 it was already shown that the influence of the corner vortices on the two-dimensionality of the flow field is not higher than 1% in terms of continuity. Apparently, this influence is also not large enough to significantly affect the pressure obtained through solving the Poisson equation.

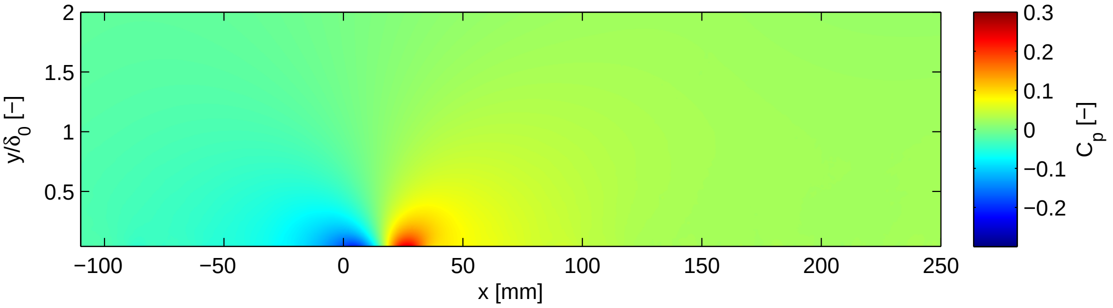

Figure 5.25: Pressure field obtained from PIV for the zero pressure gradient case with suction, $\sigma = 0.7$.

5.2.4 Effect of Suction on the Integral Parameters

In order to further investigate the effects of suction on the boundary layer, this section discusses the results for the streamwise development of the integral parameters. More specifically the effect on the momentum thickness and the shape factor is shown and compared with the results found by Park et al. and Antonia et al.

Let us start with the influence of suction on the development of the momentum thickness, θ. Figure 5.26 shows the streamwise development of this parameter for different suction cases together with the flat plate case.

From this figure it can be observed that when applying suction, the momentum thickness is reduced downstream of the slot, as compared to the reference case. Logically, the decrease in momentum thickness becomes higher for an increasing amount of suction. A relatively low suction coefficient of $\sigma = 0.2$, already gives a reduction of approximately 8 % as compared to the flat plate boundary layer, for a given position behind the slot.

It can be observed in figure 5.27, that apart from a reduction in both the momentum thickness and the displacement thickness, the ratio between the two, the shape factor, also reduces. The suction, as explained in section 2.2.1, causes the velocity profile to become 'fuller'. It seems that behind the slot, when the local influence of the slot is diminished, both H and θ show the same trend, but at a reduced value. That is, for $x \geq 200$ [mm], the lines in figures 5.26 and 5.27 are approximately parallel.

Now, let us focus on the region surrounding the slot. From the streamwise development of θ (and H) a typical pattern can be observed. When approaching the slot, θ, decreases and reaches a minimum near $x = 0$ [mm]. Then, across the slot, θ increases, reaching a maximum at the end of the slot's rear edge, near $x = 30$ [mm]. Finally a rapid decrease occurs, after which the streamwise development becomes similar to the reference case, but at a reduced value of θ. It should be kept in mind that for the region $0 \leq x \leq 30$ [mm], the boundary layer parameters are evaluated as if there was a porous strip (similar to Park et al. [29]). That is, the streamwise velocity was set to zero at the virtual line at $y = 0$ [mm]. Although the streamwise velocity is actually not zero, the resulting integral parameters do give a good indication of the local effects.

The pattern described above, matches the pattern obtained by Park et al. for the streamwise development of Re_θ, which was already shown in figure 2.8. Note that it is possible to compare the results for θ with results for Re_θ because they are approximately proportional. The Reynolds number is a function of the momentum thickness, θ, the freestream velocity, U_∞, and the constant kinematic viscosity, ν. In section 5.2.2 it was shown that behind the slot, there is a small reduction in freestream velocity, due to the application of suction. The relative reduction in freestream

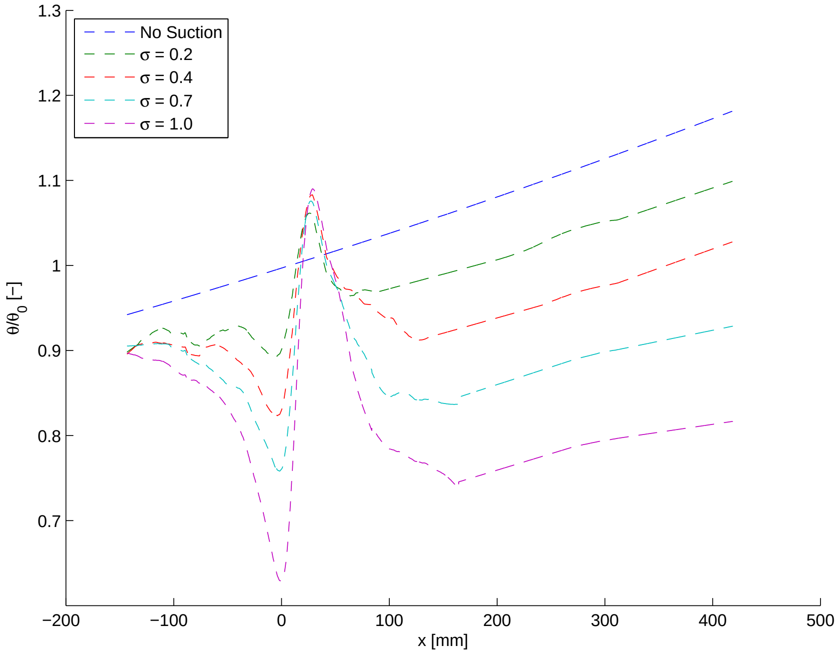

Figure 5.26: Streamwise development of the momentum thickness for the zero pressure gradient case with suction. Smoothing: -120 ≤ x ≤ 100: Sgolay(1,50), 100 ≤ x ≤ 420: Sgolay(1,800).

velocity, however, is much smaller than the relative reduction in θ. It can therefore be assumed constant, which results in $\mathrm{Re}_\theta \propto \theta$.

To understand the typical pattern for θ, figure 5.28 shows the velocity profile at four characteristic locations: a location in front of and rearward of the slot, and the locations of both extrema. It can be seen that moving from x = -100 [mm] to x = 0 [mm] the velocity profile becomes much fuller. This can be explained by the local increase in near-wall velocity, due to the addition of two flow patterns, already described in figure 5.20. Then, directly after the slot at x = 30 [mm], the near-wall velocity is reduced, causing the peak in momentum thickness. Downstream of this point, the velocity profile becomes fuller again, due to the favourable pressure gradient, as can be seen from the profile at x = 150 [mm].

In section 2.2.2 it was already described that Park et al. report that both H and Re_θ, show a weak non-linearity with respect to σ (for $0.1 \leq \sigma \leq 0.45$). For higher suction rates ($2.6 \leq \sigma \leq 6.5$), where relaminarisation effects occurred, Antonia et al., show a linear decrease for Re_θ and a non-linear increase of H with respect to σ.

As a final comparison between the current results and the ones reported in literature, the relation between σ and the parameters, Re_θ and H has been obtained. For both parameters, the average ratio of the result with and without suction has been obtained for the region $250 \leq x \leq 400$ [mm]. In this region, the local influences due to the slot are not present anymore.

Figure 5.29 shows this result for Re_θ. Note that the error bars represent the standard deviation from the average ratio found in the region $250 \leq x \leq 400$ [mm]. Before calculating the ratio and the corresponding standard deviation, the results have been smoothed (Sgolay(1,20)) in order to remove the high spatial frequency measurement noise.

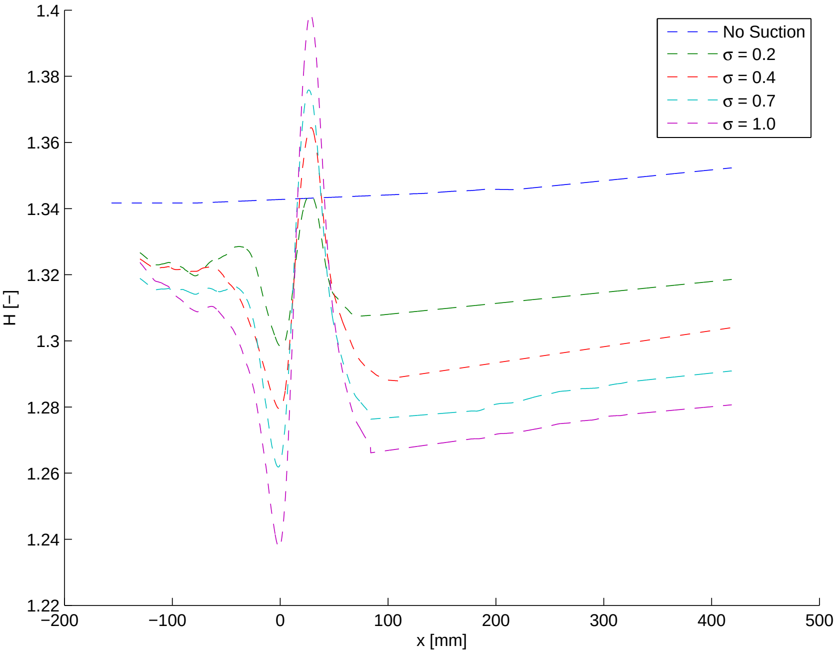

Figure 5.27: Streamwise development of the shape factor for the zero pressure gradient case with suction. Smoothing: -120 ≤ x ≤ 100: Sgolay(1,50), 100 ≤ x ≤ 420: Sgolay(1,800).

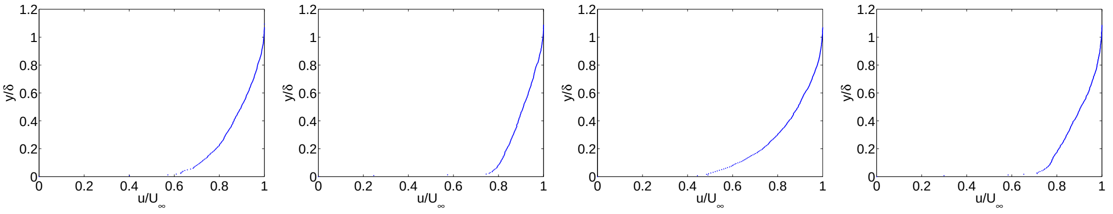

(a) x =-100 mm (b) x = 0 mm (c) x = 30 mm (d) x = 150 mm

Figure 5.28: Boundary layer velocity profiles at different positions before and after the slot, with suction, σ =0.7.

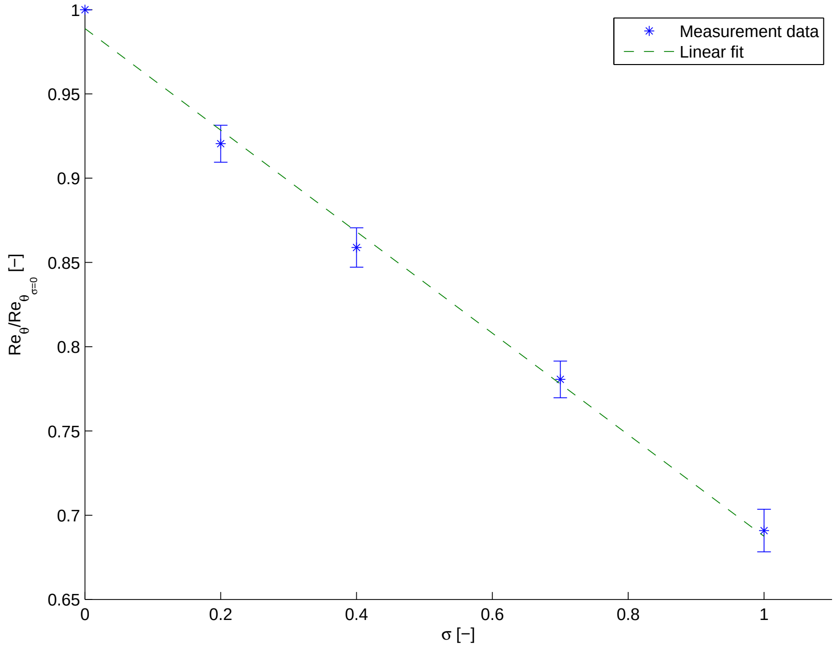

Figure 5.29: Ratio $\mathrm{Re}_\theta/\mathrm{Re}_{\theta_{\sigma=0}}$ as a function of the suction coefficient, σ, for the zero pressure gradient case. Averaged values for $250 \leq x \leq 400$.

It can be observed from figure 5.29 that the reduction in Re_θ with respect to the original boundary layer is approximately linear. This observation matches with the observations by Antonia et al, who also reported this linear relationship. However, taking into account the uncertainties in the measurements, the results could also be fitted with a weak non-linear curve. Especially when only the results for $\sigma \leq 0.4$ are taken into account. It is for this range of suction coefficients that Park et al. report the weak non-linearity in the relation between σ and θ.

From figure 2.8, it has been graphically deduced that for $\sigma = 0.45$, Park et al. find a ratio of $\mathrm{Re}_{\theta_\sigma}/\mathrm{Re}_{\theta_{\sigma=0}} = 0.81$. For the current experiment, this ratio (according to the linear fit) is found to be 0.85. Possibly, this difference is caused by the difference in Reynolds number for the two investigations. However, it is not evident that the two investigations can be compared, quantitatively, in this way. To clarify this, further research towards the influence of Reynolds number should be conducted.

Finally, figure 5.30 shows the average shape factor ratio $H_\sigma/H_{\sigma=0}$. The shape factor clearly shows a non-linear decrease with respect to σ, which qualitatively matches with the observation from Park et al. The relative reduction in shape factor, is much less than for the momentum thickness. For $\sigma = 1.0$, the momentum thickness is reduced by 32 %, whereas the shape factor is decreased by only 5 %.

Concluding, in this section it has been found that the results for the integral parameters, θ and H, show a good match with literature. Close to the slot, a typical pattern in the development for θ and H is found. Downstream of the slot, where the local effects are diminished, the rate of growth of these parameters seems to be independent of the suction coefficient. For this location behind the slot, a linear, or possible slightly non-linear, relation is found for the decrease in Re_θ with respect to σ. The shape factor clearly shows a non-linear decrease with respect to σ.

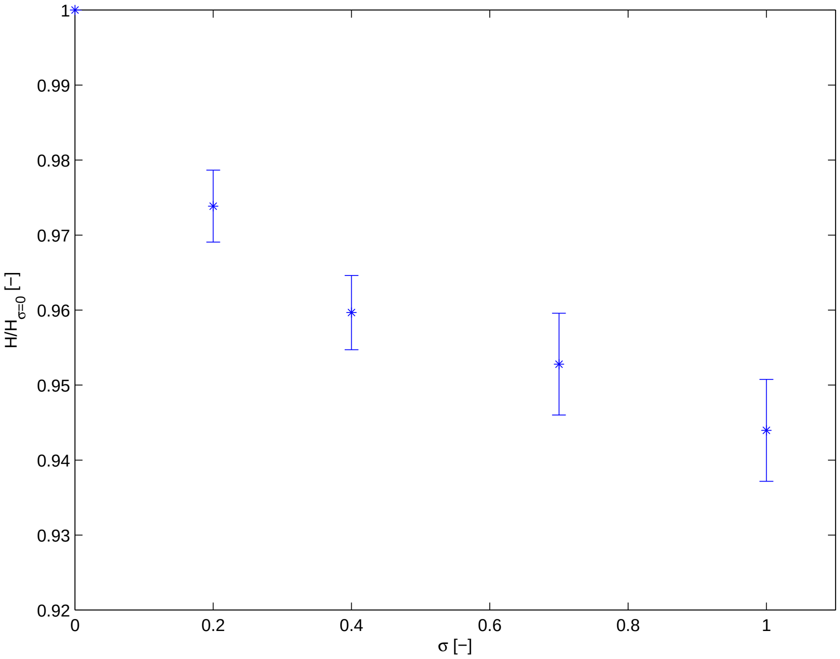

Figure 5.30: Ratio $H/H_{\sigma=0}$ as a function of the suction coefficient, σ, for the zero pressure gradient case. Averaged values for $250 \leq x \leq 400$.

5.3 Slot Suction with an Adverse Pressure Gradient

This section presents the results for the measurements with an adverse pressure gradient, for $\frac{dp}{dx} \approx 200$ [Pa/m]. In the previous section, the main phenomena due to suction have already been explained. Furthermore, the results were compared with the available literature on slot suction for a zero pressure gradient turbulent boundary layer. As far as the author is aware of, no literature has been published, on a similar investigation for a turbulent boundary layer experiencing an adverse pressure gradient. Therefore, the results in this section will be compared to the ones obtained for the zero pressure gradient problem. Any differences and similarities will be discussed and, if possible, explained.

5.3.1 Measurement without Suction

Again, before presenting the results with suction, the reference measurement for the case without suction is discussed first. Figure 5.31 shows the development of θ for the boundary layer without suction. Similarly as for the zero pressure gradient case, the rate of growth calculated from the momentum balance is also depicted. First of all, it can be observed that the increase in θ over the domain is much larger than for the zero pressure gradient case. Whereas the zero pressure gradient case showed an increase of approximately 1.2 [mm], the current results show an increase of approximately 6.5 [mm] over the domain. These values correspond to an increase of 23 % and 112 % respectively. The higher rate of change of momentum thickness is obviously the result of the adverse pressure gradient, as can be seen from the integral momentum relation in equation 2.9.

Similar as for the zero pressure gradient case, it can also be seen that the rate of growth of the momentum thickness is higher than the one obtained from the momentum balance. The relative difference between the two, is however much lower. Whereas the measured growth was

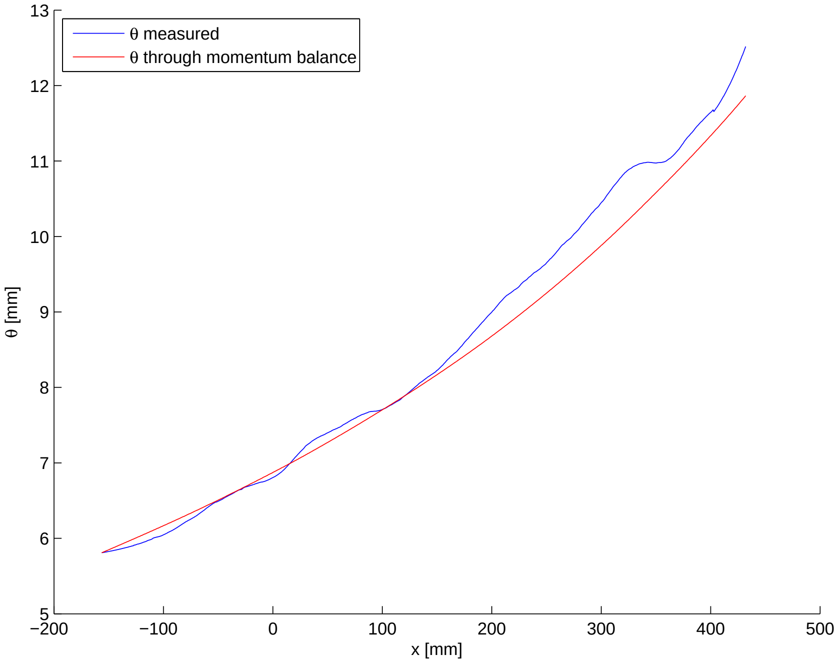

Figure 5.31: Streamwise development of the momentum thickness for the adverse pressure gradient case without suction. Smoothing: Sgolay(1,100).

approximately 90% higher for the zero pressure gradient, it is only in the order of 8 % for the current case. On the other hand, the absolute difference is in the order of $\theta \approx 0.5$ [mm] for both cases. The additional increase in momentum thickness therefore seems to be relatively independent of the pressure gradient.

Furthermore, it can be observed from figure 5.31, that the hump near x = 320 [mm] is still visible. However, its amplitude relative to the total change in θ over the domain, is much less. Next to that, the hump near x = -100 [mm] is no longer visible. Finally, it can be noted that the momentum thickness at x = 0 [mm], is equal to $\theta_0 = 6.9$ [mm]. For a freestream velocity of 26.2 [m/s] at the location of the slot, this resulted in a Reynolds number of $\mathrm{Re}_{\theta_0} \approx 11{,}600$. The boundary layer thickness at x = 0 [mm] was found to be $\delta \approx 55$ [mm]. The resulting slot width for the measurements with suction was therefore set equal to 11 [mm] based on the dimensionless slot width of $\frac{W}{\delta_0} = 0.2$.

In order to confirm that the velocity profile also matches the logarithmic law for the adverse pressure gradient case, figure 5.32 shows the fit for velocity profiles at two different positions within the domain (i.e. x = -50 [mm] and x = 250 [mm]). It can be observed that for the adverse pressure gradient, the logarithmic law still nicely fits the velocity profile. The RMS error for this fit is in the same order of magnitude as for the zero pressure gradient case (see table 5.6). Furthermore, the velocity profile shows a larger wake component due to the presence of the adverse pressure gradient.

Similarly as for the zero pressure gradient boundary layer case, this fit has also been made using Coles' law of the wake. From figure 5.33, one can observe that the match between the measured profile and Coles' law of the wake is also quite good. However a slight deviation between the fit and the upper part of the measured velocity profiles can be observed. This deviation is larger for the profile further downstream, at x = 250 [mm], which is reflected by the higher RMS error (see table 5.6). Furthermore, the wake component, Π, is now found to be increasing from 0.5 at the beginning of the domain to approximately 2.5 at the end of the domain. For the specific profiles

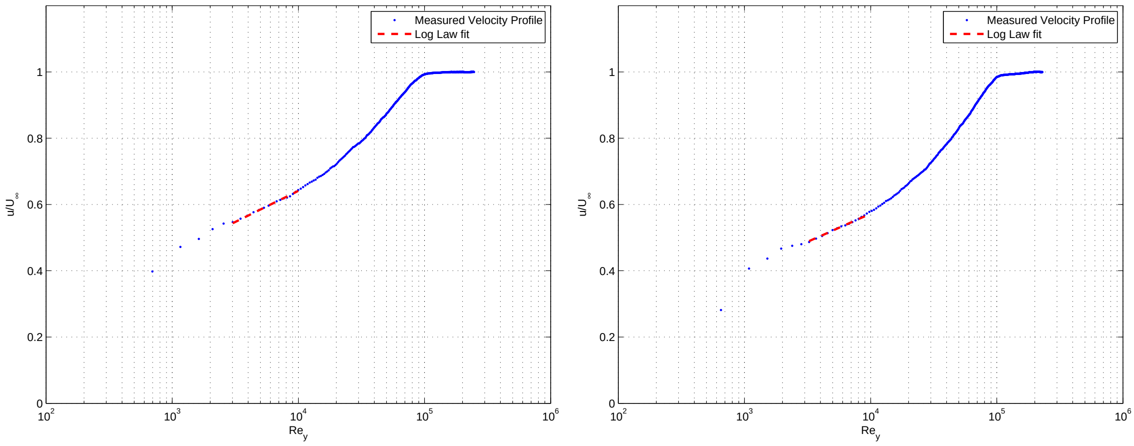

(a) x = -50 mm (b) x = 250 mm

Figure 5.32: Fit of the logarithmic law for two velocity profiles at different streamwise locations for the adverse pressure gradient case without suction.

in figure 5.33, the characteristic values for the fitted data are summarised in table 5.6.

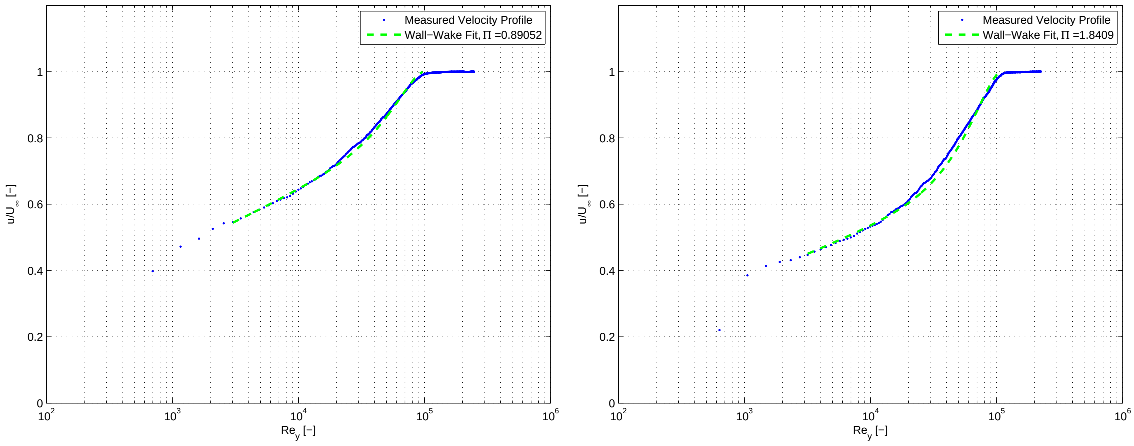

(a) x = -50 mm (b) x = 250 mm

Figure 5.33: Fit of Coles' law of the wake for two velocity profiles at different streamwise locations for the adverse pressure gradient case without suction.

Figure 5.34 shows the friction coefficient obtained through the Clauser technique together with the one obtained from the correlation from White (equation 2.19). It can be seen that at the beginning of the domain, the match between the two is very good. However, moving further in x-direction a difference can be observed between the correlation from White and the Clauser approximation. At the end of the domain, the deviation between the two typically has a value of $0.1 \cdot 10^{-3}$, corresponding to approximately 7 %.

As mentioned before, the correlation from White has an approximate accuracy of ± 3%. However, this accuracy is valid for predicting the friction coefficient of a boundary layer having a velocity profile described by Coles' law of the wake. From figure 5.33 and table 5.6, it was seen that

	x = -50 [mm]	x = 250 [mm]
C_f (Clauser) [-]	0.00224	0.00156
RMS error log law fit [-]	0.0020	0.0028
Π (Coles) [-]	0.891	1.841
RMS error Coles fit [-]	0.0085	0.0156

Table 5.6: Results for the log law fit and Coles' wall of the wake fit at x = -50 [mm] and x = 250 [mm] for the adverse pressure gradient case without suction.

for the velocity profile near the end of the domain, the RMS deviation between the measured profile and the fit from Coles' law of the wake is nearly twice the RMS deviation for the profile at the beginning of the domain. This difference in velocity profile is likely to be the cause for the difference in the obtained friction coefficient in figure 5.34.

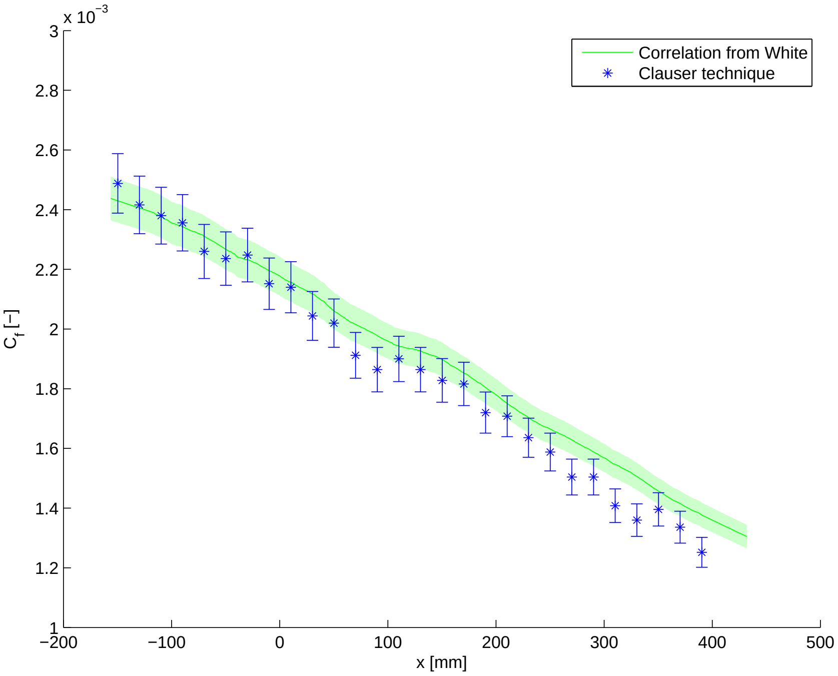

Figure 5.34: Friction coefficient obtained through Clauser technique compared with theoretical friction coefficient from White, for the adverse pressure gradient case.

Finally, for this case it was also checked whether the two-dimensional continuity equation holds. Similarly to the zero pressure gradient case, a deviation of 1% was found in the domain for -50 ≤ x ≤ 250 [mm](see table 5.7). For the smaller domain (i.e. 0 ≤ x ≤ 150 [mm]), in this case the deviation was found to be even smaller than 0.01 % of the total inflow (see table 5.8).

Concluding, analogous to the zero pressure gradient results, it has been confirmed that the velocity profile of the boundary layer for the adverse pressure gradient has the characteristics of a two-dimensional velocity profile. As expected, the adverse pressure gradient causes an increased growth of the momentum thickness, a higher decrease in the friction coefficient and a larger wake component in the velocity profile.

Boundary [mm]	2-D ‘volume flow’ [m^2/s]
x = -50	-3.1173
x = 250	2.7062
y = 120	0.4434

Table 5.7: Calculated two-dimensional ‘volume flows’ to check for continuity for -50 ≤ x ≤ 250 [mm] for the adverse pressure gradient case.

Boundary [mm]	2-D ‘volume flow’ [m^2/s]
x = -50	-3.0552
x = 250	2.8319
y = 120	0.2235

Table 5.8: Calculated two-dimensional ‘volume flows’ to check for continuity for 0 ≤ x ≤ 150 [mm] for the adverse pressure gradient case.

5.3.2 Effect of Suction on the Pressure Distribution

This section shows whether the effect of suction on the pressure distribution is altered due to the presence of an adverse pressure gradient. As mentioned earlier, the adverse pressure gradient is created by a diverging channel, which resulted in an approximately constant adverse pressure gradient of $\frac{dp}{dx} \approx 200$ [Pa/m].

The pressure gradient can be non-dimensionalised, using equation 2.22, to obtain the corresponding Clauser pressure parameter. It has been calculated that this parameter increases from β = 1.7 at x = -100 [mm] to β = 9 at x = 400 [mm]. Comparing this with the typical values for the AF-0901 airfoil, presented in section 2.4, the pressure gradient for the current experiment is still an order of magnitude lower than for the typical engineering problem, in which suction is applied to prevent turbulent boundary layer separation.

Using the current experimental setup, it was not possible to create higher adverse pressure gradients. Another option to reach a higher adverse pressure gradient would be to use, for example, a wall mounted hump. However, this would complicate the experimental setup and increase the possibility of having a reduced quality of the flow field. Therefore it has been deliberately decided, to use the more simple setup at the expense of a reduced adverse pressure gradient.

In addition to β, another dimensionless pressure gradient parameter can be calculated by inserting δ instead of δ^* into equation 2.22. It is found that this parameter increases from ξ = 10 to ξ = 36 for the same streamwise positions as above. According to White [45], this already corresponds to a mild to strong adverse pressure gradient.

Figure 5.35 shows the effect of suction on the wall pressure for the adverse pressure gradient case. For the case without suction, it can indeed be observed that the pressure coefficient rises approximately linearly in the streamwise direction. Despite the adverse pressure gradient, the application of suction results in the same trends as for the zero pressure gradient case. Relative to the reference case without suction, a more favourable (or less adverse) pressure gradient is observed, both in front of- and behind the slot.

To compare the effect of suction on the wall pressure, with and without the presence of an adverse pressure gradient, let us consider figure 5.36. Here, the difference in pressure coefficient with respect to the case without suction, $C_{p_\sigma} - C_{p_{\sigma=0}}$ is depicted for both cases.

It can be seen that the effect of suction on the local wall pressure, relative to the reference case, is similar for both cases. For the ‘low’ suction coefficients (σ = 0.2-0.4) there is a very good correspondence between the two cases, while for the higher coefficients (σ = 0.7-1.0) only small differences can be observed. The overall RMS obtained for the difference between the results

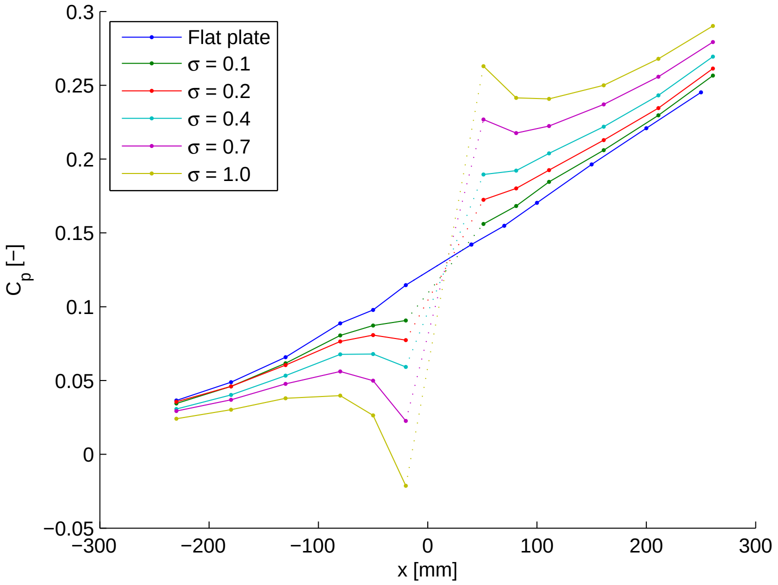

Figure 5.35: Streamwise development of the wall pressure coefficient due to the application of suction. Pressure obtained from wall pressure taps.

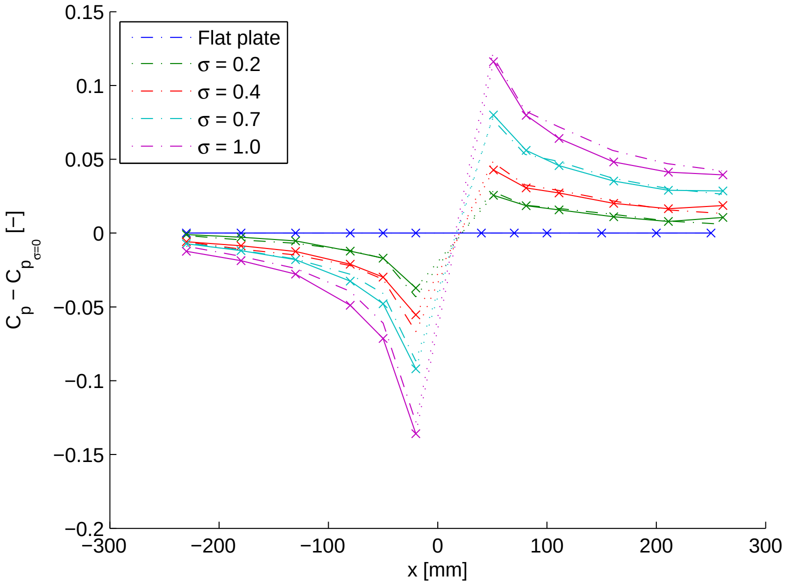

Figure 5.36: Effect of suction on the wall pressure for the zero pressure gradient case (· -) and the adverse pressure gradient case (x-).

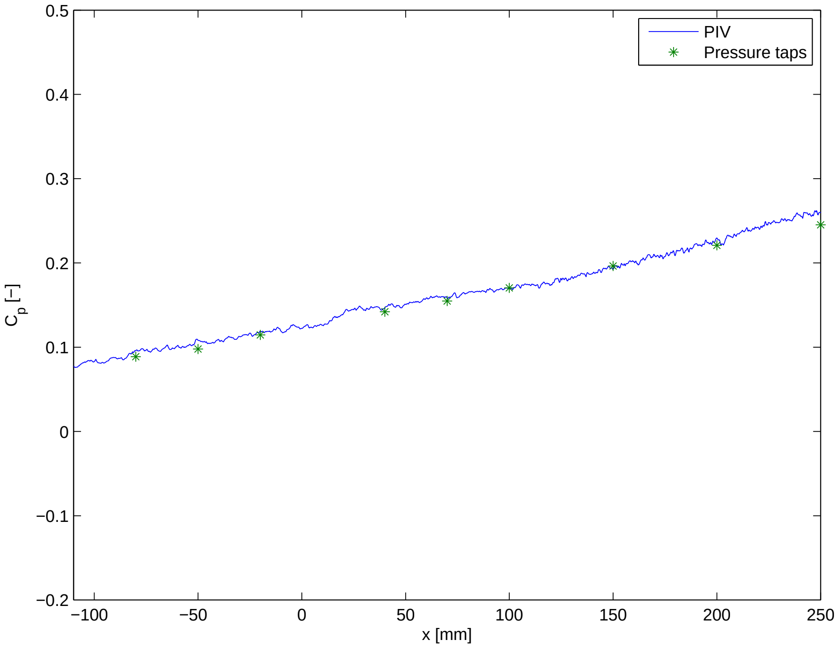

Figure 5.37: Comparison between the pressure from wall taps and from PIV, for the adverse pressure gradient case without suction.

for zero and adverse pressure gradient case is found to be 0.0044. From these results, the local influence of slot suction on the wall pressure, seems to be relatively independent of the external pressure gradient.

For the adverse pressure gradient case, the pressure field has also been obtained from the PIV measurements. Figure 5.37 compares the pressure at the lower boundary of the domain with the data obtained from the pressure taps. Similar to the zero pressure gradient, a very good correspondence between the two datasets is found.

Analogously to the previous section, 5.38 shows the wall pressure distribution from the PIV measurements for the case with suction, $\sigma = 0.7$. If one compares this with the same result for the zero pressure gradient boundary layer, in figure 5.24, the same behaviour is observed. The adverse pressure gradient does not change the fact that a stagnation point is present with a high pressure region surrounding it. Similarly, the low pressure region due to the flow acceleration over the front edge of the slot is also present.

As a final result for the pressure for slot suction, figure 5.39 shows the entire pressure field for suction with $\sigma = 0.7$. From the figure it can be seen that the pressure field shows similar behaviour to the zero pressure gradient case. When the pressure, in the case of no suction is subtracted, the similarity with the zero pressure gradient results become even more clear. This can be observed by comparing figure 5.40 with figure 5.25.

From the above, it can be concluded that, for the current value of $\frac{dp}{dx}$, the disturbance in the pressure field, due to suction, is similar to that for a zero pressure gradient boundary layer. Furthermore, it was also shown that with the presence of this adverse pressure gradients, the correspondence between the pressure from PIV and the pressure from the wall taps was very good.

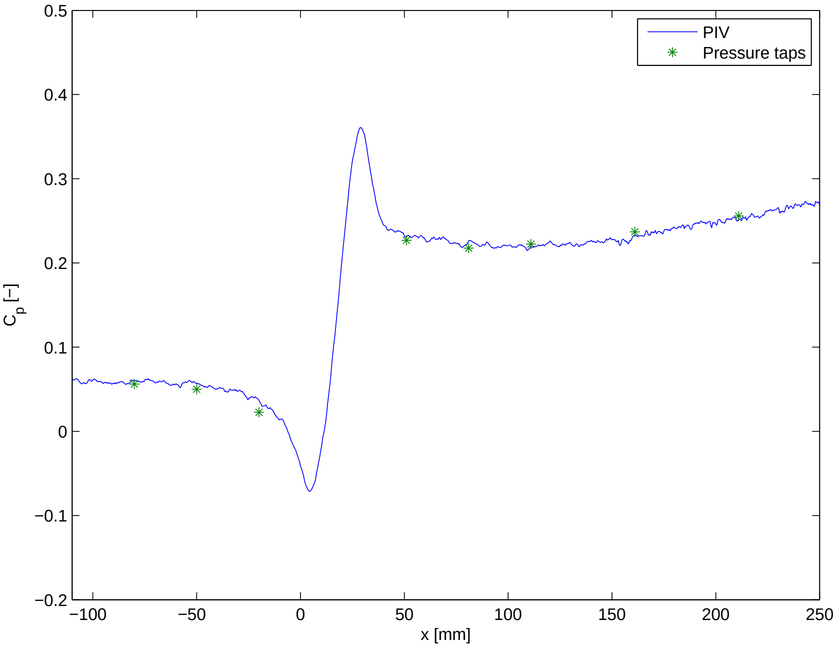

Figure 5.38: Comparison between the pressure from wall taps and from PIV, for the adverse pressure gradient case with suction, $\sigma = 0.7$.

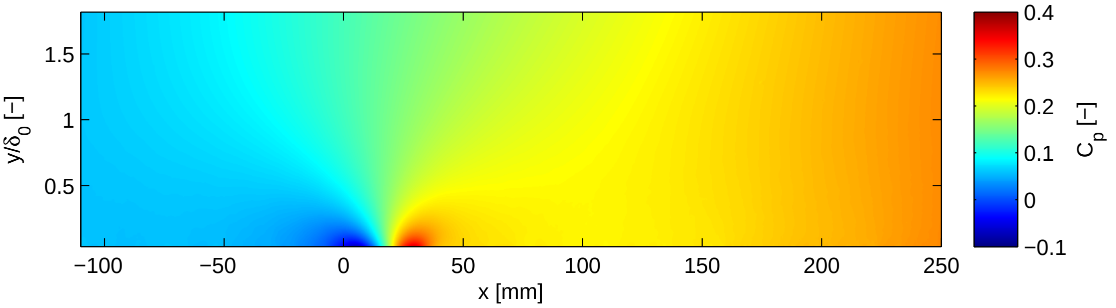

Figure 5.39: Pressure field obtained from PIV velocity field with suction, $\sigma = 0.7$.

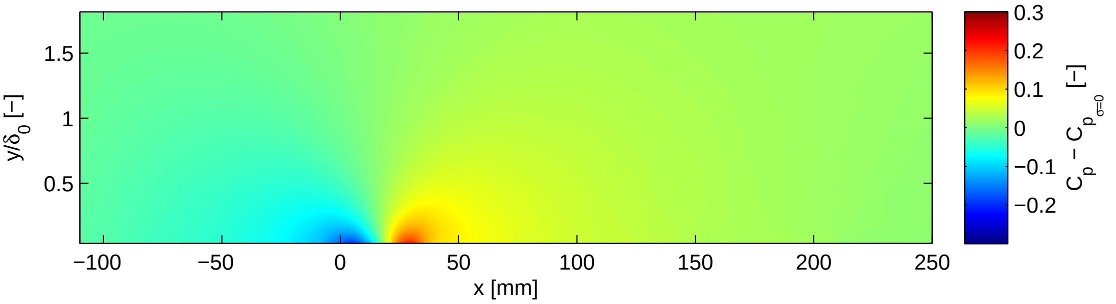

Figure 5.40: Differential pressure field obtained from PIV velocity field for the adverse pressure gradient case with suction, $\sigma = 0.7$.

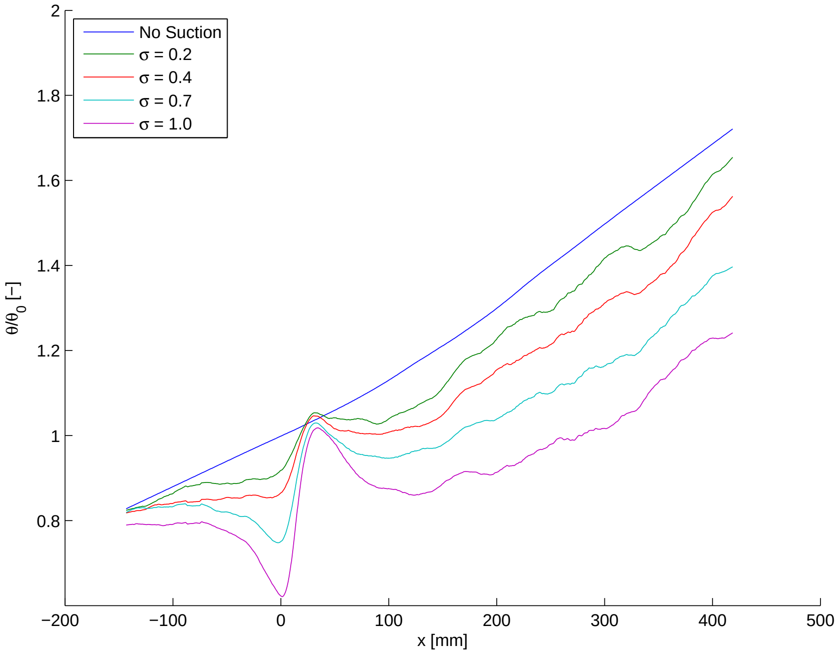

Figure 5.41: Streamwise development of the momentum thickness, for the adverse pressure gradient case. Smoothing: 'No suction' = Sgolay(2,800), other results = Sgolay(1,50).

5.3.3 Effect of Suction on the Integral Parameters

This section aims to demonstrate if the effect of suction, on the integral parameters, is also independent of the external pressure gradient. To do so, again, let us consider the streamwise development of the momentum thickness and the shape factor for the different suction coefficients. Figure 5.41 shows the streamwise development of the momentum thickness, while figure 5.42 shows the streamwise development of the shape factor.

In section 5.3.1 the increased growth of the momentum thickness due to the presence of the adverse pressure gradient was already discussed. Figure 5.42 also shows a streamwise increase in shape factor, typical for a boundary layer experiencing an adverse pressure gradient. Similarly to the zero pressure gradient case, the application of suction results in a reduction of both θ and H as compared to the reference case. The streamwise pattern also shows the same qualitative behaviour, which was explained by the velocity profiles in figure 5.28.

To further compare the effects of an adverse pressure gradient, let us consider the reduction in Re_θ, with respect to the reference case, again averaged over the region $250 \leq x \leq 400$ [mm]. From figure 5.43, it can be observed that the relation between $\mathrm{Re}_\theta/\mathrm{Re}_{\theta_{\sigma=0}}$ and σ is linear, similar to the zero pressure gradient case. Furthermore, the actual reduction in Re_θ is also equal to the zero pressure gradient case. For both cases, $\sigma = 1.0$ results in a reduction of approximately 32 % in Re_θ.

Now, as a final comparison between the adverse pressure gradient case and the zero pressure gradient case, consider the effect of suction on the shape factor. From figure 5.44 the same non-linear trend as for the zero pressure gradient case can be observed. However, the reduction in shape factor is larger than for the zero pressure gradient case. For $\sigma = 1.0$, the reduction with respect to the original shape factor is found to be 13 %, while for the zero pressure gradient case this is only 5 %. For the case with an adverse pressure gradient, the suction is therefore more effective in changing the shape of the velocity profile.

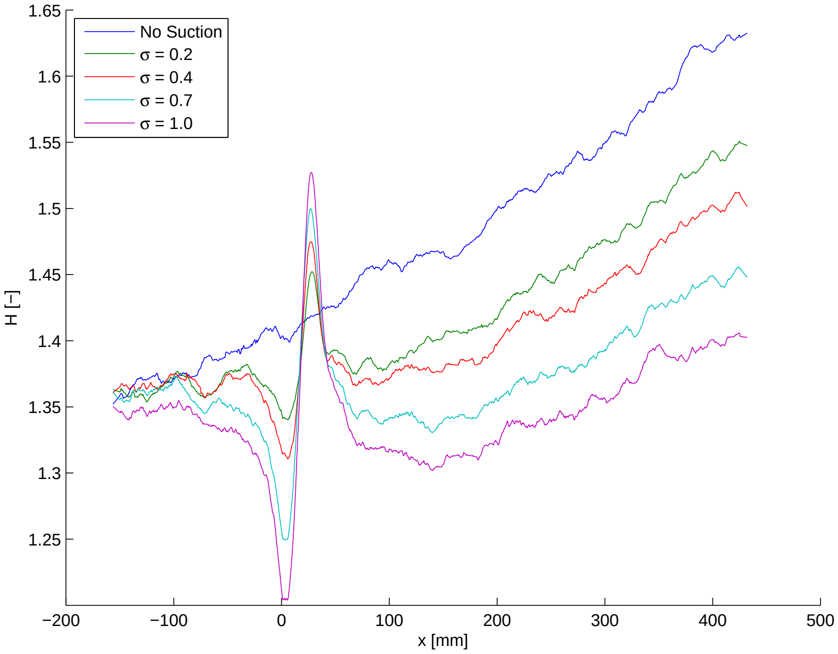

Figure 5.42: Streamwise development of the shape factor for the adverse pressure gradient case. Smoothing: Sgolay(1,50).

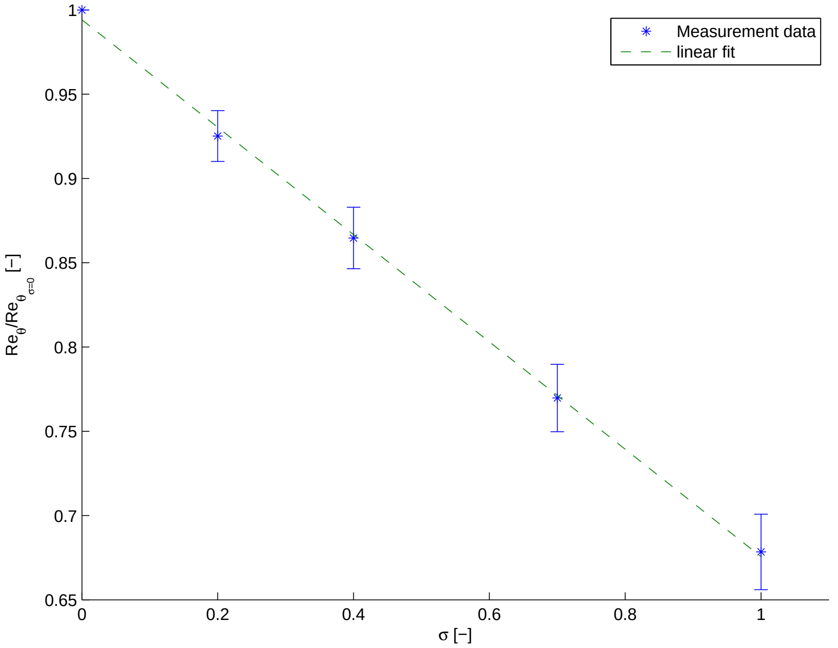

Figure 5.43: Ratio Re_θ/Re_{θ_0} as a function of the suction coefficient, σ, for the adverse pressure gradient case. Averaged values for $250 \leq x \leq 400$.

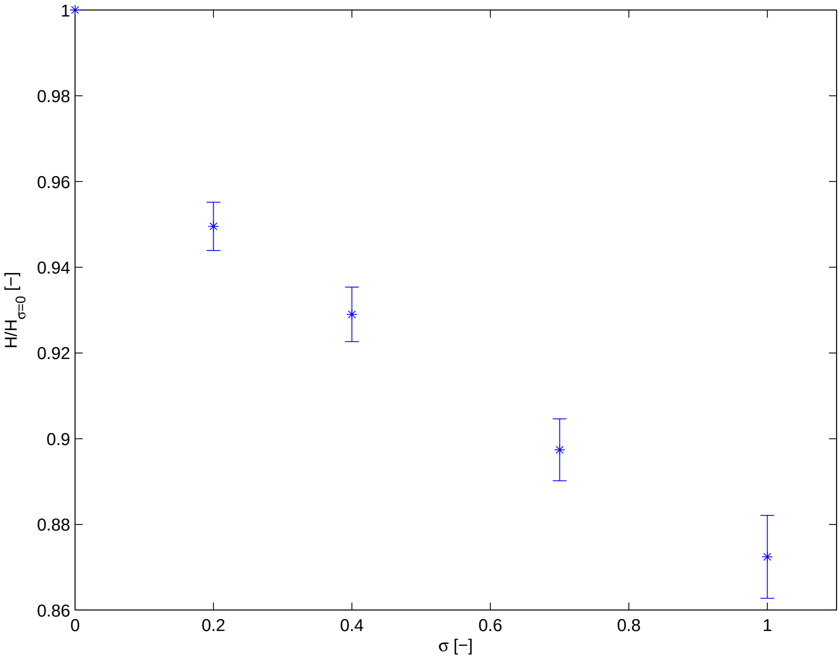

Figure 5.44: Ratio H/H_0 as a function of the suction coefficient, σ, for the adverse pressure gradient case. Averaged values for $250 \leq x \leq 400$.

It should be noted that for the zero pressure gradient case, $\sigma = 1.0$ represents a lower actual mass flow than for the adverse pressure gradient. To compare for the same mass flow, the value of $\sigma = 0.85$, should be considered for the adverse pressure gradient case. However, for this value the reduction in shape factor is still higher than for the zero pressure gradient case with $\sigma = 1.0$.

The most likely explanation for this discrepancy, is the difference in shape of the undisturbed boundary layer at the location of the slot. Comparing figures 5.27 and 5.42, it can be seen that the shape factor for the zero pressure gradient case at $x = 0$ [mm], equals $H_0 \approx 1.34$, while for the adverse pressure gradient case, it is found to be, $H_0 \approx 1.41$.

In their investigation towards slot suction on a zero pressure gradient turbulent boundary layer, Oyewola et al. [28] also identify the initial value of H_0 to be affecting the 'effectiveness' of suction. More precisely, in their comparison with the work from Antonia et al. [2], it is found that for a boundary layer with a higher initial shape factor, a lower suction coefficient, σ, was needed to reach the same effects. This matches the observation from the current experiment.

To explain how a higher initial shape factor might result in a higher decrease in shape factor for a given suction coefficient, σ, let us return to the theory in section 2.1.1. More specifically, consider figures 2.1 and 2.2. from figure 2.1 it can be seen that the difference in θ and δ^* increases when moving from the boundary layer edge to the wall. Especially the low velocity points near the wall, contribute more to the value of δ^* than θ.

Now, assume that suction is represented by simply removing the near-wall part of the boundary layer. One can imagine, that by doing so, the value of δ^* is, relatively, reduced more than the value of θ. This is indeed reflected by the fact that the shape factor decreases when applying suction.

Now consider a boundary layer with a higher initial shape factor, and thus more low velocity points near the wall (see figure 2.2). For this case, one can imagine that removing the lower part of the boundary layer has more effect on δ^* than for the boundary layer with a low shape factor.

The effect for θ will also increase, but relative to δ^* this effect will be lower. Although this is a simplified analysis, the author believes that it shows that a higher initial shape factor can indeed cause a higher reduction in shape factor for a given suction rate.

Summarising, it is found that the influence of the adverse pressure gradient is only visible in the reduction in shape factor. The effect on the pressure distribution is similar to that for the zero pressure gradient case. Furthermore, the decrease in momentum thickness is also the same, both qualitatively and quantitatively. It appears that the higher reduction in shape factor can be explained by the different initial condition of the unperturbed boundary layer. Further research could help to better understand the relation between the initial shape of the boundary layer and the effectiveness of suction in altering this shape. The outcomes of such research might help finding the most 'effective' way of applying suction.

5.4 Slot Suction Compared with Distributed Suction

In chapter 1, the envisioned application of boundary layer suction to wind turbine blades was defined as part of the motivation for the current research. More specifically, boundary layer suction through a slot was introduced as an alternative option to distributed boundary layer suction through a porous medium. One of the research goals that stemmed from this background problem, was to describe the effects of slot suction relative to distributed suction.

In order to do so, suction through a porous plastic and a perforated plate, have been investigated in the same experimental setup and for the same adverse pressure gradient as described in section 5.3. This section presents the results for distributed boundary layer suction and compares them with the results for slot suction.

5.4.1 Measurement without Suction

Before comparing the different suction methods, the results for the zero suction cases are presented first. As mentioned in section 3.2.1, for all three inserts (slot, porous plastic and perforated plate) a reference measurement has been performed. Since the experimental setup had to be partially rearranged, these measurements were done to check the repeatability of the zero suction measurement.

Figures 5.45 and 5.46 show the streamwise development of the momentum thickness and the shape factor respectively, for all three setups. From these it can be observed that the trends for these three data sets are close to each other, but do not exactly coincide. While the reference measurements for both distributed suction inserts are nearly on top of each other, the reference measurement for the slot insert is slightly below the others. The mean deviation for θ is found to be in the order of 2 % while for H this is approximately 0.5 %. The rearrangement of the setup to be able to fit the new insert is very likely to be the cause of these deviations. Although the observed differences in the reference measurements are not very large, they will be taken into account during the interpretation of the following results. Furthermore, note that in this section, the same reference values for θ_0 and δ_0 are used, as defined in section 5.3.1.

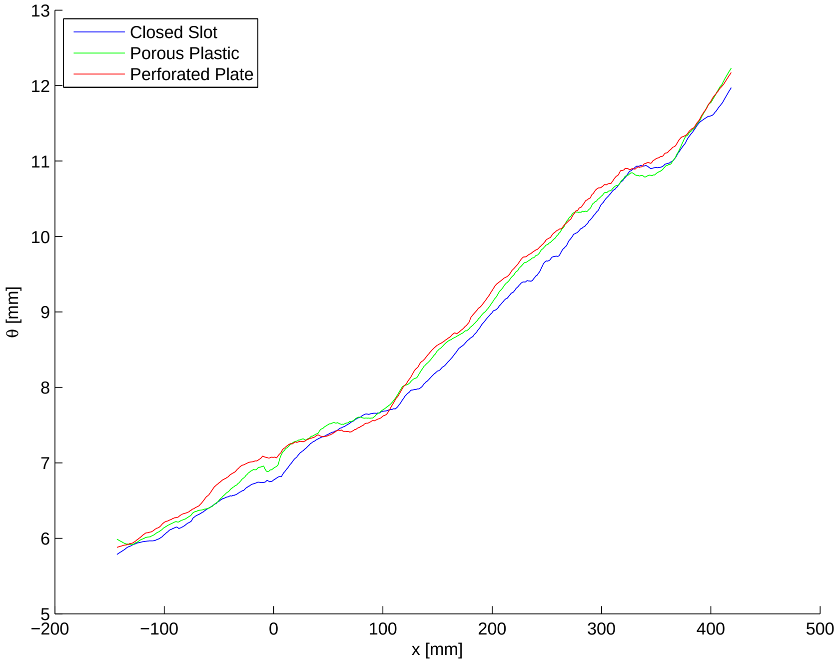

Figure 5.45: Streamwise development of the momentum thickness, for three suction setups, for the adverse pressure gradient case without suction.

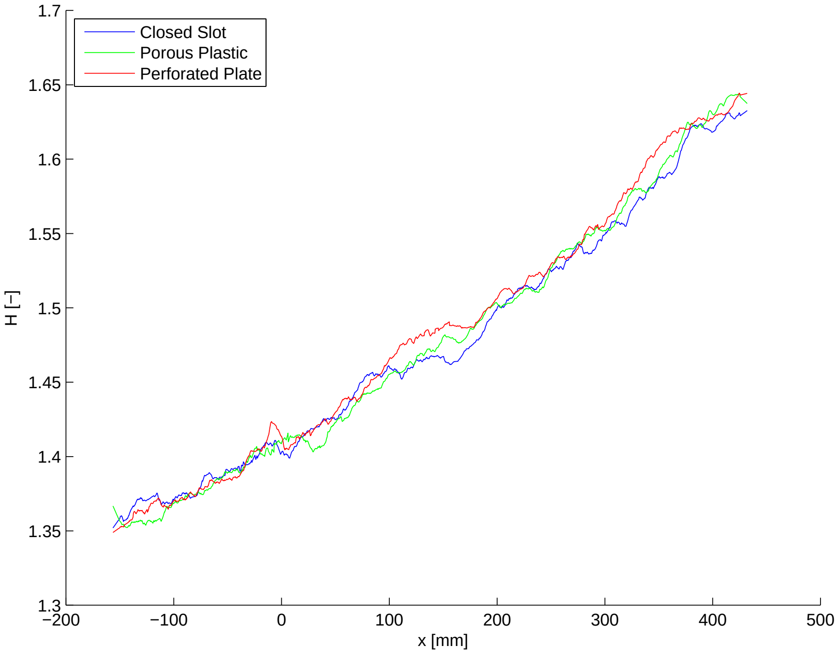

Figure 5.46: Streamwise development of the shape factor, for three suction setups, for the adverse pressure gradient case without suction.

5.4.2 Flow Pattern due to Suction

This section aims to show the differences and similarities in the qualitative flow pattern, due to the application of either localised or distributed suction. The region of suction for the perforated plate and the porous plastic corresponds to $0 \leq x \leq 100$ [mm], while the slot including the rounded edges extends over $0 \leq x \leq 31$ [mm].

Figures 5.47, 5.48 and 5.49 show the differences between the streamwise velocity field obtained at $\sigma = 0.7$ and the case without suction. These figures correspond to suction trough the slot, the porous plastic and the perforated plate, respectively. From both velocity fields for distributed suction (figures 5.48 and 5.49), it can be observed that there is no region near the wall, where the flow is decelerated with respect to the reference case. Earlier, it has already been explained how this region of deceleration, which is present for the case of slot suction, might actually cause separation. Therefore, when boundary layer suction is used to prevent separation, this difference between localised and distributed suction is important to take into account.

Furthermore, the velocity fields for the distributed suction cases show general similarity. Both show a region of acceleration in front of the suction region. It appears that the region of acceleration in front of the suction region is slightly larger for the porous plastic. Possibly this is due to the air flowing through the overlap parts with which the porous plastic was mounted to the insert. (see figure 3.5). Next to that, it can be seen that at the region of distributed suction, the near-wall velocity is increased due to the transpiration for both cases.

Finally, for all three cases it can be observed that behind the region of suction, there is a clear increase in velocity in the boundary layer, indicating a decrease for the integral parameters, θ and δ^*. It appears that near the end of the domain, this velocity increase is similar for the three suction cases. Section 5.4.4 will elaborate on this in more detail, in terms of the integral parameters.

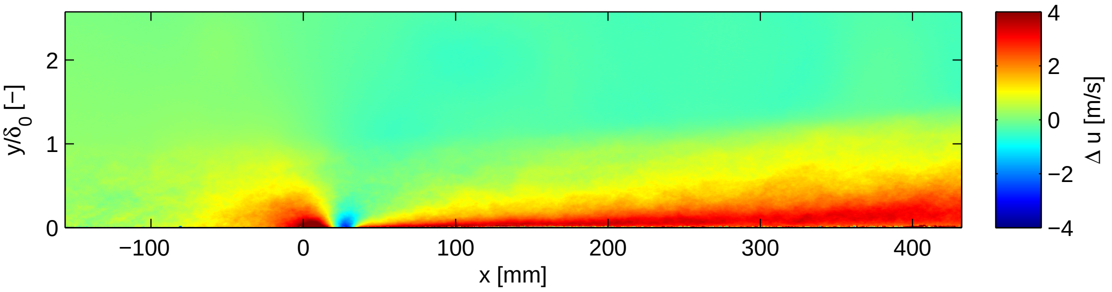

Figure 5.47: Difference in streamwise velocity for the adverse pressure gradient case without suction and with suction through a slot, $\sigma = 0.7$.

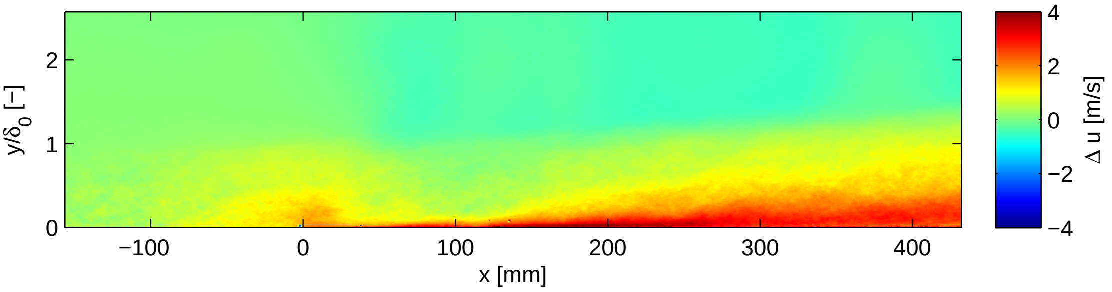

Figure 5.48: Difference in streamwise velocity for the adverse pressure gradient case without suction and with suction through a porous plastic, $\sigma = 0.7$.

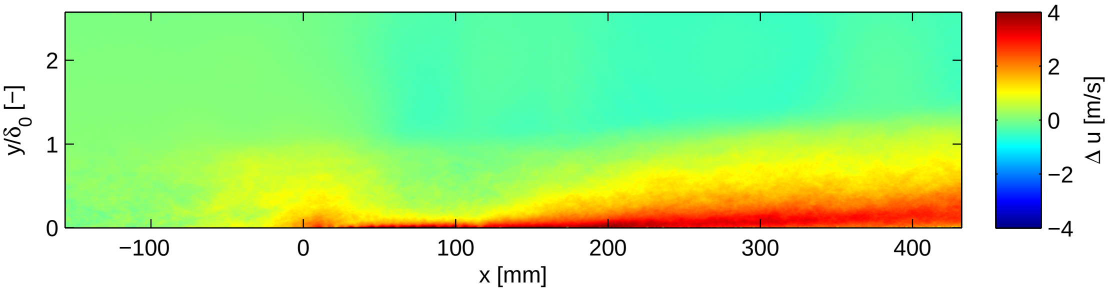

Figure 5.49: Difference in streamwise velocity for the adverse pressure gradient case without suction and with suction through a perforated plate, $\sigma = 0.7$.

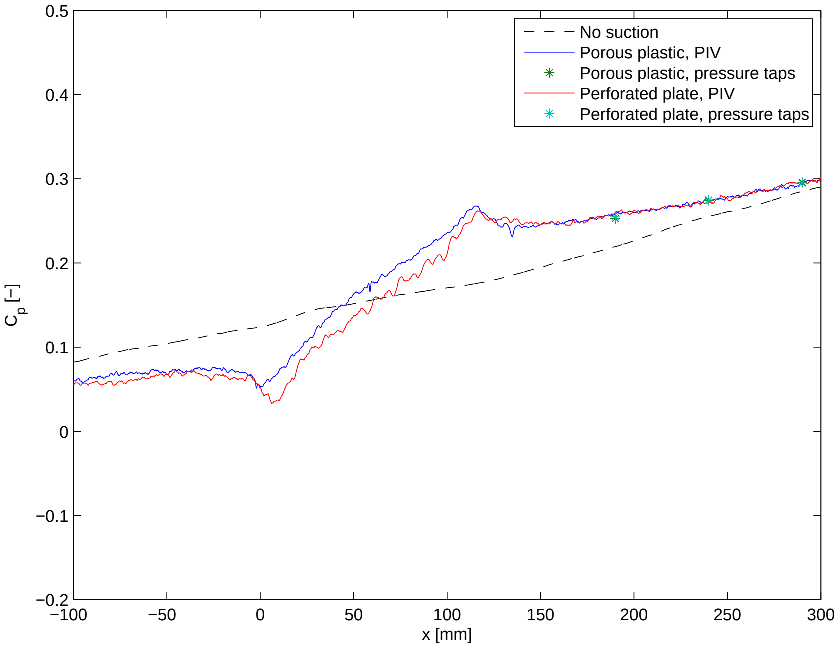

Figure 5.50: Comparison between the pressure from wall taps and from PIV for the adverse pressure gradient case with distributed suction through a porous plastic and a perforated plate, $\sigma = 0.7$.

5.4.3 Effect of Suction on the Pressure Distribution

Due to the use of new inserts for distributed suction, six of the twelve pressure taps, described in section 3.5, were not available anymore. For the evaluation of the pressure distribution, therefore, the pressure deduced from the velocity field has to be used. Fortunately, until now, this technique has been shown to give results, which correspond to the data from the pressure taps very well.

Figure 5.50 shows the wall pressure distribution obtained for the case of suction through the porous plastic and the perforated plate, for $\sigma = 0.7$. It can be observed that the data coincides with the data from the available pressure taps. Furthermore, it can be seen that the pressure coefficient rises stronger in the region of suction, in an approximate linear fashion. Just like for the case of slot suction, one can observe a (small) region with a more favourable pressure gradient, in front of and rearward of the suction zone. The pattern is therefore similar to the one of slot suction, but with a much lower 'amplitude'. Obviously, this is directly related to the lower suction velocity. For $\sigma = 0.7$, the suction velocity for localised and distributed suction through the porous plastic corresponds to $V_w = 11.7$ [m/s] and $V_w \approx 1.29$ [m/s] respectively.

When comparing the results for both distributed suction cases, it can be seen that the point of minimum pressure is located somewhat more upstream for the porous plastic. This is probably due to the overlap region where the porous plastic was mounted to the insert. In the previous section this effect was also observed in the effect on the streamwise velocity. Due to this effect there is also a small offset between the two results, which vanishes when the end of the suction region is reached.

For $\sigma = 0.7$, the suction velocity for distributed suction is approximately 5 % of the freestream velocity. According to theory (see section 2.2.1) the boundary layer equations are still not valid for these suction velocities. The suction might therefore still considered to be slightly localised. Now, for $\sigma = 0.2$, the suction velocity through the porous plastic is approximately 0.37 [m/s],

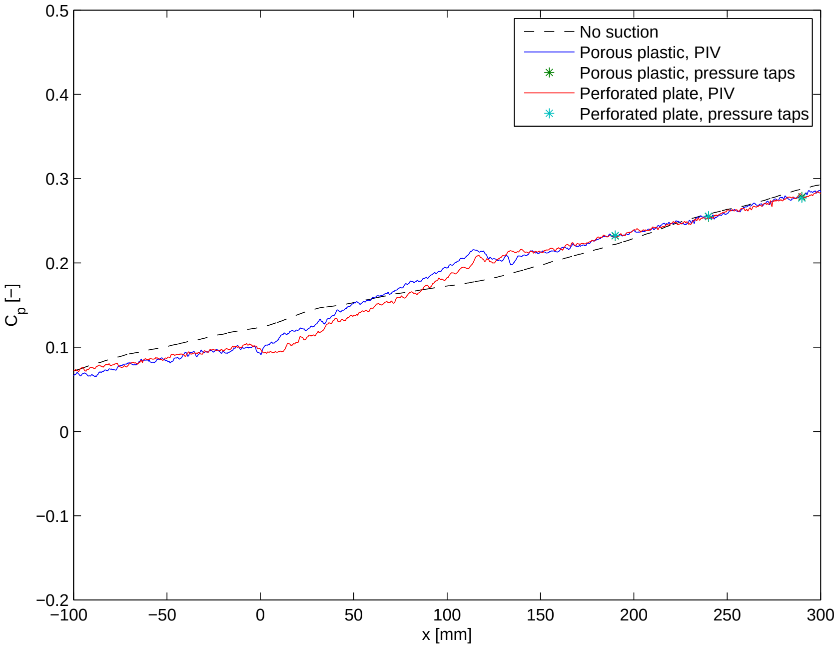

Figure 5.51: Comparison between the pressure from wall taps and from PIV for the adverse pressure gradient case with distributed suction through a porous plastic and a perforated plate, $\sigma = 0.2$.

corresponding to 1.5 % of the freestream velocity. From the pressure distributions in figure 5.51 it can now be seen that the 'slot like' pattern has nearly vanished for both distributed suction cases. The pressure rises almost monotonically, except for the small region rearward of the application of suction through the porous plastic.

Figures 5.52 and 5.53, show the entire pressure field for the suction through the porous plastic for both suction rates $\sigma = 0.2$ and $\sigma = 0.7$. Note that for the perforated plate similar results were found. For the lower suction rate, it can be observed. that except for the very small regions near $x = 0$ [mm] and $x = 100$ [mm], the wall-normal pressure gradient is found to be approximately equal to zero (i.e. the pressure contours are approximately vertical). For the higher suction rate, $\sigma = 0.7$, it can clearly be seen that at the same locations, the wall-normal pressure gradient is much higher and that for a much larger region it cannot be assumed equal to zero. This again indicates that for the lower suction rate the boundary layer equations are approximately valid, while for the higher suction rates they are certainly not.

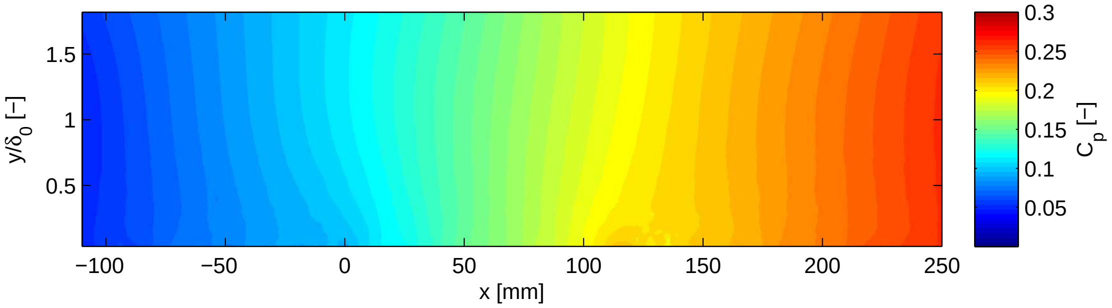

Figure 5.52: Pressure field obtained from PIV velocity field for distributed suction through porous plastic, $\sigma = 0.2$.

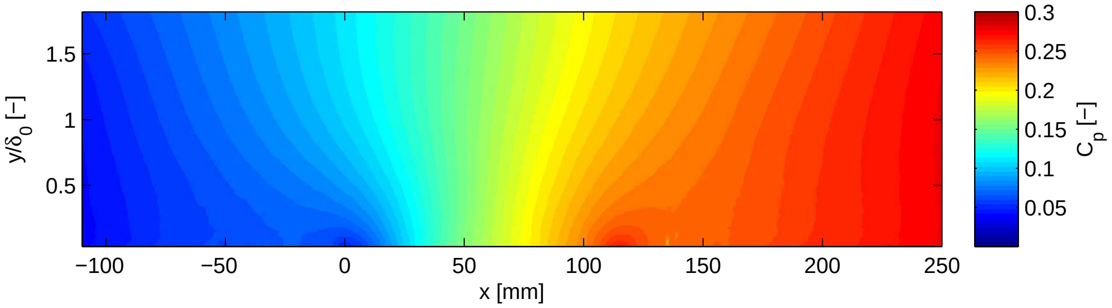

Figure 5.53: Pressure field obtained from PIV velocity field for distributed suction through porous plastic, $\sigma = 0.7$.

5.4.4 Effect of Suction on the Integral Parameters

Until now, it has been observed that there are both similarities and differences between localised and distributed suction, in terms of the general flow field and the pressure distribution. Logically, the most distinct differences were observed in the region close to the location of suction. This section elaborates on the effects of distributed suction as compared to localised suction, with respect to the integral parameters.

Again, let us compare the different suction media for the relatively low coefficient of $\sigma = 0.2$ and the relatively high coefficient of $\sigma = 0.7$. Figure 5.54 and 5.55 show the streamwise development of the momentum thickness and the shape factor for these suction coefficients.

For these parameters, just as for the flow pattern and the pressure distribution, the most distinctive differences between the results for distributed suction and slot suction can be observed in the region where suction is applied. For the slot suction one can see a very strong local effect already upstream of the slot, while for distributed suction these effects are much less. As the suction velocities are much lower for the distributed cases, this is exactly what one would expect.

For $\sigma = 0.7$, it can be seen that the development for θ and H due to distributed suction, shows a similar, but much more gradual, pattern as compared to the development of these parameters due to slot suction. That is, the rate of change of H and θ show a decrease upstream and downstream of the suction region as compared to the reference case. Above the suction region, both the shape factor and the momentum thickness show an increase. This resemblance in pattern is very likely due to the suction velocity still being relatively high. This observation was also found for the

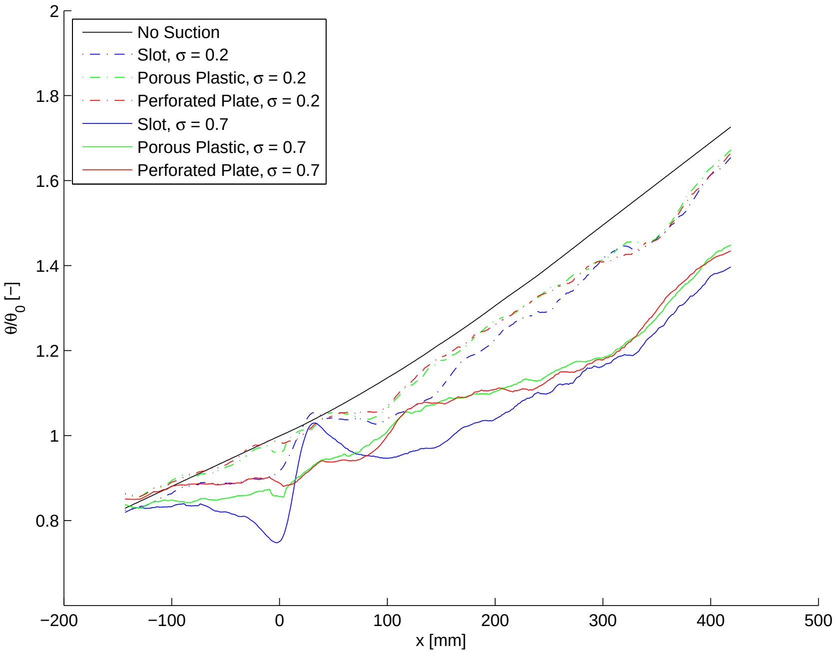

Figure 5.54: Streamwise development of the momentum thickness for the three suction setups with suction. Smoothing: No suction = Sgolay(1,800), Distributed suction = Sgolay(1,100), Slot suction = Sgolay(1,50).

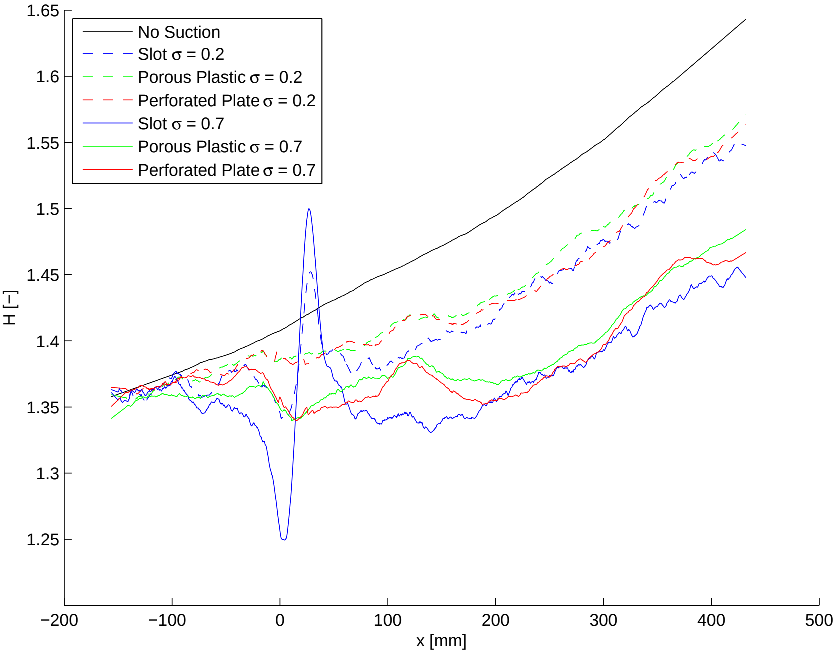

Figure 5.55: Streamwise development of the shape factor for the three suction setups with suction. Smoothing: No suction = Sgolay(1,800), Distributed suction = Sgolay(1,100), Slot suction = Sgolay(1,50).

streamwise development of the wall pressure in the previous section. Finally it can be observed that the effect of suction through the porous plastic is somewhat stronger in front of the suction zone as compared to the suction through the perforated plate. This again is deemed to be an effect of the flow crossing through the overlap part with which the porous plastic is mounted to the insert.

The results for distributed suction at $\sigma = 0.2$, show a much smoother development of H and θ. It can be seen from figure 5.54, that for the largest part of the porous zone ($20 \leq x \leq 100$ [mm]), θ does not increase. Furthermore, the shape factor does not show the typical minimum and maximum in front of- and behind the suction zone respectively. Based on the previous, it seems that the results for $\sigma = 0.2$ are more representative for actual distributed suction, while the results for $\sigma = 0.7$, also show characteristics typical for localised suction.

Despite all the local differences discussed above, it can be observed that, well downstream of the slot (i.e. $x \geq 250$ [mm]), the results for distributed suction and slot suction are very close to each other. It appears that the obtained values for the case of slot suction are slightly below the ones for distributed suction. However, this trend was already visible in the reference measurements without suction, in figures 5.45 and 5.46. The maximum deviation between the results can be seen in the region near $x = 350$ [mm], and was found to be approximately 3 % and 2 % for the momentum thickness and shape factor respectively. Taking into account these differences, together with the general measurement uncertainty (which is increased in this region due to the lens effects), it can be concluded that for the current experiment, the differences between suction through a porous medium and suction through a slot, are limited to the region close to the location of suction.

This finding is very interesting from an engineering point of view. It implies that the suction 'effectiveness', for changing the velocity profile well downstream of the region of suction, is not dependent on the way through which the fluid is removed from the boundary layer. However, the very strong local effects should be taken into account when suction through a slot is to be used.

Furthermore, when a trade-off is made between the use of either distributed or localised suction, there are other factors to be taken into account. For example, the pressure loss through either a slot or a porous material is very important. Especially in the case of passive suction, reducing this pressure loss is the only way to increase the maximum suction rate. Furthermore, with a porous material or a perforated plate, the porosity and thus the suction distribution can be controlled in both stream and spanwise direction. This can form an important advantage as compared to the use of a slot. Next to these, there are many more considerations in deciding whether to use localised or distributed suction. These are related to, for example, structural strength and manufacturability. The current results provide valuable additional insights, that can assist in selecting the best way of suction.

5.5 Influence of Slot Width

The previous sections have discussed the general results, both in the absence and presence of an adverse pressure gradient. Furthermore, for an adverse pressure gradient, slot suction has been compared with suction through a porous plastic and a perforated plate. The dimensionless slot width used for the previous discussions was equal to $\frac{W}{\delta} = 0.2$.

In order to assess the influence of the slot width on the mean effect of suction, measurements were performed for three different slot widths: $\frac{W}{\delta} = 0.05,\ 0.2,\ 0.5$. It should be noted that these results are obtained from the first measurement campaign. As already described in section 3.2, this campaign did not run flawlessly. Unfortunately, this caused a large part of the data to be of insufficient quality. The data being most reliable has been selected to present here. This corresponds to the results for suction through two slots ($\frac{W}{\delta} = 0.05,\ 0.2$) for the adverse pressure gradient case.

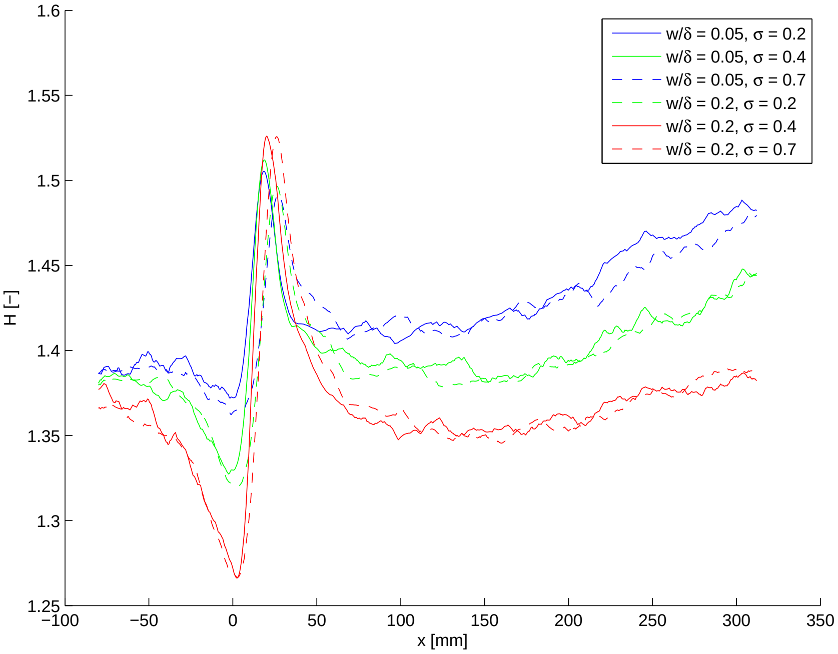

Figure 5.56: Streamwise development of the shape factor for two different slot widths at various suction rates. Smoothing: Sgolay(1,20).

From figures 5.56 and 5.57, it can be observed that for the different suction coefficients, the results for both slot widths are similar. Although there are some slight differences near the slot, the value for θ and H obtained downstream of the slot are very close to each other. Despite the fact that the results are limited to these two figures they do support the earlier findings by Fage et al. and Pierpont et al., stating that the slot width, except locally, has no influence for the mean flow properties for a given value of σ.

Based on these findings on different slot widths as well as the findings from the comparison between distributed and localised suction, it appears that σ is a very 'robust' parameter for describing the effect of suction. Neglecting the local effects, it seems that for the mean flow, the volume of fluid withdrawn from the boundary layer is determining for the reduction in integral parameters.

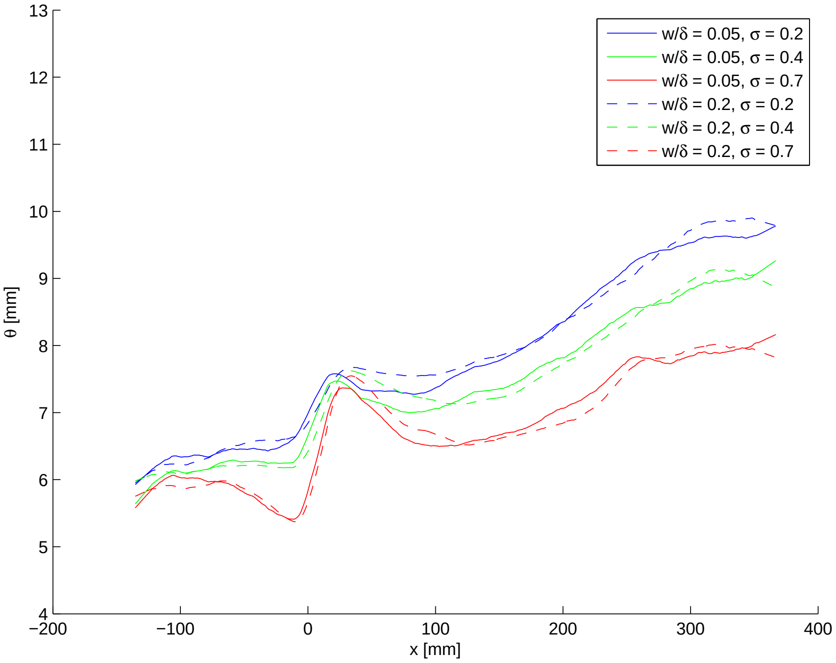

Figure 5.57: Streamwise development for the momentum thickness for two different slot widths at various suction rates. Smoothing: Sgolay(1,50).

5.6 Uncertainty Analysis

For the interpretation of any experimental result, it is important to, at least, have some idea on the uncertainty of the results. First of all, if the uncertainties are unknown, it is not possible to draw definite conclusions from the results. Secondly, if the present data is to be used for validation of numerical methods, it should be known for which range the numerical results are actually validated by this data.

This section presents an uncertainty analysis of the results presented in the previous sections. The first subsection discusses the theoretical uncertainty in the PIV measurement and identifies further causes of uncertainty. The second subsection gives an overall estimate of the uncertainty for the integral parameters.

5.6.1 Uncertainties in PIV

In order to estimate the measurement uncertainty related to the PIV measurements, let us return to the basics of this method. Some of this has already been explained in section 2.3, but is repeated for convenience.

By tracing the movement of a particle, Δx, between two snapshots, separated by a time interval, Δt, the instantaneous velocity of this particle can be estimated. After all, the velocity is equal to the ratio of displacement and time. The time interval between two images is regulated by a trigger clock of which the uncertainty is assumed negligible. So in order to estimate the uncertainty of the velocity obtained by PIV, one should estimate the uncertainty in the measurement of the particle displacement.

As already explained in section 2.3, the determination of this pixel displacement is accurate on a sub-pixel level, with $\sigma_{px} \approx 0.1$. When assuming that no additional uncertainty is present due to the errors mentioned in section 2.3.3, the measurement uncertainty, σ_u, in the instantaneous velocity can be deduced from equation 5.1.

$$\frac{\sigma_u}{u} = \frac{\sigma_{px}}{\Delta x_{px}} \tag{5.1}$$

Here, Δx_{px} is the pixel displacement of a particle on the camera sensor. Now, for a given velocity and camera setup, this pixel displacement can be increased by increasing the time interval between the two images, Δt. As one can observe from equation 5.1, an increase in pixel displacement, results in a reduced uncertainty in the measured velocity. From this point of view, one would always want to increase the pixel displacement to obtain more accurate results.

However, there are important reasons why the pixel displacement needs to be limited. First of all, if any three-dimensional effects are present, the chance of 'losing' particles between the two images increases with increasing time interval. Furthermore, for a given interrogation window size, velocity gradients combined with a large pixel displacement can cause additional errors. In section 2.3.3 this was already explained for the near-wall region of the turbulent boundary layer.

During the current experiment a time interval of 35 μs was used, which resulted in a pixel displacement of approximately 14 pixels for the freestream velocity of $U_\infty \approx 28$ [m/s]. Using equation 5.1, it can then be calculated that the measurement uncertainty for one instantaneous vector field is, $\sigma_u \approx 0.2$ [m/s].

However, it should be taken into account, that the turbulence within the flow also adds to the uncertainty in the measurement of the mean velocity. That is, if there was no measurement error, each instantaneous velocity result would still deviate from the actual mean. The magnitude of this deviation is dependent on the level of turbulence. For a turbulent boundary layer this level varies, especially in the wall-normal direction.

In order to include the turbulent fluctuations into the estimation for the uncertainty of the mean velocity, the measured RMS error from the mean velocity has been used. This error is obtained from 500 samples and is assumed to be representative for the actual turbulent fluctuations in the velocity field. In section 5.1.3, it was shown that for this sample size, the mean of the velocity fluctuations was converged.

For each vector within an instantaneous velocity field, the combined uncertainty in the measured mean value can now be written as:

$$\sigma_{u_c} = \sqrt{(\sigma_u^2 + \sigma_{turb}^2)}$$

Here, σ_{turb} is assumed to be equal to the obtained RMS error described above.

As said, in order to estimate the mean velocity distribution an average was taken over 500 samples. The uncertainty in determining the mean velocity is thereby reduced and is now estimated by:

$$\sigma_{u_{mean}} = \frac{\sigma_{u_c}}{\sqrt{N}} \tag{5.2}$$

Here, N is the number of samples [40]. For the freestream, where the turbulent fluctuations are lowest, this results in a standard deviation of $\sigma_{u_{mean}} \approx 0.01$ [m/s].

To estimate the uncertainty in the determination of the integral parameters, like θ and δ^*, standard error propagation rules can be applied to the numerical integration procedure. This will now be illustrated for the value of the displacement thickness, δ^*. The equation used to calculate the value of δ^* is given by:

$$\delta^* \approx \sum_{i=0}^{i_e-1} \delta^*_{i+1/2} = \sum_{i=0}^{i_e-1} \left(1 - \left(\frac{\tilde{u}_i + \tilde{u}_{i+1}}{2}\right)\right) \cdot (y_{i+1} - y_i) \tag{5.3}$$

Here, $\tilde{u}$ is the streamwise velocity normalised by the freestream velocity and i_e is the index corresponding to the boundary layer edge coordinate, y_e (see section 4.2).

In order to estimate the uncertainty in the value obtained by equation 5.3, a standard rule for error propagation has been applied [40]. For an arbitrary function f(x, y, z) with independent variables x, y and z, this rule is given in equation 5.4.

$$\sigma_f^2 = \left(\frac{\partial f}{\partial x}\right)^2 \sigma_x^2 + \left(\frac{\partial f}{\partial y}\right)^2 \sigma_y^2 + \left(\frac{\partial f}{\partial z}\right)^2 \sigma_z^2 \tag{5.4}$$

Using this rule it can be found that for each contributing term to the integral of δ^* the error is estimated by:

$$\sigma^2_{\delta^*_{i+1/2}} = \left(\frac{1}{2}\left(y_{i+1} - y_i\right)\right)^2 \cdot \left(\sigma^2_{\tilde{u}_i} + \sigma^2_{\tilde{u}_{i+1}}\right) \tag{5.5}$$

Here $\sigma_{\tilde{u}_i}$, is the standard deviation of the measured normalised mean velocity. This value is the combined value of the uncertainty in the freestream velocity and the velocity at an arbitrary wall-normal position. However, the freestream velocity was determined by averaging 30 velocity points at the top of the boundary layer (see section 4.2.1). Therefore, for this estimation, the uncertainty in the freestream velocity in assumed negligible. This assumption results in the fact that $\sigma_{\tilde{u}_i}$ is approximately equal to $\sigma_{u_{mean_i}}$.

Subsequently, adding up all of the individual values of $\sigma^2_{\delta^*_{i+1/2}}$, obtained through equation 5.5, results in the variance for the measured value of δ^*. Assuming, that the random error follows a normal distribution, this variance can been used to calculate the 95 % confidence interval. For a velocity profile at $x = 30$ [mm], for the zero pressure gradient case without suction, this procedure has been performed. The percentual uncertainty in terms of the 95% confidence interval was found to be ± 0.3 %, for a mean value of $\delta^* = 7.56$ [mm].

Note, that in order to calculate this value, not all data points were included. Since, for the PIV post-processing, a 75 % overlap was used (see section 4.1), every 3 neighbouring points are correlated with each other (see section 2.3.1). Since equation 5.4 can only be used for independent variables, every fourth data point in wall-normal direction is used for the evaluation of equation 5.5.

Now, a quick glance at the unsmoothed results for δ^* in figure 5.58 shows that the high spatial frequency variation around the trend, is clearly higher than the confidence interval calculated above. The random variation seems to be approximately 5 %, which is an order of magnitude higher than the theoretically predicted uncertainty.

It appears that the combined uncertainty due to the PIV measurement uncertainty and the flow turbulence is lower than the actual uncertainty in the results for δ^*. This can be explained by other sources of uncertainty in the determination of the integral parameters not included in the above analysis. First of all, the uncertainty estimation for PIV presented above, is based on the assumption that $\sigma_{px} \approx 0.1$. For example, in the regions where the images were slightly too much out of focus (see section 5.2.1) this assumption is invalid. Also, this analysis does not include errors due to, for example, high velocity gradients within the interrogation windows near the wall.

Additional sources of uncertainty can be found in the determination of the integral parameters, as described in section 4.2. For example, the determination of the wall-normal position of the first measurement point introduces a variation in δ^* and θ across the domain. In section 4.2.2, the error was already described by the RMS error as compared to a fit with Spaldings' law of the wall. However, Spaldings' law of the wall was determined, based on the friction velocity, which in its turn was determined from the measured velocity profile. This means that the calculated uncertainty cannot simply be added to the one calculated above, without taking into account the

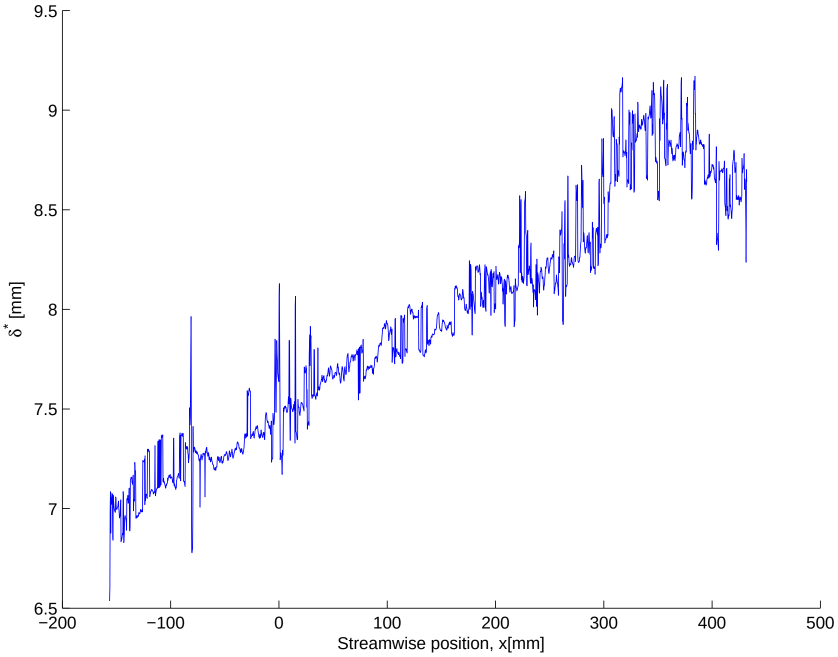

Figure 5.58: Unsmoothed result of the displacement thickness for the zero pressure gradient case without suction.

correlation between these errors. Furthermore, this error is probably not entirely random. That is, it is dependent on the reflection pattern of the laser, which is not by defition random for a given location.

Concluding, it is deemed impossible to use a bottom-up error analysis to determine the confidence interval of the results. The identification of the causes of uncertainty is not very difficult. However, to quantify the contribution of each of these individual causes to the final result, is much harder. The main reason for this, is that the uncertainties, introduced due to some phenomena, and the relation between those, is simply unknown.

Therefore, in order to estimate the uncertainty of the results, another approach is pursued, which will be discussed in the following section.

5.6.2 Estimation of the Uncertainty in the Integral Parameters

This section describes an estimation for the uncertainty in the measured values for the streamwise development of the integral parameters.

Normally, if one wants to estimate the measurement uncertainty for a particular variable, this measurement is repeated a number of times. Based on these measurements a normal distribution is fitted through the observed values, and the standard deviation is determined.

For the current measurement, 500 measurements have been carried out, as was described in the previous section. However, because the flow is unsteady (turbulent), each of these measurements represents a different flow field and all samples are needed to get a good estimate for the mean velocity field. Based on this mean velocity field, the integral parameters are calculated.

Since there is only one result for the mean velocity, there is also only one result for the integral parameters at each streamwise location. In order to apply the method described above, the mean velocity field should have been measured repeatedly, which, unfortunately, is not the case.

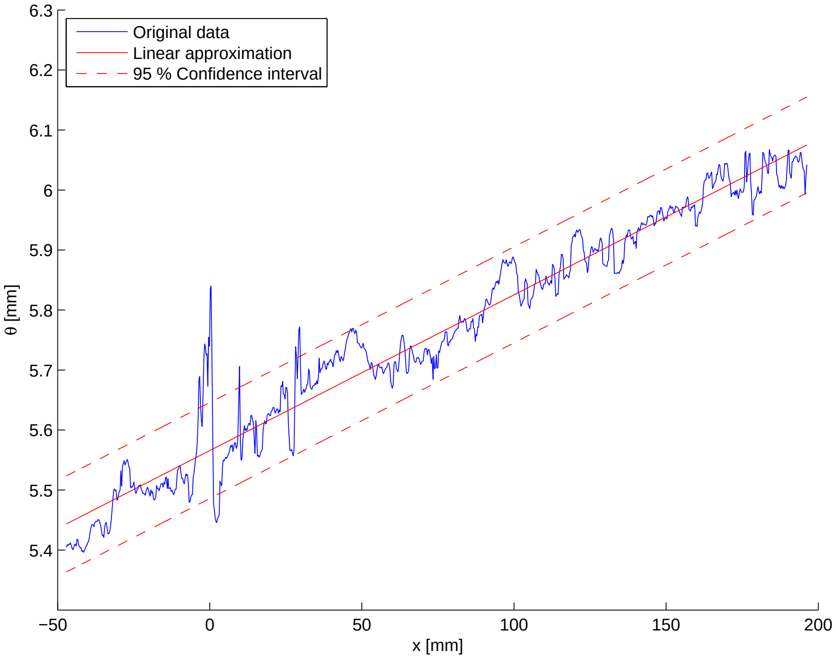

Figure 5.59: Linear approximation for the momentum thickness in the region -50 ≤ x ≤ 200. Result for the zero pressure gradient case without suction.

	Absolute	Relative [%]
H	± 0.02 [-]	± 1.49
θ	± 0.08 [mm]	± 1.38
δ^*	± 0.19 [mm]	± 2.45
Re_θ	± 142.8 [-]	± 1.37

Table 5.9: Estimated 95% confidence intervals for integral parameters.

However, the high frequency spatial fluctuations observed in the results (see figure 5.58) do give some information on the measurement uncertainty within the results. From the physics of the problem of a zero pressure gradient boundary layer, it is known that these fluctuations represent pure measurement noise. To estimate the measurement uncertainty, a linear approximation is made for the results of the integral parameters. It is assumed that the deviations from this linear approximation, are solely due to random measurement noise. Furthermore, it is assumed that these deviations are normally distributed. The region for linear approximation is chosen to be -50 ≤ x ≤ 200 [mm], to avoid influence of the bias errors due to lens distortions, described earlier. Figure 5.59 shows this linear approximation for θ.

Figure 5.60 now shows an histogram of the measured deviations from the linear approximation, together with a fitted normal distribution. It can be observed that these deviations are indeed approximately normally distributed, as was one of the assumptions for this method. Furthermore, for the same reason as explained above, the histogram only contains the error from the linear trend for each fourth point in streamwise direction. From this fit of the normal distribution, the corresponding value for σ_θ has been determined for the momentum thickness. This procedure has been carried out for the other integral parameters, and has resulted in the 95 % confidence intervals presented in table 5.9. In figure 5.59 the confidence interval for θ is also depicted.

It should be taken into account that the estimated uncertainties in table 5.9 may not be exactly

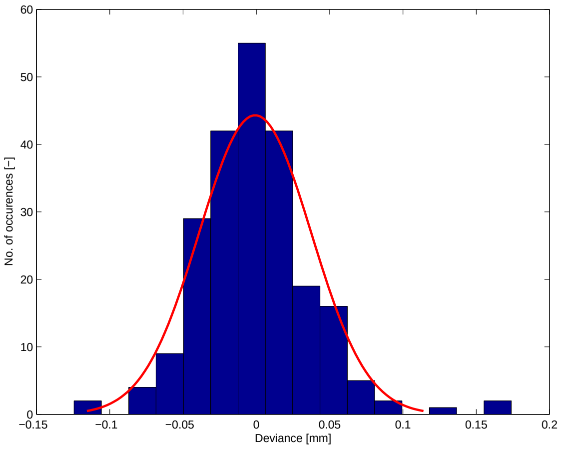

Figure 5.60: Error distribution for the momentum thickness with respect to linear moving average.

	Absolute	Relative [%]
H	± 0.0032 [-]	± 0.24
θ	± 0.011 [mm]	± 0.18
δ^*	± 0.026 [mm]	± 0.32
Re_θ	± 19.7 [-]	± 0.18

Table 5.10: Estimated maximum value of 95% confidence intervals for trendlines of the integral parameters.

correct. As mentioned earlier, the deviation from the trend includes a non-random component related to the reflection of the laser. Furthermore, this analysis does not include all uncertainties. First of all, there is an additional uncertainty due to the PIV post-processing procedure, discussed in section 4.1. Also the bias and additional random errors due to the lens effects, discussed in section 5.2.1, are not included in the calculated confidence intervals. However, the values in table 5.9 do give insight in the combined uncertainty within the calculation of the integral parameters.

The calculated intervals above, are approximately valid for individual measurements of the integral parameters. However, for the data presented in this chapter, often very clear trends could be observed. The confidence intervals presented above are not representative for the uncertainty in these trends. In order to get insight in this uncertainty, the 95 % confidence interval for the linear trendline itself (depicted in figure 5.59) is calculated [26]. Figure 5.61 shows the results of this calculation for θ. It can be observed that the uncertainty in the trend, is clearly lower than the uncertainty in the individual measurements. It can also be observed that the uncertainty in the trend reaches a maximum near the edges of the domain. Table 5.10 presents this maximum value of the confidence intervals for the linear trendlines for each of the integral parameters. Again, these values may not be exactly correct but they do give a fair estimation of the order of magnitude of the uncertainty of the results. Taking all the above into account, the author feels that the findings and conclusions in the previous sections are not invalidated by the calculated confidence intervals.

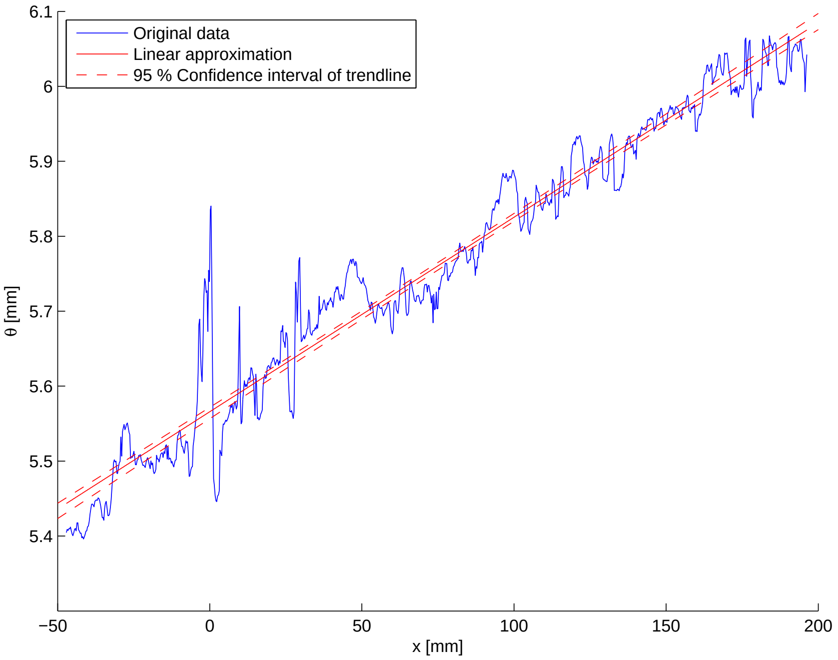

Figure 5.61: Confidence interval of the linear approximation for the momentum thickness in the region -50 $\leq x \leq$ 200. Result for the zero pressure gradient case without suction.

Chapter 6

Conclusions and Recommendations

The main goal of the research described in this report was to study the effect of slot suction on an incompressible two-dimensional turbulent boundary layer experiencing an adverse pressure gradient. A literature review has shown a gap in knowledge for the subject of slot suction at 'relatively high' Reynolds numbers (i.e. $\mathrm{Re}_\theta \geq 2{,}000$), and more specifically, for slot suction at the conditions of an adverse pressure gradient. From the general research goal, a number of sub goals were deduced. Some of these were more closely related to the engineering application of slot suction on a thick wind turbine airfoil (AF-0901).

In order to achieve these goals, an experimental investigation has been conducted in the W-tunnel facility at the DUT. In chapter 3, the experimental setup, measurement methods and measurement procedures are discussed in detail. In short, two-component planar PIV measurements have been performed for boundary layer slot suction at a zero pressure gradient and at an adverse pressure gradient of $\frac{\partial p}{\partial x} = 200$ [Pa/m]. Furthermore, for the adverse pressure gradient, comparative measurements have been conducted for distributed suction through a porous plastic and a perforated plate. These latter measurements were performed to be able to put the results for slot suction in a broader perspective.

The data obtained from the experiments has been processed using the methods described in chapter 4 and the results for the mean flow field are presented and detailedly discussed in chapter 5. The current chapter presents the most important conclusions stemming from these results. Furthermore, recommendations for further research are presented, based on the findings in this report.

6.1 Conclusions

The conclusions of this report are discussed in the following three subsections. Firstly, the validation of the results is discussed. Secondly, the conclusions regarding slot suction are presented. Finally, the conclusions from the comparison between slot suction and distributed suction are discussed.

Validation of results

As for all experimental investigations, it is necessary to validate the results and identify possible measurement errors. For the current experiment, this validation has mainly been performed for the measurements without suction.

From a first inspection of the results for the zero pressure gradient boundary layer without suction, some unexpected deviations were found. That is, from the streamwise development of the momentum thickness, θ, non-monotonic behaviour was observed, in the form of two humps. Although the deviation from the trend was not more than 3 %, it was deemed important to exclude the possibility of these humps arising from any physical phenomenon. It was found that the erroneous humps, were caused by lens distortions. Apparently, these were of a too high order to correct for, using the image correction functions in DaVis.

The boundary layer velocity profile was also compared with a theoretical turbulent boundary layer velocity profile. It was found that, for both the zero pressure gradient and the adverse pressure gradient, there was good correspondence with Coles' law of the wake. The friction coefficient was also obtained through the Clauser technique, and compared to theoretical results for a boundary layer described by Coles' law of the wake. This comparison showed acceptable correspondence for both the zero pressure gradient and the adverse pressure gradient boundary layer.

For the zero pressure gradient boundary layer, the streamwise increase in momentum thickness has been compared with the predicted value through the integral momentum equation. It was found that the rate of growth for the momentum thickness in the current experiment was nearly twice the theoretically predicted value. Corner vortices, moving low momentum from the corner towards the mid plane of the tunnel, have been identified as a possible cause for this. These corner vortices are a typical secondary flow, found in square ducts with turbulent flow and generally have a magnitude of 1 % of the axial velocity. For the adverse pressure gradient boundary layer, the absolute deviation in the growth of the momentum thickness was found to be of similar magnitude as for the zero pressure gradient case.

Concluding, the non-monotonic behaviour in the results was found to have no physical cause, but was a result of measurement errors. Furthermore the rate of growth of the integral parameters was found higher than the theoretically predicted value. However, since the boundary layer velocity profile complied with that of a theoretical two-dimensional turbulent boundary layer, it is assumed that the measurements are representative for two-dimensional boundary layer suction.

In addition to the validation of the results, an uncertainty analysis has also been performed. From this analysis it was estimated that the 95 % confidence interval for the individual measurements of the integral parameters, was in the order of 2 % of the mean values. The uncertainty in the trendlines was estimated to be an order of magnitude lower. It is believed that these uncertainties do not affect the validity of the conclusions in the upcoming two paragraphs.

Suction through a slot

From the measurements with suction through a slot, a typical pattern was found for the streamwise velocity in the boundary layer. Upstream of the slot, there was an increase in streamwise velocity whereas downstream of the slot there was a decrease with respect to the unperturbed flow.

The measured wall pressure distribution could naturally be linked to this velocity pattern. Corresponding with findings from Park et al. [29], it was found that the flow experiences a favourable pressure gradient in front of and behind the slot, and an adverse pressure gradient above the slot. The presence of an adverse pressure gradient did not alter the local disturbance in the pressure distribution due to the slot. That is, if the pressure field for the measurement without suction was subtracted from results with suction, the resulting pressure distribution matched that for the zero pressure gradient case with suction. Apparently, the adverse pressure gradient only acts as a bias and does not alter the qualitative and quantitative effects on the pressure distribution.

The results for the momentum thickness and the shape factor also showed a typical pattern in the region close to the slot. This pattern matched the findings from Park et al. for the zero pressure gradient case. Downstream of the local disturbance, it was found that the integral parameters developed equally to the case without suction, but at a reduced value.

For the Reynolds number based on the momentum thickness, it was found that this reduction was linearly (or possibly weakly non-linearly) dependent on the suction parameter, σ. This matched the findings from Park et al. and Antonia et al. [2] for the zero pressure gradient boundary layer. The presence of an adverse pressure gradient altered this relation neither qualitatively, nor quantitatively. For both cases, a value of $\sigma = 1.0$ resulted in a reduction of 32 % with respect to the reference value.

For the shape factor, the relation with σ was found to be non-linear, again in correspondence with the findings from Park et al. This non-linear relation was not qualitatively different for the case with an adverse pressure gradient. However, it was found that the reduction in shape factor, was higher for the case with an adverse pressure gradient. For $\sigma = 1.0$, the reduction in shape factor was found to be 5 % and 13 % for the zero and adverse pressure gradient case respectively. The difference in shape factor for the undisturbed boundary layer between these two cases, is identified as the most likely cause for this discrepancy.

Finally, the effect of suction with different slot widths was investigated. It was found that changing the slot width from $\frac{W}{\delta} = 0.05$ to $\frac{W}{\delta} = 0.2$, apart from very local effects, did not change the effects of suction on the momentum thickness and the shape of the boundary layer. These findings are in correspondence with the observations from Fage et al. [12] and Pierpont et al. [30].

The slot width having no influence on the external flow, results in more flexibility in finding the optimal engineering application. For the application on wind turbines as introduced in chapter 1 this means that one is free to choose that slot width, for which the pressure drop is satisfactory. Hereby the required suction coefficient can be reached, for a given negative pressure inside the turbine blade. Furthermore, structural considerations might also influence the decision on the slot width to use.

Summarising the findings on the measurements of slot suction, a generally good agreement with the results from Park et al. was found. The difference in Reynolds number for their investigation ($\mathrm{Re}_\theta \approx 500$) and the current investigation ($\mathrm{Re}_\theta \approx 10{,}000$) did not change the qualitatively effects of slot suction on the boundary layer. The influence of an adverse pressure gradient on the effects of suction was limited to the results for the shape factor of the boundary layer.

In a broader perspective, these findings imply that the literature on low Reynolds number, zero pressure gradient boundary layers with suction, can be considered qualitatively representative for the effect of suction on the mean flow at more engineering level flow conditions. However, with respect to the quantitative effects, the current results form a valuable addition to the currently available literature.

Slot suction compared with distributed suction

For the adverse pressure gradient, measurements have also been performed for suction through a porous plastic and a perforated plate. These measurements were performed in order to compare the effects of high velocity localised slot suction with low velocity distributed suction.

It was found that suction through the porous plastic and the perforated plate resulted in similar flow fields. The pressure distribution and streamwise development of the integral parameters, θ and H, were also comparable for both cases. Furthermore it was found that for high suction rates, where the suction velocity was still relatively high (i.e. 5 % of the freestream velocity), the local suction effects resembled those of slot suction, but with a lower amplitude. For low suction rates, the local effects on suction were found to be more representative for actual distributed suction (i.e. suction velocities approximately 1 % of the freestream velocity).

Despite this qualitative difference, for both suction rates, it was found that downstream of the region of suction, the results for slot suction and distributed suction approximately collapsed. Similarly to the findings on varying slot width, it is concluded that the suction rate σ is the determining parameter for the effects downstream of the slot, where the local disturbances have vanished.

This result implies that, when taking into account the local effects, both distributed and localised suction can possibly be used to obtain the same results. This gives an additional degree of freedom in designing wind turbine blades for boundary layer suction. The eventual decision for using either localised or distributed suction depends on a trade-off between aerodynamic, structural and practical arguments.

6.2 Recommendations

Although valuable knowledge has been gained from this research, there are recommendations for further research. This section presents the most important of these recommendations.

First of all, the author believes that the dataset from the current experiment can be used for further investigation. The validity of the dataset has been demonstrated by a comparison of the results with theory and literature. Within this report only a selection of the results from this dataset is presented. The entire dataset contains valuable information on the mean and fluctuating components of the velocity within the boundary layer subjected to either localised or distributed suction. As was pointed out in the introduction of this report, reference data is extremely scarce on this topic. It is therefore recommended that this flow problem is also solved with numerical tools, for which the current dataset can serve as a validation. This can give improved insights in the usability of numerical tools to describe the problem of boundary layer slot suction, and possibly help in improvement or selection of current numerical methods.

This report focussed on the effect of suction on the mean properties of the flow and compared these with available low Reynolds number literature. As already mentioned in the introduction of this report, these results were considered outside the scope of this work. Investigating the effects on the turbulence characteristics and also comparing these with the low Reynolds number literature, could give additional insights. These insights might help to better understand the relation between suction, turbulence and Reynolds number. It is therefore recommended to further explore the current dataset, in terms of turbulence characteristics.

The current experiment had some limitations which can be improved upon in an additional experimental campaign. First of all, it is recommended to perform similar measurements in a larger wind tunnel facility, to avoid the effects of corner vortices. A few additional measurements could already confirm whether the conclusions with respect to the effect of suction are similar to the ones from the current dataset.

Next to that, it is recommended to perform additional measurements for distributed suction, but with a lower velocity. It has been shown that the lowest suction coefficient in the current research still resulted in suction velocities slightly above 1 % of the freestream velocity. From the additional measurements it can then be confirmed if the current findings can be extrapolated to a situation more representative for the envisioned application on wind turbine airfoils. That is, a situation where the suction velocity is a magnitude lower and the boundary layer approximations are still valid. Furthermore, this data could then also be used as validation for numerical tools, which are based on solving the turbulent boundary layer equations.

Finally, it is recommended to perform further research towards the role of the initial shape of the boundary layer, on the effectiveness of suction. From the current research it appears that slot suction becomes more effective for a profile which is less full. Although the same presumption was made in [28], the author thinks that further research is needed to come to a definite conclusion on this matter.

References

[1] R.A. Antonia, L.V. Krishnamoorthy, L. Fulachier, T. Benabid, and F. Anselmet. Influence of wall suction on the organized motion in a turbulent boundary layer. *Journal of Fluid Mechanics*, 190:217–240, 1988.

[2] R.A. Antonia, Y. Zhu, and M. Sokolov. Effect of concentrated wall suction on a turbulent boundary layer. *Physics of Fluids*, 7:2465, 1995.

[3] M. Birsanu. Aerodynamic tip design of a wind turbine equipped with boundary layer suction. Master's thesis, Delft University of Technology, 2011.

[4] P. Bradshaw. *Turbulence*. Springer, 1976.

[5] P. Bradshaw. Turbulent secondary flows. *Annual review of fluid mechanics*, 19(1):53–74, 1987.

[6] Catec. *High-Precision Air / Gas Velocity Transmitter for Industrial Applications*, 2006.

[7] C.F. Colebrook. Turbulent flow in pipes, with particular reference to the transition region between the smooth and rough pipe laws. *Journal of the ICE*, 11(4):133–156, 1939.

[8] J.S. Connelly, M.P. Schultz, and K.A. Flack. Velocity-defect scaling for turbulent boundary layers with a range of relative roughness. *Experiments in fluids*, 40(2):188–195, 2006.

[9] A.O. Demuren and W. Rodi. Calculation of turbulence-driven secondary motion in non-circular ducts. *Journal of Fluid Mechanics*, 140(1):189–222, 1984.

[10] L. Djenidi, P.E. Gall, A. Vincent, and R.A. Antonia. Effect of wall suction on the structure of a turbulent boundary layer. In *Proceeding of the 11th Int. Symp. on Application of Laser Techniques to Fluid Mechanics, Lisbon, Portugal*, pages 8–11, 2002.

[11] H.A. Einstein and H. Li. Secondary currents in straight channels. *Transactions, American Geophysical Union*, 39:1085–1088, 1958.

[12] A. Fage and R.F. Sargent. Design of suction slots. *Technical report*, 63:341, 1953.

[13] M. Gad-el Hak. *Flow control: passive, active, and reactive flow management.* Cambridge Univ Pr, 2000.

[14] K. Ghosh and R.J. Goldstein. Verification of the clauser technique in predicting wall shear stress. *AIAA journal*, 48(1):252–256, 2010.

[15] Höntzsch GmbH. *Thermal Flow Sensors TA with thin-film sensor element*, 2006.

[16] R. Gurka, A. Liberzon, D. Hefetz, D. Rubinstein, and U. Shavit. Computation of pressure distribution using piv velocity data. In *International Workshop on PIV'99- Santa Barbara, 3 rd, Santa Barbara, CA*, pages 671–676, 1999.

[17] S.E. Haaland. Simple and explicit formulas for the friction factor in turbulent pipe flow. *Journal of Fluids Engineering*, 105(1):89–90, 1983.

[18] Pramote Hochareon. *Development of particle image velocimetry (PIV) for wall shear stress estimation within a 50cc Penn State artificial heart ventricular chamber.* PhD thesis, Pennsylvania State University, 2003.

[19] T.P. van der Hoeven. Literature review: Localised suction of the turbulent boundary layer through a slot. Technical report, Actiflow B.V., 2012.

[20] I.E. Idelchik and E. Fried. Handbook of hydraulic resistance. 1986.

[21] T. Karman. Über laminare und turbulente reibung. *ZAMM-Journal of Applied Mathematics and Mechanics/Zeitschrift für Angewandte Mathematik und Mechanik*, 1(4):233–252, 1921.

[22] J. Kim, K. Kim, and H.J. Sung. Wall pressure fluctuations in a turbulent boundary layer after blowing or suction. *AIAA journal*, 41(9):1697–1704, 2003.

[23] K. Kim, H.J. Sung, and M.K. Chung. Assessment of local blowing and suction in a turbulent boundary layer. *AIAA J*, 40(1):175–177, 2002.

[24] C.P. Kothandaraman and R. Rudramoorthy. *Basic Fluid Mechanics.* New Age International, 2007.

[25] A. Melling and J.H. Whitelaw. Turbulent flow in. *J. Fluid Mech*, 78(part 2):289–315, 1976.

[26] Douglas C Montgomery, Elizabeth A Peck, and G Geoffrey Vining. *Introduction to linear regression analysis*, volume 821. Wiley, 2012.

[27] E. Obert, R. Slingerland, D.J.W. Leusink, T. van den Berg, J.H. Koning, and M.J.L. van Tooren. *Aerodynamic design of transport aircraft.* Ios Press, 2009.

[28] O. Oyewola, L. Djenidi, and R.A. Antonia. Combined influence of the reynolds number and localised wall suction on a turbulent boundary layer. *Experiments in fluids*, 35(2):199–206, 2003.

[29] J. Park and H. Choi. Effects of uniform blowing or suction from a spanwise slot on a turbulent boundary layer flow. *Physics of fluids*, 11:3095, 1999.

[30] P.K. Pierpont. Investigation of suction-slot shapes for controlling a turbulent boundary layer, 1947.

[31] L. Prandtl. Über flüssigkeitsbewegung bei sehr kleiner reibung. In *Proceedings of 3rd International Mathematics Congress, Heidelberg*, 1904.

[32] M. Raffel, C.E. Willert, S.T. Wereley, and J. Kompenhans. Particle image velocimetry: A practical guide. *Berlin, Springer Science+ Business Media Deutschland GmbH, 2007. 463*, 2007.

[33] C.L. Rumsey et al. Summary of the 2004 cfd validation workshop on synthetic jets and turbulent separation control. 2004.

[34] A. Savitzky and M.J.E. Golay. Smoothing and differentiation of data by simplified least squares procedures. *Analytical chemistry*, 36(8):1627–1639, 1964.

[35] F. Scarano. Experimental aerodynamics. 2007.

[36] H. Schlichting and K. Gersten. *Boundary-layer theory.* Springer Verlag, 2000.

[37] D.B. Spalding. A single formula for the "law of the wall". *Journal of Applied Mechanics*, 28:455, 1961.

[38] J. Stewart. *Calculus Early Transcendentals.* Brooks/Cole, 2003.

[39] M.F. Tachie, M. Agelinchaab, and M.K. Shah. Turbulent flow over transverse ribs in open channel with converging side walls. *International journal of heat and fluid flow*, 28(4):683–707, 2007.

[40] J.R. Taylor. *An introduction to error analysis: the study of uncertainties in physical measurements.* Univ Science Books, 1997.

[41] S.D. Veenhuizen and R.N. Meroney. Secondary flow in a boundary layer. Technical report, DTIC Document, 1969.

[42] L.L.M. Veldhuis. Aircraft aerodynamics primer. Draft - Version 0.9, 2011.

[43] T. Wei, R. Schmidt, and P. McMurtry. Comment on the clauser chart method for determining the friction velocity. *Experiments in fluids*, 38(5):695–699, 2005.

[44] F.M. White. *Fluid Mechanics.* McGraw-Hill inc., 1994.

[45] F.M. White. *Viscous fluid flow. 3rd edition.* Boston: McGraw-Hill, 2006.

[46] J. Williams, R.C. Pankhurst, and E.M. Love. *Wind Tunnel Tests on the NPL434 Nose Slot Suction Aerofoil.* HM Stationery Office, 1952.

Appendix A

Test Matrices

Case	σ [-]	W/δ [-]	Diffusor Angle [deg]	Remarks
2D1	-	-	0	These measurements are hotwire measurements to measure the two-dimensionality of the flow
2D2	-	-	0	
2D3	-	-	0	
2D4	-	-	0	
2D5	-	-	0	
Zero Pressure Gradient Measurements				
Closed1	-	-	0	Reference Measurement
P0W0_1	0.1	0.05	0	
P0W0_2	0.2	0.05	0	
P0W0_3	0.4	0.05	0	
P0W0_4	0.7	0.05	0	
P0W0_5	1.0	0.05	0	
P0W1_1	0.1	0.2	0	
P0W1_2	0.2	0.2	0	
P0W1_3	0.4	0.2	0	
P0W1_4	0.7	0.2	0	
P0W1_5	1.0	0.2	0	
P0W2_1	0.1	0.5	0	
P0W2_2	0.2	0.5	0	
P0W2_3	0.4	0.5	0	
P0W2_4	0.7	0.5	0	
P0W2_5	1.0	0.5	0	
‘Low’ Adverse Pressure Gradient Measurements				
Closed2	-	-	5.4	Reference Measurement
P1W0_1	0.1	0.05	5.4	
P1W0_2	0.2	0.05	5.4	
P1W0_3	0.4	0.05	5.4	
P1W0_4	0.7	0.05	5.4	
P1W0_5	1.0	0.05	5.4	
P1W1_1	0.1	0.2	5.4	
P1W1_2	0.2	0.2	5.4	
P1W1_3	0.4	0.2	5.4	
P1W1_4	0.7	0.2	5.4	
P1W1_5	1.0	0.2	5.4	
P1W2_1	0.1	0.5	5.4	
P1W2_2	0.2	0.5	5.4	
P1W2_3	0.4	0.5	5.4	
P1W2_4	0.7	0.5	5.4	
P1W2_5	1.0	0.5	5.4	
‘High’ Adverse Pressure Gradient Measurements				
Closed3	-	-	10.7	Reference Measurement
P2W0_1	0.1	0.05	10.7	
P2W0_2	0.2	0.05	10.7	
P2W0_3	0.4	0.05	10.7	
P2W0_4	0.7	0.05	10.7	
P2W0_5	1.0	0.05	10.7	
P2W1_1	0.1	0.2	10.7	
P2W1_2	0.2	0.2	10.7	
P2W1_3	0.4	0.2	10.7	
P2W1_4	0.7	0.2	10.7	
P2W1_5	1.0	0.2	10.7	
P2W2_1	0.1	0.5	10.7	
P2W2_2	0.2	0.5	10.7	
P2W2_3	0.4	0.5	10.7	
P2W2_4	0.7	0.5	10.7	
P2W2_5	1.0	0.5	10.7	

Table A.1: Testmatrix for the first measurement campaign.

Case	σ [-]	W/δ [-]	Diffusor Angle [deg]	Remarks
Closed	-	-		Reference Measurement
Suc1	0.1	0.2	1 ($\mathrm{d}p/\mathrm{d}x \approx 0$)	
Suc2	0.2	0.2	1 ($\mathrm{d}p/\mathrm{d}x \approx 0$)	
Suc3	0.4	0.2	1 ($\mathrm{d}p/\mathrm{d}x \approx 0$)	
Suc4	0.7	0.2	1 ($\mathrm{d}p/\mathrm{d}x \approx 0$)	
Suc5	1.0	0.2	1 ($\mathrm{d}p/\mathrm{d}x \approx 0$)	
ClosedP	-	-	13.7	Reference Measurement
SucP1	0.1	0.2	13.7 ($\mathrm{d}p/\mathrm{d}x \approx 200$)	
SucP2	0.2	0.2	13.7 ($\mathrm{d}p/\mathrm{d}x \approx 200$)	
SucP3	0.4	0.2	13.7 ($\mathrm{d}p/\mathrm{d}x \approx 200$)	
SucP4	0.7	0.2	13.7 ($\mathrm{d}p/\mathrm{d}x \approx 200$)	
SucP5	1.0	0.2	13.7 ($\mathrm{d}p/\mathrm{d}x \approx 200$)	
ClosedPorous	-	-	13.7 ($\mathrm{d}p/\mathrm{d}x \approx 200$)	Reference Measurement
Porous1	0.2	1.8	13.7 ($\mathrm{d}p/\mathrm{d}x \approx 200$)	
Porous2	0.4	1.8	13.7 ($\mathrm{d}p/\mathrm{d}x \approx 200$)	
Porous3	0.7	1.8	13.7 ($\mathrm{d}p/\mathrm{d}x \approx 200$)	
ClosedPerf	-	-	13.7 ($\mathrm{d}p/\mathrm{d}x \approx 200$)	Reference Measurement
Perf1	0.2	1.8	13.7 ($\mathrm{d}p/\mathrm{d}x \approx 200$)	
Perf2	0.4	1.8	13.7 ($\mathrm{d}p/\mathrm{d}x \approx 200$)	
Perf3	0.7	1.8	13.7 ($\mathrm{d}p/\mathrm{d}x \approx 200$)	

Table A.2: Testmatrix for the second measurement campaign.

Appendix B

Suction Rate Measurement Method

This appendix discusses the theoretical principles underlying the suction rate measurement technique introduced in section 3.3.4. Furthermore it presents the results from the tests, performed prior to the main experiment, to determine the validity of this technique. The first section discusses the relevant theory, while the second section briefly describes the setup used for these tests. The third section describes the results related to the shape of the velocity profile within the pipe, while the final section describes the results, related to the measured maximum velocity using either a hot film flowmeter or a pitot tube.

B.1 Pipe Flow Velocity Profile

This section describes the development of a velocity profile within a pipe. More specifically, it is shown how the maximum velocity measured in a pipe can, theoretically, be related to the mass flow. As was discussed in chapter 3, the measurement method that has been used to determine the suction velocity, V_w, is based on this theoretical concept.

Depending on the Reynolds number of the flow through a pipe, the flow is either laminar, transitional or turbulent. The Reynolds number ranges, corresponding to these regimes, are as follows:

- Laminar: $0 \leq \mathrm{Re}_d \leq 2{,}000$
- Transitional: $2{,}000 < \mathrm{Re}_d < 4{,}000$
- Turbulent: $\mathrm{Re}_d \geq 4{,}000$

Here, Re_d is the Reynolds number based on the average velocity within the pipe and the pipe diameter. Both the shape of the fully developed velocity profile and the pipe length, needed for this profile to become fully developed, are dependent on the Reynolds number. For laminar flow, the fully developed velocity profile has a parabolic shape with quite a small ratio between the average and the maximum velocity. For turbulent flow, the velocity profile is much ‘fuller’ and the ratio between the average and maximum velocity grows closer to one for increasing Reynolds number. An illustration of the difference in velocity profile can be found in figure B.1.

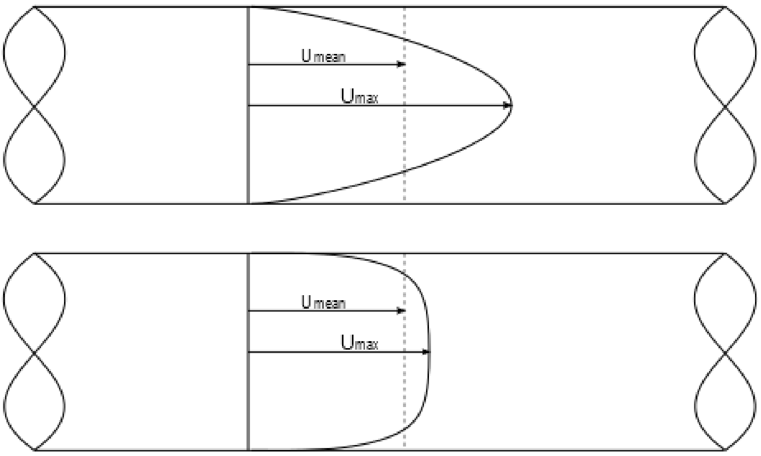

Figure B.1: Typical laminar and turbulent velocity profile within a pipe.

The position at which the velocity profile is fully developed is also known as the entrance length. For turbulent flows (i.e. $\mathrm{Re}_d \geq 4{,}000$) this can be approximated according to equation B.1 [44].

$$\frac{L_e}{D} = 4.4 Re_d^{1/6} \tag{B.1}$$

Here, L_e is the entrance length, D the pipe diameter, and Re_d is the Reynolds number based on this diameter. Now, if the velocity profile is fully developed, one can define a relation between the maximum velocity and the average velocity within the pipe. The Darcy-Weisbach friction factor is a theoretical concept often used in order to evaluate this ratio. The equation describing the relation between this friction factor, the Reynolds number and pipe characteristics is also known as the Colebrook-White equation [7] and is given by:

$$\frac{1}{\sqrt{f}} = 2log_{10}\left(\frac{\epsilon}{3.7D_h} + \frac{2.51}{Re_d\sqrt{(f)}}\right) \tag{B.2}$$

Here, f is the Darcy friction factor, ϵ is the roughness height of the pipe, and D_h is the hydraulic diameter. A simple but accurate explicit approximation for the Darcy friction factor has been obtained by S.E. Haaland in 1983 and is given in equation B.3. For a Reynolds number range of $4{,}000 \leq \mathrm{Re}_d \leq 10^8$ this equation estimates the Colebrook-White relation with ± 1.5 % accuracy [17].

$$\frac{1}{\sqrt{f}} = -1.8log_{10}\left[\left(\frac{\epsilon/D_h}{3.7}\right) + \frac{6.9}{Re}\right] \tag{B.3}$$

Finally, the mean velocity can now be found through a relation between the velocity ratio and the Darcy friction factor given in equation B.4 [24].

$$\frac{U_{mean}}{U_{max}} = \frac{1}{1 + 1.33\sqrt{f}} \tag{B.4}$$

Concluding, using the relations presented above, it is possible to calculate the ratio between the mean and maximum velocity within a pipe, for a given maximum velocity and pipe diameter. However, it should be taken into account that these are only applicable when the velocity profile is fully developed. In section 3.3.4 it was explained how the above described theory is used in order to measure the suction velocity.

B.2 Test Setup

The setup used during this preparatory experiment consisted of a 4 [m] long pipe with a 77 [mm] inner diameter. At one side, the pipe was open, while at the other side it was connected to a suction pump. At 50 [cm] from the suction pump, the velocity within the pipe could be measured either by a hotfilm element or a pitot tube. Figure B.2 shows a schematical representation of the test setup.

This experimental setup has been used to measure velocity profiles within the pipe for different velocities. The results from these measurements are presented in the next section. Furthermore the maximum velocity measured by a pitot tube has been compared with the velocity measured by the hotfilm element. The results of this comparison can be found in section B.4.

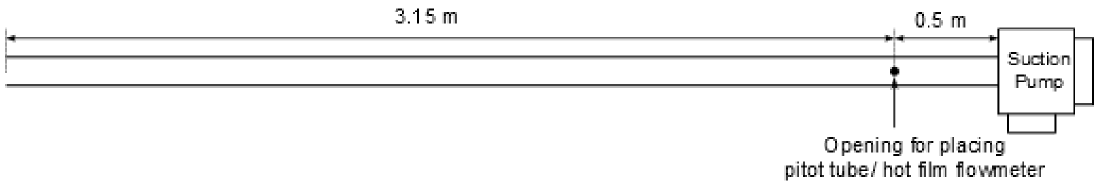

Figure B.2: Schematical overview of test setup for validation of volume measurement method.

B.3 Velocity Profile

As mentioned before, the velocity within the pipe could either be measured using a pitot tube or a hotfilm element (EE75 Velocity/Temperature Transmitter). Comparing them: the pitot tube offers a higher spatial resolution and is less intrusive due to its small cross-section. The hotfilm element on the other hand is more easy to position and is capable of measuring both low and high velocities accurately.

In order to measure velocity profiles within the pipe, the pitot tube was used. The main reason for using the pitot tube was its high spatial resolution. Figure B.3 shows the velocity profiles obtained at different suction rates. These profiles were obtained by taking the mean value of three measurements. When normalising these velocity profiles by the maximum velocity, one can observe that the velocity profile becomes slightly 'fuller' for increasing velocity (i.e. increasing Reynolds number). This has already been explained in section B.1 and can also be observed from the data presented in table B.1. Here, one can see the ratio between the maximum and the mean velocity obtained from the measurements together with the theoretical value for this ratio. The higher this ratio, the 'fuller' the velocity profile is.

The ratios obtained from the experimental data are based on a polynomial fit through the measurement points. An example of such a fit can be seen in figure B.4. From table B.1, one can observe that the flow in the pipe is indeed fully developed. The slight differences between the theoretical values and the obtained experimental values are accepted since they are within the limits of accuracy of this experiment. After all the error between these values is below 1 %.

Based on the data presented above it was decided to use the theory from section B.1 to determine the velocity ratio, and thus the maximum velocity to be measured for a particular volume flow. This is especially needed for the low suction quantities as the author was unable to obtain velocity profiles experimentally for pipe velocities below 3 [m/s].

U_{max}	Measured Velocity Ratio [-]	Theoretical Velocity Ratio [-]	Error [%]
10	0.841	0.834	0.78
20	0.846	0.841	0.68
30	0.841	0.844	0.40
40	0.854	0.846	0.99

Table B.1: U_{mean}/U_{max} according to theory and from experiment.

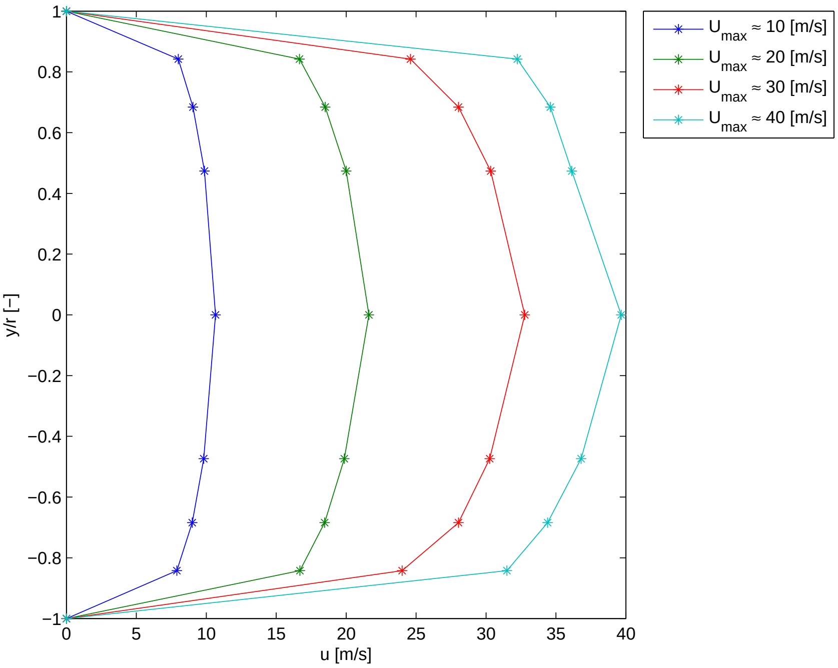

Figure B.3: Measured velocity profiles within pipe

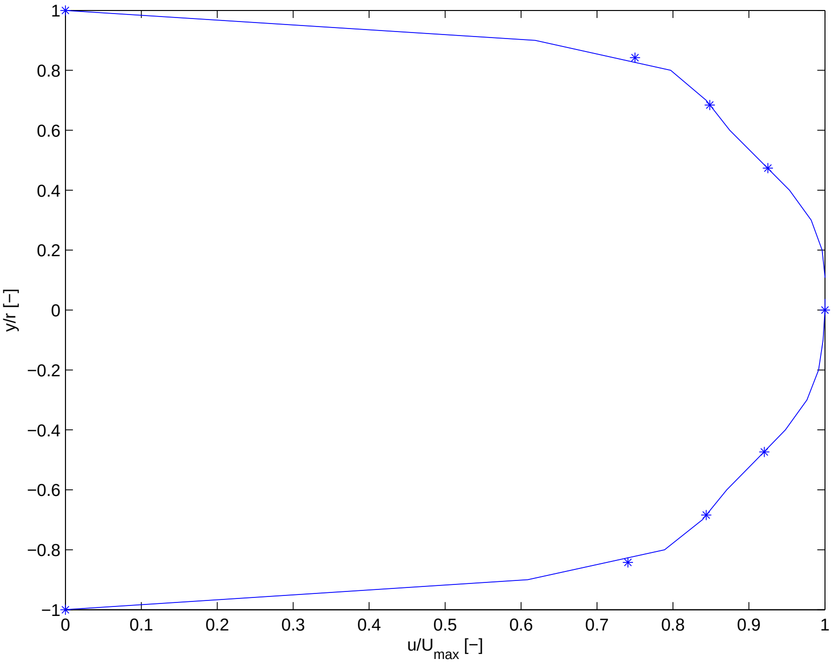

Figure B.4: Fit through data points for $U_{max} \approx 10$.

B.4 Maximum Measured Velocity

At low velocities (i.e. 1 to 2 [m/s]) the hotfilm flow meter has a measurement error of approximately 1 %.[1] On the other hand, the Scanivalve Pressure scanner used for this experiment, has a resolution of approximately 1 [Pa]. Now for low velocities, for example 2 [m/s], the dynamic pressure is in the order of magnitude of the velocity squared (i.e. 4 [Pa]). Now with an uncertainty of 1 [Pa], this results in measurement uncertainties of as much as 25 %. Therefore, during the actual experiment the hotfilm flowmeter has been used, despite its intrusiveness and limited spatial resolution.

This section describes the results from measurements that were carried out to compare the maximum velocity measured by the hotfilm flowmeter and the pitot tube at higher velocities. Based on these measurements conclusions are drawn on the correctness of the velocity obtained by the hotfilm element. That is, it is verified that the hotfilm measurements do not give results which are completely off the measurements obtained by the pitot tube measurements.

Before presenting the results, firstly the causes for a discrepancy between the data from the two measurement devices should be considered. The author identifies four main causes for this, of which two were already briefly mentioned:

- The hotfilm device causes blockage in the pipe, thereby increasing the velocity locally (conservation of mass).
- The blockage of the hotfilm device is accompanied by a slight pressure loss causing the pump to work at another point at its working curve. This point corresponds to an increased pressure, but a decreased volume flow and thus measured velocity.
- Due to the fact that the hotfilm sensor is quite large (6 [mm]), the measured velocity is an average. With the velocity profile within a pipe this means that the measured average will be slightly below the actual maximum velocity.
- Despite the careful positioning of the sensors, a slight error in the alignment with the flow direction might cause significant errors in the measured maximum velocity. This is especially true for the pitot tube. The EE75 sensor has an error below 3 % for a misalignment angle of 20 degrees [6].

Three separate measurement series were performed of which the results are summarised in table B.2. From the table it can be observed that the difference between the measured velocities mostly is in the order of magnitude of 2-4 %. More specifically it was observed from the complete data set that the maximum deviation between both measurements is within 5 % for 95 % of the measurements. Furthermore, it can be observed from table B.2 that the mean deviation between the measurements decreases with increasing velocity. This might be due to the increasing accuracy of the pitot measurements at higher velocities. When considering the maximum deviation there is a less clear pattern with respect to the differences between the two measurement devices.

Taking into account the sources of error described above, the results of the measurements seem to be realistic. The maximum error is in the order of magnitude of 5 % which clearly shows that the hotfilm measurements are comparable with the pitot measurements. This also implies that the intrusiveness and the limited spatial resolution of the hotfilm element, do not cause very large measurement errors. The documentation on a similar hotfilm measurement device confirms that the intrusiveness of the flow meter in this setup is indeed negligible [15]. From this document it can be seen that when the pipe diameter is above 50 [mm], the ratio between the measured maximum and the mean flow does not change with increasing pipe diameter.

Recapitulating, it has been demonstrated by two types of measurements that the volume measurement with the hotfilm element gives realistic results. Without being able to give an exact

---

[1] According to manufacturer's calibration certificate

Velocity range [m/s]	Average deviation [%]	Maximum deviation [%]
5 - 15	4.02	5.99
15 - 30	2.78	4.05
30 - 40	1.82	4.14

Table B.2: Mean and maximum deviation between hotfilm and pitot measurements at different velocity ranges.

calculated estimate of the accuracy of the measurement method (no fixed reference to compare with) it was shown that the hotfilm measurements and the pitot tube measurements were within 5 % of each other for nearly all measurements. The author feels that it is thereby validated, that the hotfilm measurement method can be used to give a realistic measure of the volume passing through the pipe.

Appendix C

Derivation of Two-Dimensional Poisson Equation for the Mean Pressure

This appendix shows the derivation of the Poisson equation for the mean pressure, of a two-dimensional incompressible turbulent flow.

In order to do so, let us consider the two-dimensional Reynolds averaged conservation of mass and of momentum for the incompressible mean turbulent flow. Note that although all pressure and velocity terms are mean values, the overbars are omitted for convenience.

$$\frac{\partial u}{\partial x} + \frac{\partial v}{\partial y} = 0 \tag{C.1}$$

$$u\frac{\partial u}{\partial x} + v\frac{\partial u}{\partial y} = -\frac{1}{\rho}\frac{\partial p}{\partial x} + \nu\Delta^2 u - \left(\frac{\partial u'^2}{\partial x} + \frac{\partial u'v'}{\partial y}\right) \tag{C.2}$$

$$u\frac{\partial v}{\partial x} + v\frac{\partial v}{\partial y} = -\frac{1}{\rho}\frac{\partial p}{\partial y} + \nu\Delta^2 v - \left(\frac{\partial u'v'}{\partial x} + \frac{\partial v'^2}{\partial y}\right) \tag{C.3}$$

The first step, is to differentiate the x-momentum equation (C.2) with respect to x, and the y-momentum equation (C.3) with respect to y. Doing so, and adding both equations results in:

$$\begin{aligned}
-\frac{1}{\rho}\left(\frac{\partial^2 p}{\partial x^2} + \frac{\partial^2 p}{\partial y^2}\right) &= u\left(\frac{\partial^2 u}{\partial x^2} + \frac{\partial^2 v}{\partial x \partial y}\right) + v\left(\frac{\partial^2 v}{\partial y^2} + \frac{\partial^2 u}{\partial x \partial y}\right) + \left(\frac{\partial u}{\partial x}\right)^2 + \left(\frac{\partial v}{\partial y}\right)^2 \\
&+ 2\left(\frac{\partial v}{\partial x}\frac{\partial u}{\partial y}\right) - \nu\left(\frac{\partial^3 u}{\partial x^3} + \frac{\partial^3 u}{\partial y^2 \partial x} + \frac{\partial^3 v}{\partial y^3} + \frac{\partial^3 v}{\partial x^2 \partial y}\right) + \left(\frac{\partial^2 u'^2}{\partial x^2} + 2\left(\frac{\partial^2 u'v'}{\partial x \partial y}\right) + \frac{\partial^2 v'^2}{\partial y^2}\right)
\end{aligned} \tag{C.4}$$

Rearranging and rewriting some terms then results in:

$$\begin{aligned}-\frac{1}{\rho}\left(\frac{\partial^2 p}{\partial x^2}+\frac{\partial^2 p}{\partial y^2}\right) &= u\left(\frac{\partial}{\partial x}\left(\frac{\partial u}{\partial x}+\frac{\partial v}{\partial y}\right)\right)+v\left(\frac{\partial}{\partial y}\left(\frac{\partial v}{\partial y}+\frac{\partial u}{\partial x}\right)\right)+\left(\frac{\partial u}{\partial x}\right)^2+\left(\frac{\partial v}{\partial y}\right)^2\\ &+2\left(\frac{\partial v}{\partial x}\frac{\partial u}{\partial y}\right)-\nu\left(\frac{\partial^2}{\partial x^2}\left(\frac{\partial u}{\partial x}+\frac{\partial v}{\partial y}\right)+\frac{\partial^2}{\partial y^2}\left(\frac{\partial u}{\partial x}+\frac{\partial v}{\partial y}\right)\right)+\left(\frac{\partial^2 u'^2}{\partial x^2}+2\left(\frac{\partial^2 u'v'}{\partial x\partial y}\right)+\frac{\partial^2 v'^2}{\partial y^2}\right)\end{aligned} \tag{C.5}$$

In this equation it can already be seen that the first two terms on the right hand side, as well as the viscous term, drop out, due to the conservation of mass (see equation C.1). Furthermore, when we square both sides of equation C.1 we find:

$$\left(\frac{\partial u}{\partial x}+\frac{\partial v}{\partial y}\right)^2=\left(\frac{\partial u}{\partial x}\right)^2+\left(\frac{\partial v}{\partial y}\right)^2+2\left(\frac{\partial u}{\partial x}\frac{\partial v}{\partial y}\right)=0 \tag{C.6}$$

Using equation C.6, we can substitute the third and fourth term in equation C.5, which leaves us with the following form of the Poisson equation for the mean pressure:

$$\Delta p = 2\rho\left(\frac{\partial u}{\partial x}\frac{\partial v}{\partial y}-\frac{\partial v}{\partial x}\frac{\partial u}{\partial y}\right)-\rho\left(\frac{\partial^2 u'^2}{\partial x^2}+2\left(\frac{\partial^2 u'v'}{\partial x\partial y}\right)+\frac{\partial^2 v'^2}{\partial y^2}\right) \tag{C.7}$$

In section 4.5 it is explained how this equation is solved in order to obtain the pressure distribution from the PIV velocity field.

Appendix D

Original Data for Slot Suction with Zero Pressure Gradient

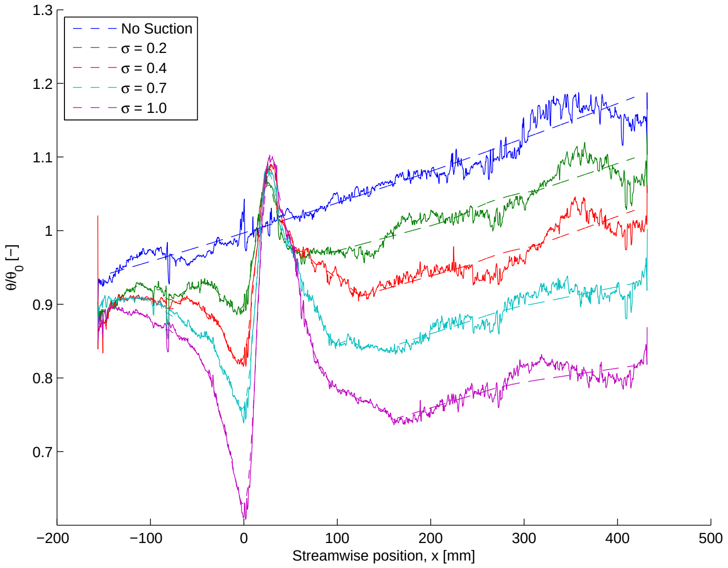

Figure D.1: Momentum thickness for zero pressure gradient case with suction. Trendlines vs. original unsmoothed result.

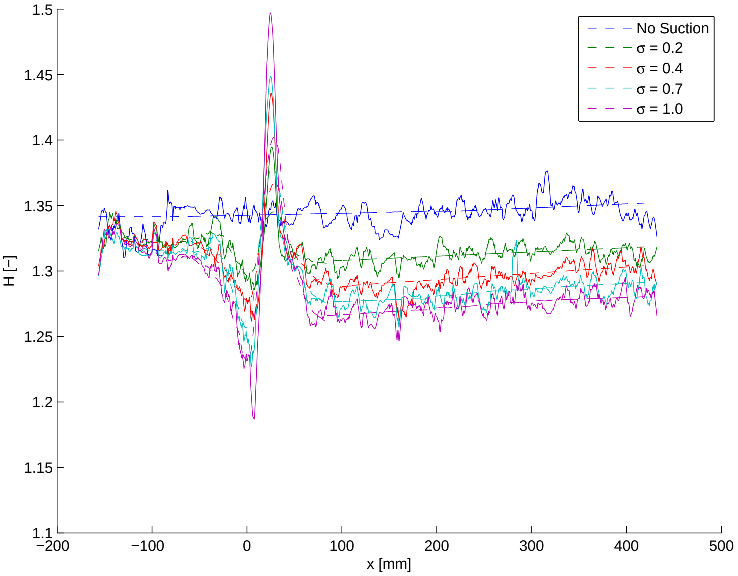

Figure D.2: Shape factor for zero pressure gradient case with suction. Trendlines vs. original smoothed (Sgolay(1,20)) result.

Appendix E

Validation of Volume Flow

This appendix shows the calculations performed to relate the increase in static pressure, due to suction, to the volume of air removed through the slot.

Figure E.1 shows a schematic top view of the experimental setup together with the parameters used during the upcoming calculations.

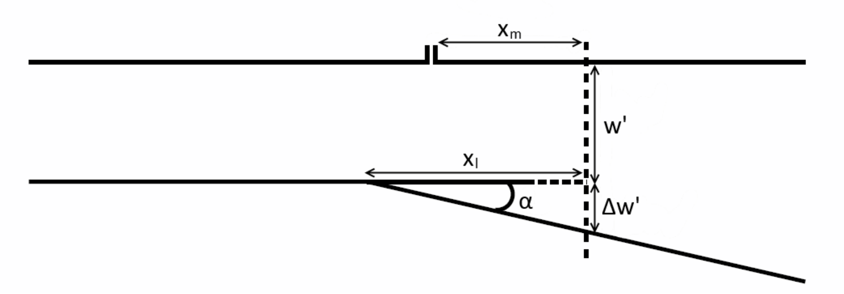

Figure E.1: Schematic topview of experimental setup including calculation parameters.

For the calculations, the position $x_m = 250$ [mm] is considered, which corresponds to the most rearward point in the domain at which the pressure is measured. As already described, the original height, h, and width, w', of the channel are 0.4 [m]. However, the cross-sectional area increases due to the diverging channel, as can be seen from figure E.1. For the zero pressure gradient case, the wall was diverging with an angle of 1 [deg].

The first step now, is to calculate the effective cross-section for the freestream to flow through. That is, the cross-sectional area due to the diverging channel, reduced by the displacement thickness at the four walls. For the measurement wall, this displacement thickness is known, but at the other three walls it is not. For the current calculations, it is estimated to be equal to the displacement thickness at the measurement wall without suction. At one hand, the boundary layer is smaller, since it is not tripped. But on the other hand, it grows slightly more as it is moving over the slightly diverging wall. Locally, where the diverging wall starts, this boundary layer will experience a higher adverse pressure gradient. For the adverse pressure gradient, no good estimate can be made on the thickness, as the effects of the diverging wall (at 14 [deg]) are unknown. Also, the effect of suction on the diverging wall is not known for this case.

Based on the information above, the effective cross-sectional area for the zero pressure gradient case has been calculated according to equation E.1.

$$A_{eff} = w'_{eff} \cdot h_{eff} = (w' + \Delta w' - \delta_1^* - \delta_2^*) \cdot (h - (2 \cdot \delta_2^*)) \tag{E.1}$$

Here, δ_1^* is the measured displacement thickness at the measurement wall and δ_2^* is the estimated displacement thickness at the other walls. The increase in width due to the diverging channel, Δw', is easily calculated using trigonometry (equation E.2).

$$\Delta w' = x_l \cdot tan(\alpha) \tag{E.2}$$

Having the effective cross-section, it is now needed to know the freestream velocity to determine the mass flow. This velocity will be deduced from the pressure data. The total pressure is known from the pitot tube and it is assumed that there is no loss of total pressure in the freestream. Using Bernoulli's law, the dynamic pressure can now be found as the difference between the total and the local static pressure. Furthermore, the density is obtained from the perfect gas law together with measurements of the temperature and the atmospheric pressure.

Combining all this data, the mass flow through the channel can now be found, using to equation E.3.

$$\dot{m}_{channel} = U_{\infty} \cdot A_eff = \sqrt{\frac{p_t - ps}{0.5\rho}} \cdot A_{eff} \tag{E.3}$$

Using the equations above, the mass flow at point x_m is calculated for different cases with and without suction. Subsequently, the observed difference in mass flow is compared with the mass flow measured through the slot. The variables used and the results for the intermediate calculation steps are presented in table E.1. The results are only calculated for the two highest suction coefficients. It should be noted that this calculation procedure is extremely sensitive to a minor variation in the value of certain variables. The reason for this, is that the mass flow being removed, is only in the order of 1 % of the mass flow through the tunnel. Note that the decrease in total pressure for an increasing suction coefficient can be explained by the fact that the wind tunnel power was slightly reduced to have the same dynamic pressure.

	$\sigma = 0$	$\sigma = 0.7$	$\sigma = 1.0$
δ_1 [m]	0.00815	0.00815	0.00815
δ_2 [m]	0.00815	0.00629	0.0054
h [m]	0.4	0.4	0.4
w' [m]	0.4	0.4	0.4
α [deg]	1	1	1
Δw' [m]	0.008	0.008	0.008
p_t [Pa]	464.73	453.89	449.02
p_s [Pa]	-0.14	2.44	3.90
ρ [Kg/m^3]	1.173	1.172	1.172
$Q_{channel}$ [m^3/s]	4.228	4.189	4.168
$Q_{calculated}$ [m^3/s]	-	0.0396	0.0595
$Q_{measured}$ [m^3/s]	-	0.0431	0.0616

Table E.1: Values calculated for adverse pressure gradient case.

From table E.1 it can be seen that there is a fair match between the calculated volume flow and the measured volume flow. For the two suction coefficients considered, there is found to be a maximum deviation of 8 %. Taking into account the sensitivity of the outcomes to minor changes in the input, this is very acceptable. After all, the procedure above was performed to validate, if the rise in pressure could be linked to the removal of the fluid. In order to do so, it is not needed to have a perfectly accurate match between the two.